# Dynamics of Coulomb Correlations in Semiconductors in High Magnetic Fields

by

Neil Alan Fromer

B.S. (Brown University) 1996
M.A. (University of California, Berkeley) 1999

A dissertation submitted in partial satisfaction of the
requirements for the degree of
Doctor of Philosophy

in

Physics

in the

GRADUATE DIVISION
of the
UNIVERSITY OF CALIFORNIA, BERKELEY

Committee in charge:
Daniel S. Chemla, Chair
Roger Falcone
Eugene E. Haller

Spring 2002

The dissertation of Neil Alan Fromer is approved:

Chair Date

Date

Date

University of California, Berkeley

Spring 2002

# Dynamics of Coulomb Correlations in Semiconductors in High Magnetic Fields

Copyright 2002

by

Neil Alan Fromer

## Abstract

Dynamics of Coulomb Correlations in Semiconductors in High Magnetic Fields

by

Neil Alan Fromer

Doctor of Philosophy in Physics

University of California, Berkeley

Daniel S. Chemla, Chair

Current theories have been successful in explaining many nonlinear optical experiments in undoped semiconductors. However, these theories require a ground state which is assumed to be uncorrelated. Strongly correlated systems of current interest, such as a two dimensional electron gas in a high magnetic field, cannot be explained in this manner because the correlations in the ground state and the low energy collective excitations cause a breakdown of the conventional techniques.

We perform ultrafast time–resolved four–wave mixing on $n$-modulation doped quantum wells, which contain a quasi–two dimensional electron gas, in a large magnetic field, when only a single Landau level is excited and also when two levels are excited together. We find evidence for memory effects and as strong coupling between the Landau levels induced by the electron gas.

We compare our results with simulations based on a new microscopic approach

capable of treating the collective effects and correlations of the doped electrons, and find a good qualitative agreement. By looking at the individual contributions to the model, we determine that the unusual correlation effects seen in the experiments are caused by the scattering of photo–excited electron–hole pairs with the electron gas, leading to new excited states which are not present in undoped semiconductors, and also by exciton–exciton interactions mediated by the long-lived collective excitations of the electron gas, inter–Landau level magnetoplasmons.

Daniel S. Chemla
Dissertation Committee Chair

To my family

# Contents

**List of Figures** **v**

**List of Tables** **vii**

**1 Introduction** **1**
1.1 Overview and previous work . . . . . 1
1.2 Outline of this thesis . . . . . 6

**2 Background** **8**
2.1 Introduction . . . . . 8
2.2 GaAs structures . . . . . 8
2.2.1 GaAs quantum wells . . . . . 10
2.2.2 Quantum wells in a magnetic field . . . . . 11
2.2.3 Valence band states . . . . . 14
2.3 Four–wave mixing . . . . . 16
2.3.1 Four–wave mixing measurements . . . . . 16
2.3.2 Maxwell–Liouville equations . . . . . 18
2.3.3 Dephasing and non–Markovian relaxation . . . . . 19
2.4 Multilevel atomic systems . . . . . 20
2.4.1 Two–level system . . . . . 20
2.4.2 Three–level system . . . . . 22
2.5 Coulomb correlations in semiconductors . . . . . 25
2.5.1 The semiconductor Bloch equations . . . . . 26
2.5.2 The Dynamics controlled truncation scheme . . . . . 29
2.5.3 Limits of the DCTS . . . . . 32
2.6 The two dimensional electron gas . . . . . 33
2.7 Conclusion . . . . . 38

**3 Experimental Setup** **39**
3.1 Introduction . . . . . 39
3.2 Samples . . . . . 40
3.3 The laser system . . . . . 42

3.4 The experimental layout . . . 45
3.5 The magnet . . . 47
3.6 Four–wave mixing measurements . . . 49
3.7 Data collection software . . . 51
3.8 Sample characterization measurements . . . 52
3.9 Spot size measurements . . . 53
3.10 Excitation density calculations . . . 54

**4 Linear Absorption Measurements 56**
4.1 Introduction . . . 56
4.2 Linear absorption in semiconductor structures . . . 56
4.3 Absorption in undoped quantum wells . . . 59
4.4 Absorption in modulation doped quantum wells . . . 61
4.5 Conclusion . . . 67

**5 Intra–Landau level excitations 68**
5.1 Introduction . . . 68
5.2 Time integrated four–wave mixing . . . 70
5.3 Spectrally resolved four–wave mixing . . . 71
5.4 Interpretation . . . 74
5.5 Conclusion . . . 79

**6 Inter–Landau level excitations 80**
6.1 Introduction . . . 80
6.2 SR-FWM: Transfer of signal strength . . . 81
6.3 SR-FWM signal vs. time delay . . . 84
6.3.1 Enhanced negative time delay signal . . . 84
6.3.2 Beats in the FWM signal . . . 86
6.4 Summary . . . 86
6.5 Properties of the MDQW signal . . . 89
6.5.1 Magnetic field dependence . . . 89
6.5.2 Intensity dependence . . . 90
6.5.3 pulse duration dependence . . . 95
6.6 Conclusion . . . 97

**7 Theory of FWM in doped Semiconductors 99**
7.1 Introduction . . . 99
7.2 Setup . . . 100
7.3 Time evolution of the photo–excited system . . . 105
7.4 Nonlinear polarization and average polarization model . . . 110
7.5 Simulations . . . 119
7.6 Conclusion . . . 127

**8 Conclusion** **128**
8.1 Summary . . . . . 128
8.2 Future work . . . . . 130

**Bibliography** **132**

**A Derivation of the theory** **148**
A.1 Introduction . . . . . 148
A.2 Problem setup . . . . . 149
A.3 Time dependent interaction effects . . . . . 152
A.4 Nonlinear Polarization equation of motion . . . . . 158
A.5 Dephasing and correlation processes . . . . . 164

**B Symmetry arguments** **170**

**C Derivation of the generalized average polarization model** **174**
C.1 Some useful relations . . . . . 175
C.2 Exciton-exciton interactions in the APM . . . . . 178
C.3 Additional approximations for the APM . . . . . 180

# List of Figures


2.1 FWM emission. . . . . 17
2.2 SR-FWM signal from an ensemble of three–level atoms. . . . . 24
2.3 TI-FWM calculated from the average polarization model. . . . . 31
2.4 TI-FWM in bulk GaAs, theory and experiment. . . . . 32
2.5 Magnetorotons. . . . . 35
2.6 Magnetoplasmons with completely full Landau levels. . . . . 36
2.7 Magnetoplasmons with a partially full Landau level. . . . . 37

3.1 Structure of MBE grown samples . . . . . 41
3.2 Typical laser spectrum and autocorrelation . . . . . 43
3.3 FROG measurement of the laser . . . . . 44
3.4 Layout of the optical table. . . . . 45
3.5 Magnet cross–section . . . . . 48

4.1 Selection rules for optical transitions across the bandgap. . . . . 57
4.2 Selection rules in a magnetic field. . . . . 58
4.3 Absorption spectra of sample D in a magnetic field. . . . . 60
4.4 Peak energy and linewidth vs. magnetic field for sample D. . . . . 61
4.5 Filling factor dependence on magnetic field. . . . . 62
4.6 Absorption spectra of samples A and D at zero magnetic field. . . . . 63
4.7 Absorption spectra of sample A in a magnetic field. . . . . 64
4.8 LL0 absorption peak height and area in a magnetic field. . . . . 65
4.9 Peak energy and linewidth vs. magnetic field for sample A. . . . . 65
4.10 Absorption spectra for sample A at $B = 10$T, both $\sigma^+$ and $\sigma^-$ polarized. . 66

5.1 Absorption spectra and laser excitation of sample A. . . . . 69
5.2 TI-FWM signal measured in sample A for $B = 5.5$ T$\rightarrow 11.5$ T. . . . . 70
5.3 TI-FWM decay times versus magnetic field for samples A and B. . . . . 72
5.4 SR-FWM signal in sample A. . . . . 73
5.5 $N_s^{-1}$ versus magnetic field for samples A and B. . . . . 75

6.1 SR-FWM at $B = 8$T from samples C and D, both LL0 and LL1 directly excited by the laser. . . . . 82

6.2 SR-FWM at $B = 8$T, $\Delta t = 0$ ps from samples C and D, with only LL1 directly excited by the laser. . . . . 84
6.3 FWM vs. time delay $\Delta t$ for sample C at B = 8T, with only LL1 directly excited by the laser. . . . . 85
6.4 FWM vs. time delay for samples C and D at B = 8T, from the LL maxima, both LL0 and LL1 directly excited by the laser. . . . . 87
6.5 FWM emission from LL0 vs. time delay for sample C as a function of magnetic field, both LL0 and LL1 directly excited by the laser. . . . . 90
6.6 FWM emission from LL0 vs. time delay for sample C as a function of magnetic field, with only LL1 directly excited by the laser. . . . . 91
6.7 FWM emission from LL0 vs. time delay for sample C as a function of excitation density, with only LL1 directly excited by the laser. . . . . 92
6.8 FWM emission from LL0 vs. time delay for sample C as a function of excitation density, both LL0 and LL1 directly excited by the laser. . . . . 93
6.9 Relative FWM emission $R$ vs. excitation density for samples C and D, with only LL1 directly excited by the laser. . . . . 94
6.10 FWM vs. time delay for samples C and D at low and high excitation density, with only LL1 directly excited by the laser. . . . . 95
6.11 FWM emission from LL0 vs. time delay for sample C as a function of laser pulse width, with only LL1 directly excited by the laser. . . . . 96

7.1 FWM processes involving 0–$h$, 1–$h$, and 2–$h$ states. . . . . 103
7.2 The states $|X_1\rangle$ and $|Y_1\rangle$. . . . . 107
7.3 The creation of a magnetoplasmon excitation. . . . . 110
7.4 Magnetoplasmon correlation contribution to the FWM signal. . . . . 117
7.5 Simulation of the linear absorption spectrum. . . . . 120
7.6 Simulation of the FWM signal for excitation of both LLs equally. . . . . 121
7.7 Simulation of the FWM signal at $\Delta t = 0$ for the preferential excitation of LL1. 122
7.8 Simulation of the FWM signal vs. $\Delta t$ for the preferential excitation of LL1. 123
7.9 FWM vs. $\Delta t$ calculated from the model, showing the source terms. . . . . 125
7.10 FWM vs. $\Delta t$ calculated from the model, with and without $W$. . . . . 126

# List of Tables

4.1 Sample properties. . . . . 59

## Acknowledgments

I need to start by thanking my thesis advisor, Daniel Chemla, not only for teaching me everything I could learn about semiconductors and science, but also for supporting me with either encouraging words or jokes (whichever was more appropriate). Much of the data in this thesis was taken with Christian Schüller, who brought the knowledge and expertise about the modulation doped samples, and Chih–Wei Lai, who is now helping the magnet lab recover from my time there. I learned the ropes in the lab under the tutelage of Peter Kner, who managed, somehow, to teach me how to do a four–wave mixing experiment. I am also indebted to Ilias Perakis who worked tirelessly from the Mediterranean to help understand our results.

Through the years, I have shared my lab space with a fun yet hard–working crew. Shimshon Barad, Jerome Tignon, Tom Hasche and Steve Dodge were there to help me with my first solo measurements, and later Christian and I got to share table time with, and get advice from, Sarah Bolton and Uli Neukirch.

The ready distractions of Chih–Wei, Marc Carnahan, Jen Glass, Andreas Schumacher, Jon Corson, and Gino Segrè helped to keep me from going insane during the long days of data–taking. Several incarnations of ultimate teams, winter league, and pickup have provided much needed play–time and recreation, and what good is work without play? I am also lucky to have many close friends from Brown in the area (you know who you are). Finally, thanks to my family for all of their support over the years. I wouldn't be anywhere without them.

# Chapter 1

# Introduction

## 1.1 Overview and previous work

Effects of Coulomb correlation manifest themselves in almost all transport and optical properties of semiconductors [39]. They dominate in particular the physics of electron–hole pairs photo–excited near the fundamental optical band gap [22]. However, correlations in the ground state are often not considered, although that state is strongly correlated [62]. This is because the corresponding excitations are high energy and can adjust almost instantaneously to the dynamics of the low energy, near–bandgap carriers. Thus photo–excited electron–hole pairs behave as particles with mutual interactions, without affecting the ground state which, except for providing the band structure and dielectric screening, can be considered as rigid [109]. Then the only Coulomb correlations that need to be considered are dynamically generated by the optical excitation. Such correlation effects in photo–excited undoped semiconductors have been extensively investigated over the past decade (for a review, see Ref. [22]). However, the dynamics of systems with low energy ex-

citations able to interact with photo–excited electron–hole pairs remains almost completely unexplored. Several interesting systems fall into this category, for example high temperature superconductors and fractional quantum Hall effect systems. This is also the case in modulation doped quantum wells, where a two dimensional electron gas exists in the sample and can react to photons and photo–excited carriers. Clearly the dynamics of this system raises very fundamental issues, and this is the motivation for the work presented here.

In the past twenty–five years, the technological applications of the optical properties of semiconductor systems have become increasingly important in their own right. The physics of excitons in quantum wells allows for the fabrication of many important devices, such as semiconductor diode lasers and related optoelectronic gadgets, with myriad applications in communications and consumer products [24]. These devices rely on the Coulomb interaction between the excited carriers to influence the optical response, and as we send information more quickly and efficiently, it is important to understand the behavior of these systems on shorter time and length scales.

Understanding the properties of semiconductor systems far from equilibrium and the role of many–body and Coulomb correlation effects on the femtosecond and nanometer scale is a particularly challenging problem, since the time intervals of interest are often shorter than the interaction times and oscillation periods of the elementary excitations. Examples of well–established pictures that need be revised in this regime include the classical picture of point–like particles experiencing instantaneous collisions [118, 22], and the Boltzmann and thermal bath pictures of relaxation and dephasing [22, 40]. Even the notion of weakly interacting "quasiparticles", a cornerstone of condensed matter physics, must be

revisited when describing the ultrafast nonlinear optical response [22].

In wave mixing experiments, coherent laser photons with different wavevectors interact with the sample, emitting a signal photon into a background free direction. The interaction process requires overall coherence, so that the behavior of the signal in time is a direct measurement of the phase coherence of the excited system. For this reason, ultrafast wave mixing experiments are ideally suited for exploring quantum coherence and correlation effects in semiconductor nanostructures [22, 21, 105]. The time dependent interactions and correlations among the photo–excited carriers can dominate the four–wave mixing signal [21, 22]. Importantly, the time dependent Hartree–Fock treatment of such interactions predicts an exponential rise and decay of the four–wave mixing signal, which is *asymmetric* as a function of time delay (see Ch. 2.5.1 for a detailed description of this theory). However, strong deviations from this profile have been observed experimentally [22, 21] and are due to the Coulomb correlations beyond the mean–field Hartree–Fock level.

The sensitivity of the ultrafast nonlinear spectra to these Coulomb correlations may be traced microscopically to the coupling between the two–particle density matrix, which describes the optical polarization and carrier populations, and the many–particle correlation functions (higher density matrices) [73, 21, 7]. The Hartree–Fock approximation treats the two–particle interactions by factorizing the many–particle correlation functions [40]. However, during time scales shorter than the characteristic times associated with the interaction processes (e.g. the time between successive quasiparticle collisions, or the oscillation period equal to the inverse quasiparticle excitation frequency), these correlations lead to a wave mixing signal that displays a different temporal profile as compared to

that generated by the Hartree–Fock interactions [22, 21]. Such a correlation–induced time dependence can in fact dominate the signal when the photo–excited carriers interact with long–lived collective excitations, or when only a few quasiparticles are excited under low photo–excitation conditions [7, 88, 22, 21].

To theoretically describe the above non–equilibrium many–body effects in the time and frequency dependence of the FWM signal one must use a controlled truncation scheme of the infinite hierarchy of coupled equations for the different correlation functions. In undoped semiconductors, the ground state has an empty conduction band and a full valence band, and the correlations between the photo–excited and ground state electrons can be neglected. A widely used theoretical approach in this case is the dynamics–controlled truncation scheme, or DCTS [8, 9, 7]. In this theory, the response of the semiconductor is expanded in terms of the number of photo–excited electron–hole pairs, and consistently truncated. This can be accomplished because of the correspondence between the number of electron–hole pairs in the system and the sequence of photon absorption and emission. In this way it is possible to systematically include all correlations which contribute to a specified order in the applied field. However, if carriers are present in the system before the excitation, this correspondence breaks down, and the DCTS fails [9]. This is the case in our modulation doped quantum well system, where a two dimensional electron gas exists in the ground state. A theory based on a canonical transformation and time dependent coherent states has recently been introduced [85, 82, 83, 87, 94, 108, 88], and used to study the case where the interactions with the electron Fermi sea dominate the coherent nonlinear response.

In the absence of long–lived collective excitations, a many–particle system such as a Fermi sea can react to the photo–excited carriers almost adiabatically, i.e. during time scales much shorter than the pulse duration. In this case, the Fermi sea behaves to first approximation as a thermal bath, and its interactions with the photo–excited carriers can be treated within the dephasing and relaxation time approximations. However, this is not the case when the time it takes the many–body system to readjust to the intrusion of the photo–excited carriers is comparable to or longer than the measurement times [94]. Dissipation has not occurred during the time scales of interest, and non–Markovian memory effects dominate the measured nonlinear optical dynamics [22, 40, 118]. Such memory effects come from the interactions between the photo–excited carriers and the elementary excitations of the many–body system (e.g. plasmons, phonons, magnons, etc). To describe such effects one must account for the time evolution of the *coupled* photo–excited carrier/many–body system.

In Fermi sea systems, the direct exciton–exciton interactions, which dominate the nonlinear response in undoped semiconductors, are screened. Thus the nonlinear response is determined by the Fermi sea excitations. For resonant photo–excitation, inelastic electron–electron scattering processes dominate the optical dynamics [50, 117]. For low temperatures, the dephasing times increase by a few picoseconds, in agreement with Fermi liquid theory [46]. For below resonance excitation, the dissipation processes are suppressed and coherent effects dominate. A novel dynamics of the system is then observed, due to many–body correlations of the photo–excited holes with the excitations of the Fermi sea [18, 83].

With strong magnetic fields, the Coulomb interaction effects are strongly enhanced

due to the suppression of the kinetic energy (magnetic confinement) [43, 115]. Importantly, the dispersionless single–particle energy spectrum dramatically suppresses the inelastic electron–electron scattering that otherwise plagues the ultrafast dynamics of Fermi sea systems [11]. The correlations between the two dimensional electron gas excitations and the photo–excited carriers then lead to new dynamical features in the nonlinear optical spectra even for resonant photo–excitation conditions. Such effects are most interesting in the quantum Hall effect regime [95, 113], where long lived collective excitations dominate the spectrum of the electron gas [45, 65, 66]. In this thesis we describe the results of wave mixing experiments which were designed to study the dynamics of the interactions between photo–excited carriers and the collective excitations of the two dimensional electron gas in a strong magnetic field, and we apply the theoretical approach of Refs. [85, 82, 83, 87, 94, 108, 88] to interpret the results.

## 1.2 Outline of this thesis

In the next chapter, we present the theoretical background necessary to understand the experiments, including the energy level structure of GaAs heterostructures both with and without an applied magnetic field, an overview of four–wave mixing theory in atomic systems and undoped semiconductors, and the elementary excitations of the two dimensional electron gas system. In chapter 3, we give the details of the experimental apparatus. Chapter 4 details the linear absorption spectra of both undoped and modulation doped quantum wells, as a function of applied magnetic field. In chapter 5, we describe nonlinear experiments performed on the modulation doped quantum wells, designed to

probe the intra–Landau level excitations of the electron gas. Experiments which probe the inter–Landau level excitations of the electron gas are presented in chapter 6, and a theoretical framework developed to explain these results is presented in chapter 7. Finally, we summarize the results and discuss the future research possibilities in chapter 8.

# Chapter 2

# Background

## 2.1 Introduction

This chapter provides a general background for understanding the main results of this work. We begin by reviewing the band structure of GaAs heterostructures, and discussing the effects of the magnetic field on electrons and holes in 2D systems. We will then describe some of the standard theories of four–wave mixing, first in atomic systems, and then in semiconductor samples, followed by a discussion on the breakdown of these theories in doped semiconductors. We will end the chapter with some information on two dimensional electron gas systems in a magnetic field.

## 2.2 GaAs structures

GaAs and GaAs/AlGaAs structures can be grown with remarkable purity and precise control using molecular beam epitaxy (MBE), leading to sharp resonances and long

lifetimes for transitions. This gives us an excellent venue for studying the ultrafast correlations of the many–body semiconductor system.

The band structure of bulk GaAs near the $\Gamma$–point is well described by the effective mass approximation. There are 2 degenerate $s$–like conduction bands, and 6 $p$–like valence bands. The low temperature bandgap is $E_g = 1.519$ eV. The total angular momentum is a good quantum number, so we can label the bands by $|J, m_J\rangle$. The lowest lying valence bands, $|1/2, \pm 1/2\rangle$, called the split–off bands, are separated from the other valence bands by the spin–orbit coupling. The large splitting between these bands and the other valence bands ($\approx 0.34$ eV at low temperature) allows us to neglect the split–off bands altogether. The $J = 3/2$ bands are called the heavy hole (hh, $m_J = \pm 3/2$) and light hole (lh, $m_J = \pm 1/2$) bands. They are degenerate at $k = 0$, but they have different curvature, and therefore different energies away from the zone center. The conduction bands have $S = 1/2$, $m_S = \pm 1/2$. The effective masses are $m^*_{hh} = 0.5m_0$, $m^*_{lh} = 0.082m_0$, and $m^*_e = 0.0665m_0$, where $m_0$ is the bare electron mass.

An additional bonus for the fabrication of GaAs based structures is that while the bandgap for AlAs is much higher than that of GaAs, the lattice constants for the two compounds are nearly identical. That means that alternating layers of GaAs and AlGaAs can be grown on top of one another with very little strain induced at the interfaces. By sandwiching a layer of GaAs between two layers of AlGaAs, we can create a quantum well (QW), or a finite potential well, in the growth direction. Electrons and holes excited in the GaAs layer behave like a quasi–two dimensional system. This confinement has a large effect on the system.

### 2.2.1 GaAs quantum wells

The electronic states of the QW are modified from that of bulk GaAs by the confinement potential. Inside the 2D plane, the confinement potential lifts the hh–lh degeneracy at $k = 0$, so that the hh–conduction band transition is at a lower energy than the lh transition. Also, the motion in the growth direction is quantized by the box potential into a series of subbands. Below each are a series of sharp features corresponding to the excitonic bound states. The Coulomb interaction between electrons and holes can be characterized by the 3D Rydberg energy $R = me^4/2\epsilon_0^2$ and the Bohr radius $a_0 = \epsilon_0/me^2$. The energy levels of the 2D excitonic states are obtained by solving the relative motion Schrödinger equation for a 2D electron–hole pair:

$$\left[\frac{\mathbf{p}^2}{2m} - \frac{e^2}{\epsilon_0 r}\right]\phi_\alpha(r) = E_\alpha \phi_\alpha(r), \tag{2.1}$$

where $r$ is the electron–hole separation, $\mathbf{p}$ is the relative momentum, and $m$ is the reduced mass $1/m = 1/m_e + 1/m_h$. The energy levels $E_\alpha$ are given by

$$E_\alpha = E_g - \frac{R}{(\alpha - 1/2)^2} \tag{2.2}$$

and the wavefunction for the lowest exciton state ($1s$) is

$$\phi_{1s}^{2D}(r) = \left(\frac{2}{\pi}\right)^2 \frac{2}{a_0} e^{-2r/a_0} \tag{2.3}$$

in real space and

$$\phi_{1s}^{2D}(k) = \frac{(2\pi)^1/2(a_0/2)}{[1 + (a_0 k/2)^2]^3/2} \tag{2.4}$$

in $k$–space. The wavefunction of the 2D exciton is more compact than in 3D, and the binding energy is four times higher.

The discussion above is based on the idealization that a QW structure is a perfect 2D system. In fact, this is not the case [14]. The band gap of $Al_xGa_{1-x}As$ is larger than that of GaAs, but not infinitely high. This implies that in the $z$–direction, the electron and hole wavefunctions are not entirely confined within the QW, but rather they penetrate into the barrier regions. Also, the QW itself has a finite thickness in the $z$–direction. We shall continue treating the QW system as purely 2D, which means we ignore these effects. As we shall see in the next section and in the coming chapters, these deviations from the ideal 2D system allow us to observe some interesting results.

### 2.2.2 Quantum wells in a magnetic field

The addition of a magnetic field will dramatically change the electronic properties of the system. If the field is applied along the growth direction (which we will call the $z$ direction), it will effectively confine the motion of the electrons and holes within the 2D QW plane. Classically, a charged particle in a magnetic field will undergo a circular orbit in the $xy$–plane. Quantum mechanically, the motion is described by the relative motion Schrödinger equation for a 2D electron hole pair in a perpendicular field,

$$\left[\frac{1}{2m_e}\left(\mathbf{p}+\frac{e}{2c}\mathbf{B}\times\mathbf{r}\right)^2+\frac{1}{2m_h}\left(\mathbf{p}-\frac{e}{2c}\mathbf{B}\times\mathbf{r}\right)^2-\frac{e^2}{\epsilon_0 r}\right]\phi_\alpha(\mathbf{r})=E_\alpha\phi_\alpha(\mathbf{r}), \tag{2.5}$$

where we have assumed zero center of mass motion, and omitted the bandgap energy and the Zeeman energy.

The electron–hole relative motion is determined by an effective interaction, after expanding Eq. (2.5),

$$V_{\text{eff}}(r)=-\frac{e^2}{\epsilon_0 r}+\frac{e^2B^2r^2}{8mc^2}. \tag{2.6}$$

For $B \neq 0$ all solutions to Eq. (2.5) are bound, since $V_{\text{eff}}(r)$ is an infinite potential in the limit $r \to \infty$.

The magnetic field effects can be characterized by the cyclotron energy $\omega_c = eB/mc$ and the magnetic length $l_c^2 = c/eB$ (we have set $\hbar = 1$). If there were no Coulomb interaction between the electrons and holes, the solutions to Eq. (2.5) would be a series of highly degenerate Landau levels. The energy levels of that system increase linearly with the magnetic field, and are given by $E_\alpha^{Landau} = E_n = \omega_c(n + 1/2)$. The Landau level wavefunctions are

$$\varphi_{nm}(r) = \frac{2^{|m|}}{l_c|m|!(2\pi)^{1/2}} \left(\frac{n!}{(n+|m|)!}\right)^{-1/2} (r/2l_c)^{|m|} e^{-(r/2l_c)^2} L_n^{(|m|)}(r^2/2l_c^2) e^{im\phi}, \qquad (2.7)$$

where $L_m^{(n)}(\xi)$ are generalized Laguerre polynomials. The degeneracy of each level is given by $D = (2\pi l_c^2)^{-1}$. Notice that this wavefunction does not depend on the band parameters, such as the effective mass. We will return to this point at the end of the section.

We can compare the relative importance of the magnetic field potential and the Coulomb potential by looking at the dimensionless parameter $\lambda = (a_0/l_c)^2 = \omega_c/2R$. For $\lambda \ll 1$ the Coulomb term dominates, and for $\lambda \gg 1$ the magnetic field dominates. In GaAs, the cross–over field (for which $\lambda = 1$) is approximately 3.5 Tesla.

When $\lambda \ll 1$, the magnetic field acts as a perturbation to the excitonic states. In this case, the energy levels of the exciton system vary quadratically with the applied field,

$$E_\alpha(B) \approx E_\alpha + \frac{e^2}{8mc^2}\langle r_\alpha^2\rangle B^2. \qquad (2.8)$$

When $\lambda \gg 1$, the Coulomb interaction can be thought of as a perturbation on the Landau

level structure. In this regime,

$$E_\alpha(B) \approx E_\alpha^{Landau} - \sqrt{2\pi}\frac{a_0}{l_c}E_0^{exciton}, \tag{2.9}$$

where $E_\alpha^{Landau}$ increases linearly with $B$ and the Coulomb correction increases like $B^{1/2}$, so that for large $B$, we asymptotically approach the bare energies of the Landau levels. For intermediate values of $\lambda$, Eq. (2.5) must be solved numerically.

When the magnetic field is turned on, the states $\phi_\alpha(r)$ are no longer pure states of the system. We can expand these wavefunctions on the basis of Landau level wavefunctions $\varphi_{nm}(r)$ given in Eq. (2.7), the solutions to the system in the absence of Coulomb interaction. Here, $n$ is the Landau level number, and $m$ is the azimuthal quantum number. For the optically active $s$–like excitons ($m = 0$), the expansion coefficients satisfy [112]

$$\sum_{n'}(E_n\delta_{n,n'} - V_{n,n'})\phi_\alpha(n') = E_\alpha\phi_\alpha(n) \tag{2.10}$$

where $E_n = \lambda(2n-1)$ is the Landau level energy, and for $(n \leq n')$,

$$V_{n,n'} = \left(\frac{2\lambda}{\pi}\right)^{1/2}\frac{\Gamma(n'-n+1/2)\Gamma(n-1/2)}{\Gamma(n'-n+1)\Gamma(n)}\,{}_3F_2\left({}^{1-n,n'-n+1/2,1/2}_{n'-n+1,3/2-n};1\right). \tag{2.11}$$

The function ${}_3F_2$ is a hypergeometric function [67]. All energies and lengths are measured in units of $R$ and $a_0$. This description of magnetoexcitons in terms of two–level transitions at energies $E_n$ coupled by a Coulomb potential $V_{n,n'}$ will prove quite useful in understanding the nonlinear optical response of the samples measured in our work.

In a very high magnetic field, the particles are confined to a single degenerate Landau level, with (2D) wavefunctions given by Eq. (2.7). As mentioned above, these wavefunctions are independent of the band parameters, and therefore at high magnetic field, the electron and hole wavefunctions are identical. This electron–hole symmetry greatly

simplifies the interactions between the particles at high field. For instance, in the case of complete symmetry, there should be no interactions between the photo–excited carriers [57]. Also, there should be no resonant Raman scattering from inter–Landau level excitations of a two dimensional electron gas in the symmetric case [92, 31]. However, several details of real–world samples lead to an asymmetry between electrons and holes even in this case. As mentioned in the previous section, the QW is not a perfect 2D system, and the wavefunctions penetrate into the barriers, leading to asymmetry. The strong coupling of the different valence band spin states in a magnetic field, discussed in the next section, also leads to differences between the electron and hole states at high magnetic field. In Ch. 7 we will discuss the effects of this electron–hole asymmetry on the four–wave mixing results presented in this work.

### 2.2.3 Valence band states

The above description of the QW eigenstates in a magnetic field gives a good qualitative understanding of the system, but it is inadequate for a quantitative understanding. The reason for this lies in the neglect of the spin and orbital angular momentum of the valence and conduction band states. This is important not only to explain the Zeeman splitting of the conduction band states, but also because of the mixing of the nearly degenerate hh and lh valence bands. Also, the confinement at the interfaces of the QW structures changes the band mixing and modifies the linear absorption spectra. Many authors have treated these topics in detail [2, 4, 15, 19, 28, 67, 110, 111, 121, 122]. We will present a framework for such calculations here.

For the $s$–like conduction band states, the interaction between the electron spin

and the magnetic field does not significantly modify the picture. The Zeeman Hamiltonian is $H_{Zeeman} = g^* \mu_B \vec{S} \cdot \vec{B}$ where $g^*$ is the electron $g$–factor in the material. In the conduction band we can separate the wave function $\psi(r, \sigma_z) = \phi(r)\zeta(\sigma_z)$, and the Zeeman splitting can be super–imposed over the Landau level structure.

However, the valence band structure is more complicated. There is a doubly degenerate pair of $p$–like bands at the $\Gamma$–point in the bulk material. Luttinger [64] wrote a Hamiltonian, with the full symmetry of the hh and lh bands and exact to second order in $k$ and first order in the magnetic field, which provides an accurate description of the dispersion of the valence band for energies significantly smaller than the split–off energy ( 0.34 eV). The Luttinger Hamiltonian is

$$\begin{aligned} H &= H_h + H_m && (2.12) \\ H &= -\frac{\gamma_1}{2m_0}k^2 + \frac{\gamma_2}{m_0}\left[\left(J_x^2 - \frac{1}{3}J^2\right)k_x^2 + \left(J_y^2 - \frac{1}{3}J^2\right)k_y^2 + \left(J_z^2 - \frac{1}{3}J^2\right)k_z^2\right] \\ &- 2\frac{\gamma_3}{m_0}\left(\{k_y, k_z\}\{J_y, J_z\} + \{k_z, k_x\}\{J_z, J_x\} + \{k_x, k_y\}\{J_x, J_y\}\right) && (2.13) \\ H_m &= \beta_4(B_x J_x + B_y J_y + B_z J_z) + \beta_5(B_x J_x^3 + B_y J_y^3 + B_z J_z^3) && (2.14) \end{aligned}$$

where $H_h$ is the kinetic term, $H_m$ is the magnetic term, and $\{J_a, J_b\} = 1/2(J_a J_b + J_b J_a)$ are symmetrized products of operators. The parameters $\beta$ and $\gamma$ exactly describe the effective masses and magnetic field dispersion of the valence band. For bulk material in the absence of a magnetic field, the Hamiltonian can be diagonalized to give the exact eigenvalues and eigenvectors of the valence band. For a zinc–blende semiconductor such as GaAs, the energy levels are

$$E = -\frac{1}{m_0}\left[\frac{1}{2}\gamma_1 k^2 \pm \sqrt{\gamma_2^2 k^4 + 3(\gamma_3^2 - \gamma_2^2)(k_y^2 k_z^2 + k_z^2 k_x^2 + k_x^2 k_y^2)}\right]. \qquad (2.15)$$

Often, the simplifying assumption that the band structure is isotropic within the plane, called the axial approximation, is made. This is accomplished by setting $\gamma_2 = \gamma_3$ in the above equations. We can then find solutions at finite magnetic fields. The wavefunctions in the valence band will be a combination of the different hh and lh subbands, with a different Landau level associated with each spin subband [122]. The eigenvectors take on the four–component spinor form $(F_{3/2,n-2}, F_{1/2,n-1}, F_{-1/2,n}, F_{-3/2,n+1})$. The first subscript is the $z$–component of the angular momentum $m_J$, and the second is the harmonic oscillator index which describes the nature of the Landau level associated with that $m_J$ state. The spatial part of $F$ is the 2D harmonic oscillator function in the $xy$–plane. The solution of this system is a tedious numerical calculation, which must be carried out for the specific samples used. The effects of this coupling on the optical properties of semiconductor samples will be discussed in Ch. 4. We do not have detailed calculations for our samples, and therefore in the most of the future discussions we will continue to limit ourselves to the simple two–band model, which will be suitable to qualitatively interpret our results.

## 2.3 Four–wave mixing

### 2.3.1 Four–wave mixing measurements

The experiments discussed in this work are two–pulse degenerate four–wave mixing (FWM) experiments, in which two pulses from a single modelocked laser, with central frequency $\omega$ and wavevectors $\vec{k}_1$ and $\vec{k}_2$ (called pulse 1 and 2, respectively) are focused on the sample separated by a time delay $\Delta t$ . A FWM signal is then emitted in both the $2\vec{k}_2 - \vec{k}_1$ and $2\vec{k}_1 - \vec{k}_2$ directions. If the two pulses are equal in intensity, then both directions

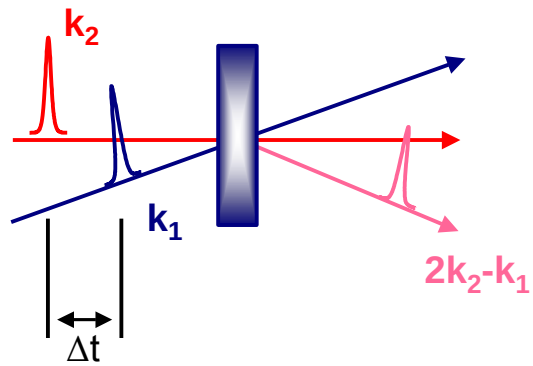


Figure 2.1: FWM emission.

will show the same signal, but with an opposite sign convention for $\Delta t$ . For our work we consider the signal in the $2\vec{k}_2 - \vec{k}_1$ direction, for which $\Delta t$ is considered positive when pulse 1 arrives first. The basic configuration is shown in Fig. 2.1.

There are several measurements that can be made on a FWM signal. The simplest is to measure the total energy of the signal as a function of the time delay $\Delta t$ . This is called time–integrated FWM (TI-FWM). In spectrally–resolved FWM (SR-FWM), we measure the intensity of the FWM signal as a function of both frequency and $\Delta t$ , by sending the signal into a spectrometer. It is also possible to measure the signal intensity in the time domain. In time–resolved FWM (TR-FWM), the temporal resolution is achieved by doing a cross–correlation of the signal with a short reference pulse. The setup for making TI-FWM and SR-FWM measurements will be described in chapter 3. Techniques have also been developed to characterize a weak signal such as FWM in both amplitude and phase [29, 55], but since we have not performed such measurements, they will not be detailed here.

### 2.3.2 Maxwell–Liouville equations

In all measurements, we are detecting the electric field of the light emitted in the direction $2\vec{k}_2 - \vec{k}_1$ . To calculate this field, the coupled equations for light propagation, Maxwell's equations, and for the behavior of the sample, governed by the Hamiltonian, need to be solved together. For most nonlinear optics experiments, including ours, the light field contains a large number of photons, and can therefore be treated classically.

The wave equation for the electric field, derived from Maxwell's equations, describes the propagation of the light through the sample:

$$\nabla \times \nabla \times \vec{E}(r,t) + \frac{1}{c^2}\frac{\partial^2}{\partial t^2}\vec{E}(r,t) = -\frac{4\pi}{c^2}\frac{\partial^2}{\partial t^2}\vec{P}(r,t), \tag{2.16}$$

where $\vec{P}(r,t)$ is the polarization created inside the sample, which must be calculated quantum-mechanically. A common technique is to use the density matrix formalism, in which the expectation values of operators are calculated from the density matrix, $\rho(t)$:

$$\vec{P}(r,t) = Tr[\hat{P}(r,t)\rho(t)] \tag{2.17}$$

$$\frac{\partial}{\partial t}\rho(t) = -\frac{i}{\hbar}\left[H(\vec{E}(r,t)), \rho(t)\right]. \tag{2.18}$$

In general, equations (2.16), (2.17) and (2.18) need to be solved self–consistently for $\vec{E}(r,t)$ and $\vec{P}(r,t)$ throughout the sample. Throughout our work, we have made the assumption that the sample is optically thin, which simplifies these equations by allowing us to ignore the spatial dependence of the polarization and the electric field along the propagation direction of the sample. We can calculate $\vec{P}(t)$ from the input electric field on the sample surface, and then calculate the electric field emitted from $\vec{P}(t)$. The problem is thus reduced to the calculation of equations (2.17) and (2.18) for the polarization.

The following sections will discuss the calculation of the density matrix elements, and the FWM signal, for various systems. We can split the equation of motion for $\rho(t)$ into two parts:

$$i\hbar\frac{\partial}{\partial t}\rho = i\hbar\frac{\partial}{\partial t}\rho_{coh} + i\hbar\frac{\partial}{\partial t}\rho_{scatt}. \tag{2.19}$$

The coherent part of the solution is derived from the Heisenberg equations of motion, and this is what we will concern ourselves with solving in the rest of the section. First we will briefly analyze the scattering term.

### 2.3.3 Dephasing and non–Markovian relaxation

A semiconductor is described by a Schrödinger equation which is local in time, i.e. it depends only on the current state of the system and not the past history. If we could solve it using the full Hamiltonian for the system, our equations of motion would also be local in time. However, a semiconductor is such a complex many–body system that this cannot be achieved. It is common to divide the full problem into a system that is analyzed in detail, and a thermal "reservoir" containing all the other degrees of freedom. For the semiconductor, the system is often the interband electronic transitions and the photons, and the reservoir contains the phonons, and other carriers in the sample. Imagine that at time $t'$ the system excites a degree of freedom of the reservoir, which then evolves according to its own energy. At a later time $t$, the reservoir interacts again with the system. This will introduce into the evolution of the system a memory kernel, or an interaction which depends on the past behavior of the system, making the equations of motion non–local in

time. For the evolution of the polarization in the sample, this can be expressed as

$$i\hbar\frac{\partial}{\partial t}p(t) = \int_{-\infty}^{t} dt'\Gamma(t-t')p(t'), \tag{2.20}$$

where we have introduced the memory kernel $\Gamma(t-t')$ which characterizes how long the system remembers its past. In the relaxation time approximation (also called the Markovian regime), the system is assumed to have an infinitely fast memory, $\Gamma(t-t') = \gamma\delta(t-t')$. The relaxation can be described by a single dephasing time $T_2 = 1/\gamma$. It is also worth noting that a memory kernel in the time domain corresponds to an energy dependent scattering rate (or linewidth) in the frequency domain. By taking the Fourier transform of Eq. 2.20, we find $i\hbar\omega p(\omega) = \Gamma(\omega)p(\omega)$.

A detailed calculation of FWM and dephasing in the non–Markovian regime, when the relaxation time approximation is not valid, requires sophisticated theoretical methods, beyond the scope of this work [53, 52, 38, 96]. A comprehensive review of the current theory of scattering at the earliest stages of relaxation can be found in Ref. [39]. Recently, a theory which connects this regime to the microscopic theory of Coulomb correlations in semiconductors in the coherent regime (discussed later in this chapter) has been presented [98].

## 2.4 Multilevel atomic systems

### 2.4.1 Two–level system

Before attempting to solve for the coherent part of Eq. (2.19) for a complicated many–body system such as a semiconductor, it is helpful to consider a model system. The

ideal system for thinking about FWM is an ensemble of non–interacting two–level systems, which is the idealization of a dilute gas of atoms with a single transition nearly resonant with the laser frequency. The Hamiltonian for this system is

$$H_{tot} = E_0 c_0^\dagger c_0 + E_e c_e^\dagger c_e - \mu E(t) c_e^\dagger c_0 - \mu^* E^*(t) c_0^\dagger c_e, \tag{2.21}$$

where $c_0^\dagger$ creates a particle in the ground state and $c_e^\dagger$ in the excited state. $E(t)$ is the electric field, and $\mu$ is the dipole moment.

The density matrix elements are the expectation values of the two–particle operators, $\rho_{i,j}(t) = \langle c_j^\dagger c_i \rangle$, where $i, j = 0, e$ are the level indices. The Liouville equation (2.18) can be written for each component of $\rho(t)$, within the relaxation time approximation. This results in the optical Bloch equations [3]:

$$i\hbar \frac{\partial}{\partial t}\rho_{ee} = iIm\{\mu^* E^*(t)\rho_{e0}\} - \frac{i\hbar}{T_1}\rho_{ee} \tag{2.22}$$

$$i\hbar \frac{\partial}{\partial t}\rho_{00} = -iIm\{\mu^* E^*(t)\rho_{e0}\} - \frac{i\hbar}{T_1}(\rho_{00} - 1) \tag{2.23}$$

$$i\hbar \frac{\partial}{\partial t}\rho_{e0} = \Delta\rho_{e0} - \mu E(t)(\rho_{00} - \rho_{ee}) - \frac{i\hbar}{T_2}\rho_{e0}. \tag{2.24}$$

Here $\Delta \equiv E_e - E_0$, $T_1$ is the population relaxation time and $T_2 = 1/\gamma$ is the dephasing time. The nonlinearity in the polarization ($\rho_{e0}$) comes from terms $\propto E(t)(\rho_{00} - \rho_{ee})$, related to the fact that the excitations obey the Pauli exclusion principle. This is called the Pauli Blocking (PB) nonlinearity, and it is present in all material systems containing fermions.

We can solve these equations perturbatively in powers of the electric field. We would like to solve for the third order response in the $2\vec{k}_2 - \vec{k}_1$ direction when the applied electric field is $E(t) = \mathcal{E}_1(t)e^{i(\vec{k}_1\cdot\vec{r}-\omega t)} + \mathcal{E}_2(t)e^{i(\vec{k}_2\cdot\vec{r}-\omega t)}$, where $\mathcal{E}_1(t)$ and $\mathcal{E}_2(t)$ describe the shape of the laser pulse envelope and are slowly varying when compared to the optical

period. In the short pulse limit, $\mathcal{E}_1(t) = E_1\delta(t+\Delta t)$ and $\mathcal{E}_2(t) = E_2\delta(t)$, we can solve for the FWM signal analytically. The third order response in the $2\vec{k}_2 - \vec{k}_1$ direction is given by

$$P^{(3)}(t) = \frac{-i|\mu|^4 E_2^2 E_1^*}{\hbar^3}\Theta(\Delta t)e^{i(\frac{\Delta}{\hbar}+i\gamma)\Delta t}\Theta(t)e^{-i(\frac{\Delta}{\hbar}-i\gamma)t} \tag{2.25}$$

The signal is emitted only after both pulses have arrived at the sample, and only if $\Delta t > 0$. The SR-FWM signal, given by $|P^{(3)}(\omega)|^2$ where $P^{(3)}(\omega)$ is the Fourier transform of $P^{(3)}(t)$, is a Lorentzian with a linewidth given by $T_2$. The TI-FWM signal is given by

$$S_{TI}(\Delta t) = \int_{-\infty}^{+\infty} |P^{(3)}(t,\Delta t)|^2 dt = \frac{1}{\hbar^6}|\mu|^8 I_2^2 I_1 \Theta(\Delta t)\frac{1}{2\gamma}e^{-2\gamma\Delta t}. \tag{2.26}$$

The dephasing time can be directly extracted from either the decay time of the TR-FWM or TI-FWM or the linewidth of the SR-FWM, and the same time constant $T_2$ determines the width of the linear absorption spectrum, so for a homogeneously broadened two–level system there is no new information contained in the FWM measurements. In an inhomogeneously broadened system, the linear absorption linewidth is the inhomogeneous linewidth. In this case, the FWM signal is emitted as a photon echo, which appears $\Delta t$ after the second pulse. The homogeneous linewidth can be determined from the TI-FWM signal, which decays in this case with a time constant of $T_2/4$[3].

### 2.4.2 Three–level system

An example which will be a useful comparison to some of our measurements is a three–level system, or an atom with 2 closely spaced transitions. The Hamiltonian for this system is

$$\begin{aligned} H_{tot} &= E_0 c_0^\dagger c_0 + E_A c_A^\dagger c_A + E_B c_B^\dagger c_B \\ &- \mu_A E(t) c_A^\dagger c_0 - \mu_A^* E^*(t) c_0^\dagger c_A - \mu_B E(t) c_B^\dagger c_0 - \mu_B^* E^*(t) c_0^\dagger c_B. \end{aligned} \tag{2.27}$$

When the laser pulse is tuned directly in resonance with one transition, with only a small excitation of the other, we should recover the two–level system results. However, since the two transitions share a common ground state, they are coupled together, and if we excite both levels with our laser pulse, then the system can either be excited into state $|A\rangle$ or $|B\rangle$, but not both. This coupling will be reflected as beats in the FWM signal, with a period related to the energy difference between the two levels.

We can again write equations for the elements of the density matrix (which is now a 3x3 matrix). For example, the equation for $\rho_{a0}(t)$ is now given by ($\hbar = 1$)

$$i\frac{\partial}{\partial t}\rho_{a0}(t) = (\Omega_A - i\gamma_A)\rho_{a0}(t) - \mu_A E(t)(\rho_{00}(t) - \rho_{aa}(t)) + \mu_B E(t)\rho_{ab}(t). \tag{2.28}$$

A similar equation must be written for $\rho_{b0}(t)$ as well. The transition energies are $\Omega_j = E_j - E_0$, $j = A, B$. These equations can again be solved analytically in the case of delta function excitation. The resulting third order polarization is given by

$$\begin{aligned} P^{(3)}(t) &= -2iE_2^2E_1^*\Theta(t)\left[|\mu_A|^2e^{-i(\Omega_A - i\gamma_A)t} + |\mu_B|^2e^{-i(\Omega_B - i\gamma_B)t}\right] \\ &\times \Theta(\Delta t)\left[|\mu_A|^2e^{i(\Omega_A + i\gamma_A)\Delta t} + |\mu_B|^2e^{i(\Omega_B + i\gamma_B)\Delta t}\right]. \end{aligned} \tag{2.29}$$

In this example it is also enlightening to solve the system numerically for Gaussian pulses, to demonstrate the effect of the laser wavelength on the signal. Figure 2.2 shows the results of these calculations in the frequency domain, when the laser is tuned to excite both transitions equally, and when it only excites only the upper transition, to $|B\rangle$. In the former case, the signal is emitted at the energy of both transitions, and there are large beats as a function of time delay, with a period $\tau = 2\pi/(\Omega_B - \Omega_A)$. The latter case shows the results for the two–level atom, a single exponential decay from $|B\rangle$ with no beats and

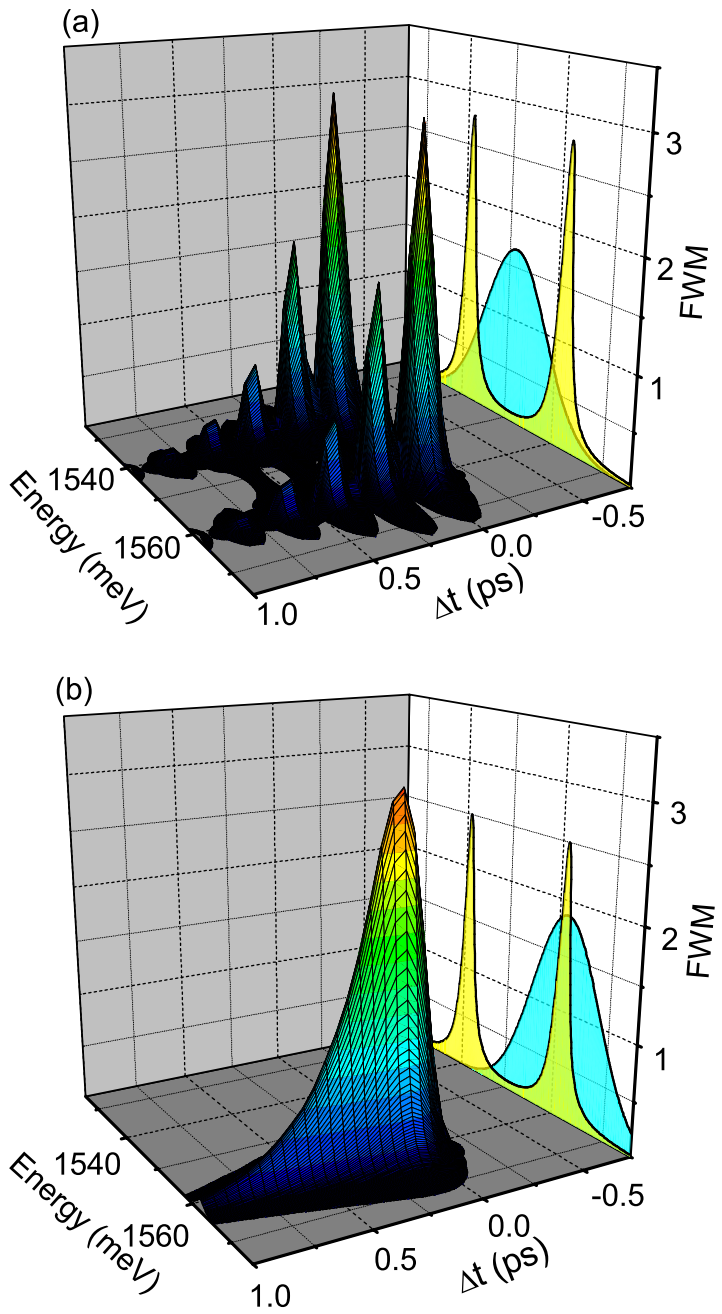


Figure 2.2: Calculated SR-FWM signal from an ensemble of three–level atoms. The exciting laser pulse spectrum and linear absorption are shown as projections on the back screen. The laser pulses are Gaussian with a FWHM of 120 fs, the spacing between transitions is 20 meV, and the dephasing time for both transitions is $T_2 = 0.5$ ps. (a) The signal when both levels are excited equally. (b) The signal when only the level $|B\rangle$ is excited.

no signal from the other transition. We emphasize this result, that without a signal from several transitions, there should be no beats in $\Delta t$ .

## 2.5 Coulomb correlations in semiconductors

Of course, semiconductors aren't non–interacting atomic ensembles, but rather a highly complex many–body system. If we neglect the Coulomb interactions between electrons and holes, we can treat each state in $k$–space as a separate two level system. Or, in a magnetic field, we can assume a each Landau level is a different state, and if we excite only the lowest and next highest levels, this can be treated as a three–level system.

Optical experiments in semiconductors have been explained using multi–level system models (see, eg., [72] and [104]). However, the Coulomb interaction has drastic effects even on the linear optical properties of the semiconductor. Ignoring these interactions, or including them in an *ad hoc* manner, is a poor way to explain the nonlinear results.

To account for the interactions between photo–excited electrons and holes, we need to start from the Hamiltonian for the electron–hole subsystem of the semiconductor [40]:

$$\begin{aligned} H_{tot} &= \sum_{\mathbf{k}} \left[ \epsilon_{c\mathbf{k}} \hat{e}^{\dagger}_{\mathbf{k}} \hat{e}_{\mathbf{k}} + \epsilon_{v\mathbf{k}} \hat{h}^{\dagger}_{\mathbf{k}} \hat{h}_{\mathbf{k}} \right] \\ &+ \frac{1}{2} \sum_{\mathbf{k} \neq \mathbf{k}'} V_{\mathbf{q}} \left[ \hat{e}^{\dagger}_{\mathbf{k}+\mathbf{q}} \hat{e}^{\dagger}_{\mathbf{k}'-\mathbf{q}} \hat{e}_{\mathbf{k}'} \hat{e}_{\mathbf{k}} + \hat{h}^{\dagger}_{\mathbf{k}+\mathbf{q}} \hat{h}^{\dagger}_{\mathbf{k}'-\mathbf{q}} \hat{h}_{\mathbf{k}'} \hat{h}_{\mathbf{k}} - 2 \hat{e}^{\dagger}_{\mathbf{k}+\mathbf{q}} \hat{h}^{\dagger}_{\mathbf{k}'-\mathbf{q}} \hat{h}_{\mathbf{k}'} \hat{e}_{\mathbf{k}} \right] \\ &- \sum_{\mathbf{k}} \left[ \mu_{cv} E(t) \hat{e}^{\dagger}_{\mathbf{k}} \hat{h}^{\dagger}_{-\mathbf{k}} + \mu^{*}_{cv} E^{*}(t) \hat{h}_{-\mathbf{k}} \hat{e}_{\mathbf{k}} \right] . \end{aligned} \tag{2.30}$$

The first line of this equation gives the single particle energies of the electrons and holes. $\hat{e}^{\dagger}_{\mathbf{k}}$ creates an electron with wavevector $\mathbf{k}$, and $\hat{h}^{\dagger}_{\mathbf{k}}$ creates a hole. $\epsilon_{c\mathbf{k}}$ and $\epsilon_{v\mathbf{k}}$ give the dispersion of the conduction and valence bands respectively. The second line of equation (2.30)

describes the Coulomb interaction between electrons (first term), between holes (second term), and between electrons and holes (third term). $V_{\mathbf{q}}$ is the unscreened Coulomb potential in $\mathbf{k}$–space. The last line describes the interaction between the semiconductor and the applied electric field. The dipole moment $\vec{\mu}_{cv}$ can be taken to be independent of the wavevector $\mathbf{k}$. We consider the band dispersions to be parabolic, and given by the effective mass approximation ($\hbar = 1$):

$$\epsilon_{c\mathbf{k}} = E_{c,0} + \frac{k^2}{2m_e^*} \qquad \text{and} \qquad \epsilon_{v\mathbf{k}} = E_{v,0} + \frac{k^2}{2m_h^*}. \tag{2.31}$$

The bandgap ($E_{c,0} - E_{v,0}$) contains the Coulomb interaction of the full valence band.

The polarization is given by

$$\vec{P} = \sum_{\mathbf{k}} \mu^* \langle \hat{P}_{\mathbf{k}} \rangle = \sum_{\mathbf{k}} \mu^* \langle \hat{h}_{-\mathbf{k}} \hat{e}_{\mathbf{k}} \rangle. \tag{2.32}$$

If we write the Heisenberg equation of motion for the operator $\hat{P}_{\mathbf{k}}$, we find that in addition to being driven by other two–particle correlations (polarizations and electron or hole populations), the Coulomb interaction couples the two–particle correlations to four–particle correlations (products of four operators). To solve our equation, we must solve equations of motion for these four–particle correlations. These are in turn driven by six–particle correlations, and so on in an infinite hierarchy. In order to solve the system, we must make some approximations which truncate this hierarchy and give a closed set of equations.

### 2.5.1 The semiconductor Bloch equations

The most common method for dealing with this problem has been to factorize the four–particle correlations into products of two–particle correlations, and then make the

random phase approximation (RPA), which neglects the terms which oscillate rapidly due to large momentum differences. The RPA is also called the time dependent Hartree–Fock (HF) approximation. This leads to a closed set of equations for the two–particle density matrix elements ($n_{e,\mathbf{k}}$, $n_{h,\mathbf{k}}$, and $P_{\mathbf{k}}$), which can be rewritten in a form similar to Eqs. (2.22)-(2.24). These are the well known semiconductor Bloch equations (SBE)[99, 60], given here within the relaxation time approximation:

$$\begin{aligned} i\frac{\partial}{\partial t}P_{\mathbf{k}} &= (\epsilon_{c,\mathbf{k}} + \epsilon_{h,\mathbf{k}} - i\gamma)P_{\mathbf{k}} - \sum_{\mathbf{q}\neq\mathbf{k}} V_{\mathbf{k}-\mathbf{q}}P_{\mathbf{q}} - \mu_{cv}E(t)\left[1 - n_{e,\mathbf{k}} - n_{h,\mathbf{k}}\right] \\ &+ \sum_{\mathbf{q}\neq\mathbf{k}} V_{\mathbf{k}-\mathbf{q}}\left[P_{\mathbf{q}}(n_{e,\mathbf{k}} + n_{h,\mathbf{k}}) - P_{bk}(n_{e,\mathbf{q}} + n_{h,\mathbf{q}})\right] \qquad (2.33) \\ \frac{\partial}{\partial t}n_{j,\mathbf{k}} &= -2Im\left\{P^*_{\mathbf{k}}\left[\mu_{cv}E(t) + \sum_{\mathbf{q}\neq\mathbf{k}} V_{\mathbf{k}-\mathbf{q}}P_{\mathbf{q}}\right]\right\} - \frac{1}{T_1}(n_{j,\mathbf{k}}) \quad (j = e, h). \qquad (2.34) \end{aligned}$$

The SBE are a two–particle mean–field theory. The equations account for the exciton structure, but do not treat exciton–exciton interactions. We will call this RPA level Coulomb nonlinearity the bare Coulomb interaction (BCI). The density matrix elements in Eqs. (2.33) and (2.34) are driven by both the electric field of the laser and a term due to the polarization from all other $k$–states. Mean–field theories, such as the BCS theory of superconductivity [103], have been used to explain many aspects of condensed matter physics. The SBE have been quite successful in explaining many experiments in semiconductors, such as the AC stark effect [99, 100], TR-FWM effects [120], and photon echoes from continuum states [35, 59].

One very important effect of the Coulomb interaction is the existence of a FWM signal for $\Delta t < 0$, seen in experiments on GaAs quantum wells [54, 119]. The prediction of rise time of $T_2/4$ is a general result of the SBE, independent of the excitation or the

material, assuming the system is homogeneously broadened. For an inhomogeneous system there is a weaker signal for $\Delta t < 0$ [44].

It is possible to transform the SBE from $k$–space into the exciton basis (following Ref. [21]). We find there is a non–local Coulomb coupling between the excitons at the BCI level. A useful model can be extracted by averaging over the lowest lying exciton states, and generating an equation of motion for a single average polarization, $\mathcal{P}$. The average polarization model (APM) was first introduced to clarify the RPA theory for FWM, since it captured the essential physics while simplifying the equations to keep the interpretation transparent [119]. In addition to the averaging, we will make the assumption that we are in the coherent regime, and that the length of the Bloch vector is constant, or $n \approx |\mathcal{P}|^2$. We then have only a single equation to solve perturbatively:

$$i\frac{\partial}{\partial t}\mathcal{P}(t) = (\Omega - i\gamma)\mathcal{P}(t) - \mu E(t)\left[1 - \frac{|\mathcal{P}(t)|^2}{\mathcal{P}_s^2}\right] + \mathcal{V}\mathcal{P}(t)|\mathcal{P}(t)|^2. \tag{2.35}$$

Here, $\mathcal{P}_s$ is a saturation parameter and $\mathcal{V}$ is an effective Coulomb coupling parameter. It is straightforward to generalize Eq. (2.35) to include several levels [21], for example the different hole states. The APM has been useful in explaining a number of experiments at the RPA level [119, 120, 102]. However, for a quantitatively accurate simulation of experiments, it is necessary to use the full numerical solutions of the SBE, including all band structure and selection rules.

We can also apply the RPA factorization technique when we have a magnetic field applied to the sample. We start by expanding the magnetoexciton states in terms of the Landau levels, as in Section 2.2.2, and generate a set of equations for $P_n$ and $n_n$, the

polarization and excited population of Landau level $n$ respectively [112]:

$$i\frac{\partial}{\partial t}P_n = \left(E_n - 2\sum_{n'} V_{n,n'} n_{n'}\right) P_n - (1-2n_n)\left(\mu_{cv}E(t) + \sum_{n'} V_{n,n'} P_{n'}\right) \quad (2.36)$$

$$\frac{\partial}{\partial t}n_n = 2Im\left\{P_n\left(\mu_{cv}^* E^*(t) + \sum_{n'} V_{n,n'} P_{n'}^*\right)\right\}. \quad (2.37)$$

The Coulomb interaction $V_{n,n'}$ couples different Landau levels together, and is given in Eq. (2.11). Eqs. (2.36) and (2.37) have been solved numerically for up to 1000 Landau levels [112, 102]. An APM can be generated from this system as well, by keeping only the few Landau levels which are directly excited. However, due to the long range nature of the Coulomb interaction, it is necessary to include many levels in order to achieve any level of accuracy in these calculations.

### 2.5.2 The Dynamics controlled truncation scheme

Over the past several years, numerous experimental effects have been measured which require a theoretical description beyond the RPA, such as the contribution of biexcitons to the nonlinear optical response [10, 63, 48]. The correct interpretation of these experiments requires a formalism in which the Coulomb interaction is accounted for consistently, and to arbitrary order. One such formalism which naturally extends the SBE is the dynamics controlled truncation scheme (DCTS) [8].

Calculating the optical response starts, as before, with the many–body Hamiltonian, Eq. (2.30), and the equation of motion for the polarization. However, unlike in the RPA treatment, the four–particle correlations are not factorized. The results of the DCTS theory are several mathematical theorems which show that certain higher correlations contribute to higher order in the electric field, and can thus be neglected for a calculation of

the optical response to a given order [8, 5, 116]. This can be accomplished because of the correspondence between the number of electron–hole pairs in the system and the sequence of photon absorption and emission. The theory systematically includes all correlations which contribute to a specified order. In the limit of third order processes ($\chi^{(3)}$–truncation), and within the coherent limit, there is only one four–particle correlation function which must be taken into account, the biexciton creation operator $B$ [116, 97]. The effects of additional four–particle correlations, such as the exciton density, and correlations which contribute to fifth order in the electric field, have been investigated as well [13, 17].

The necessary four–particle correlation, $B^{ehe'h'} = \langle \hat{e}\hat{h}\hat{e}'\hat{h}'\rangle - \langle \hat{e}\hat{h}\rangle\langle \hat{e}'\hat{h}'\rangle + \langle \hat{e}\hat{h}'\rangle\langle \hat{e}'\hat{h}\rangle$, gives the biexcitonic structure, both the bound and unbound states. By subtracting the factorized components, we let B characterize the deviation from the RPA theory [97]. The DCTS equations will then contain several driving terms: (1) the PB nonlinearity present even in atomic systems, (2) the BCI Coulomb interaction of the RPA theory, and (3) a new source term which describes the coupling between excitons and the full spectrum of two–exciton states. This final driving term is beyond the RPA, and has a dramatic effect on the FWM signal.

To understand the effect of this correlation, we can update the APM to include higher order correlations, based on the DCTS microscopic theory [97, 49]. For the case of co–circularly polarized laser pulses (which cannot excite a bound biexciton), the new APM equation of motion for the polarization is [49]

$$\begin{aligned} i\frac{\partial}{\partial t}\mathcal{P}(t) &= (\Omega - i\gamma)\mathcal{P}(t) - \mu E(t)\left[1 - \frac{|\mathcal{P}(t)|^2}{\mathcal{P}_s^2}\right] \\ &+ \mathcal{V}\mathcal{P}(t)|\mathcal{P}(t)|^2 + \mathcal{V}_B\mathcal{B}(t)\mathcal{P}(t)^* \end{aligned} \tag{2.38}$$

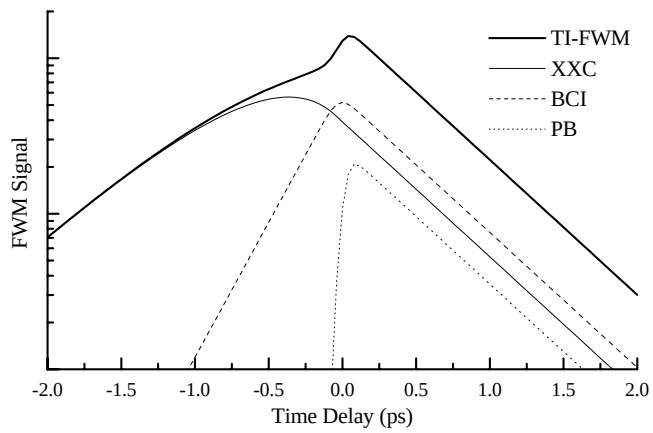


Figure 2.3: TI-FWM calculated from the average polarization model, showing the different time dependence of the Pauli blocking (PB), mean–field (BCI), and exciton–exciton correlations (XXC). From Kner *et al.* [48].

where the function $\mathcal{B}$ is an effective four–particle correlation function describing the continuum of unbound biexciton states, and satisfying the equation

$$i\frac{\partial}{\partial t}\mathcal{B}(t) = (2\Omega - i\Gamma)\mathcal{B}(t) + \mathcal{P}(t)^2. \tag{2.39}$$

Unlike the PB nonlinearity which exists only for $\Delta t > 0$, or even the BCI nonlinearity for which the rise time is half the decay time, new source term due to exciton–exciton correlations (XXC) grows in a non–exponential fashion, and for $\Delta t < 0$ can dominate the signal, as shown in Fig. 2.3. These equations can easily be generalized to include the four Zeeman split hh and lh transitions in a magnetic field [30]. The updated APM has also been used to explain the effects of the bound biexciton on the pump/probe spectrum of ZnSe QWs and microcavities [74, 75]. The functional form of the model is directly related to the full microscopic theory, which makes it qualitatively different from a simple multi–level scheme.

Several different formalisms have been developed which are able to account for

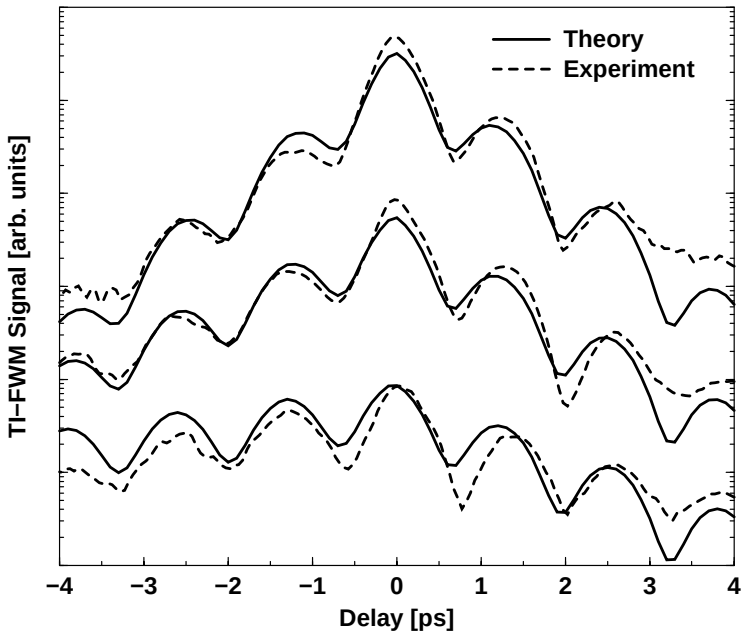


Figure 2.4: Theoretical and experimental TI-FWM signals from bulk GaAs at 10T, for colinear polarized excitation and densities $n = 1.5 \times 10^{15}\text{cm}^{-}3$,$1.5 \times 10^{16}\text{cm}^{-}3$, and $5 \times 10^{16}\text{cm}^{-}3(\times 10)$ (bottom to top). From Schäfer *et al.* [98].

higher order correlations, and many are in fact equivalent to the DCTS [87, 73, 68, 79]. Recently, a theory has been presented which bridges the gap between the DCTS and theories based on Greens functions which explain the build–up of screening effects [98]. Within this theory it is possible to simulate with remarkable accuracy the results of FWM in bulk GaAs in a high magnetic field, as seen in Fig. 2.4.

### 2.5.3 Limits of the DCTS

The DCTS is successful because in many semiconductor systems, there is a correspondence between the number of electron–hole pairs in the system and the absorption of photons. In semiconductor systems where this scheme is applicable, we have been able to

explain the experimental results with incredible accuracy. However, if this correspondence breaks down, the DCTS fails. This is the case, for instance, in modulation doped quantum wells (MDQWs), where a high mobility two dimensional electron gas (2DEG) exists in the sample before excitation, and can react to photons and photo–excited carriers. In the coming chapters, we will investigate some of the unusual results of FWM in these materials, and present a new theoretical approach which is capable of describing the dephasing and correlation effects of a 2DEG.

## 2.6 The two dimensional electron gas

The presence of a Fermi sea of electrons drastically changes the optical properties of a quantum well. In an undoped semiconductor, the correlations in the ground state are often not considered, because they are high energy and can adjust almost instantaneously to the dynamics of the near–bandgap carriers. Thus the ground state, except for providing the band structure and dielectric screening, can be considered rigid. In a doped system, the presence of electrons in the conduction band implies low energy excitations which can alter the dynamics of the photo–excited electron–hole pairs.

The 2DEG causes several differences from the undoped case, such as the restriction of phase space available for excitation or scattering of conduction electrons, due to the Pauli exclusion principle. The presence of electrons in the conduction band changes the optics, since a photo–excited electron cannot be placed in a state which already contains a doped electron. This forces a relationship between the optical properties of the sample and the filling factor, or the number of filled Landau levels, defined as $\nu = N_e/D = 2\pi l_c^2 N_e \propto 1/B$.

We will detail the dependence of the linear absorption on $\nu$ in chapter 4.

More striking are the Coulomb correlation effects, even in the ground state, caused by the 2DEG. The electron–electron interaction causes a renormalization of the band energies, and also of the electron–hole Coulomb interaction. The many–body states introduced by coupling to the low energy excitations of the Fermi sea will also affect the optical properties. The shake–up of the electron gas in response to the photo–excitation of an electron–hole pair creates the Fermi edge singularity (FES), a strong enhancement of the absorption at the band edge, similar to that seen in the X–ray spectra of metals [77]. Instead of forming a one electron–one hole coupled system (an exciton), the excitation creates a many electron–one hole collective state. The linear optics the FES have been studied both experimentally [101, 61] and theoretically (see ref. [81] and the references therein). Understanding the nonlinear optical response of the FES requires a treatment which goes beyond the DCTS to account for the presence of the Fermi sea [85, 106, 94, 88]. It is this technique which we will use to interpret our work on doped samples in a large magnetic field.

The high–mobility 2DEG in a magnetic field is a strongly correlated system, and these correlations lead to unusual experimental behavior, such as the quantum Hall effect. Transport and linear optical experiments have been successfully used to study some of the unique properties of this system [95, 113, 51, 36, 1]. While the intra– and inter–Landau level excitation spectrum has been predicted [33, 45, 66], only a few experiments in electron tunneling or Raman scattering [27, 92, 91] have successfully accessed this information. We will be interested in how these excitations affect the dynamics of the photo–excited system.

At high field, when the Landau levels are well separated from one another, it costs

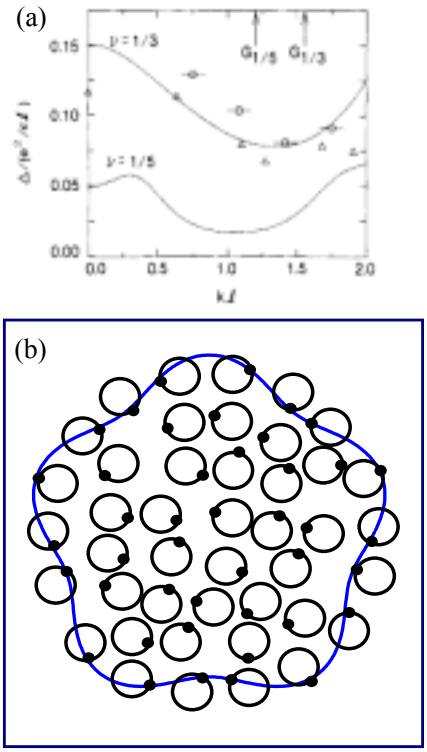


Figure 2.5: Magnetorotons. (a) The calculated dispersion curves for intra–Landau level excitations at fractional filling. From Girvin *et al.* [33]. (b) Cartoon of the development of a magnetoroton excitation from the phase of single electron orbits.

an energy $\sim \omega_c$ to create an inter–Landau level excitation. But there is another energy scale for the electron gas: the Coulomb interaction potential is $\sim e^2/l_c$. For fields of $B \sim 10$T, this energy is less than the cyclotron energy, and we can assume that there are intra–Landau level excitations, which exist entirely within a single Landau level. It has been shown [33] that the same theory used by Feynman to explain the excitations of liquid Helium can also be used to explain the intra–Landau level excitations of the two dimensional electron gas in a large field. The dispersion curve for these excitations, shown in Fig. 2.5(a), exhibits a minimum at a characteristic energy, in parallel with the roton mode in superfluid helium. In the quantum Hall community, these objects are called magnetorotons, and can be thought

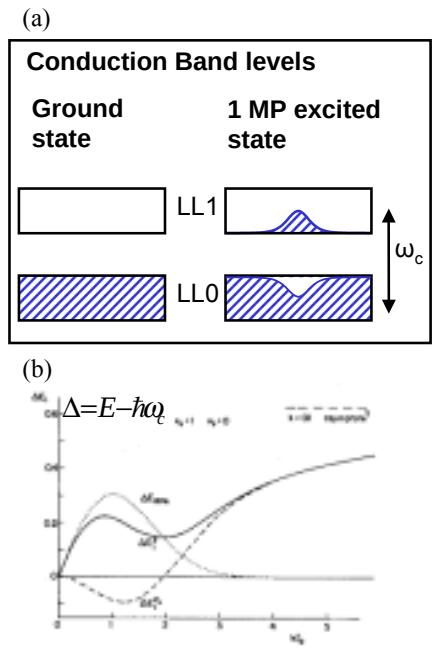


Figure 2.6: Magnetoplasmons with completely full Landau levels. (a) Cartoon showing the excitation of a magnetoplasmon. (b) The dispersion curve of an inter–Landau level excitation at filling factor $\nu = 1$. From Kallin and Halperin [45].

of as an excitation in which the electron density remains essentially constant, but there is a circular modulation built up from the phase of the single electron orbits, as shown schematically in the bottom panel of Fig. 2.5.

The inter–Landau level excitations are called magnetoplasmons, and are most easily understood when we have a completely full Landau level, as shown in Fig. 2.6. Promoting an electron from a full Landau level to the next highest empty level costs energy $\omega_c$. However, the removal of an electron leaves behind a hole in first level, which can interact with the promoted electron, similar to a magnetoexciton. This interaction must be taken into account to understand the structure of the excitation. The dispersion curve calculated for a full Landau level ($\nu = 1$) to first order in the Coulomb interaction energy $e^2/l_c$ is shown

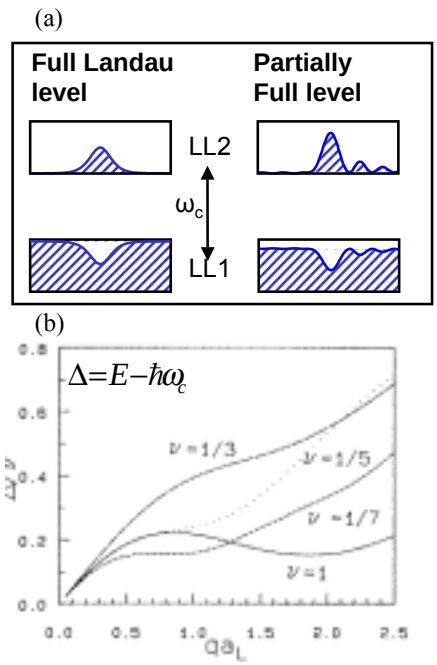


Figure 2.7: Magnetoplasmons with a partially full Landau level. (a) The excitation of a magnetoplasmon from a partially full Landau Level. (b) The dispersion curves of inter–Landau level excitations at partial filling. From Macdonald *et al.* [66].

in Fig. 2.6(b). This curve can also be obtained through a mean–field approximation.

The theory of intra–Landau level excitations discussed above has been extended to the calculation of the magnetoplasmon dispersion at partial filling [66], as shown in Fig. 2.7. Within the mean–field theory, any filling factor less than 1 should give the same dispersion curve as nu=1. If we think of the full level case as the creation of an electron–hole pair, similar to a magnetoexciton, than in a partially full level a magnetoplasmon is like an electron–hole pair accompanied by a shake–up of the electron gas. Note that for all filling factors, the excitation energy at long wavelength approaches the cyclotron energy. This is Kohn's theorem, a direct consequence of the translational invariance of the system in the x–y plane.

## 2.7 Conclusion

In this chapter, we reviewed the electronic structure of GaAs QW samples, and the effects of an applied magnetic field. We described FWM in atomic systems, and also how the Coulomb interaction changes the picture. We introduced the DCTS theory, which can explain FWM in undoped semiconductors quite well, and also explained why it breaks down in doped semiconductor samples. We also reviewed some of the correlations in a 2DEG, which will prove important in trying to understand our experiments in modulation doped QW samples.

# Chapter 3

# Experimental Setup

## 3.1 Introduction

This chapter provides a practical description of the two–pulse degenerate FWM experiments studied in this work. The geometry of such an experiment and the different measurements which were performed on the FWM signal, time integrated (TI) and spectrally resolved (SR) FWM, were described in the previous chapter.

We will begin with a description of the semiconductor samples used in the experiments, and the techniques used to process the samples for transmission measurements. Next we will describe the laser system and the layout of the optical table, including the magneto–optic cryostat used to apply the magnetic field and keep the sample at low temperature. We will then detail the process of aligning the experiment and detecting the FWM signal. We will end the chapter with descriptions of some additional measurements and calculations used to characterize the samples and evaluate the FWM measurements.

## 3.2 Samples

Several different semiconductor samples were used in the experiments described in this work. All the samples were GaAs/AlGaAs quantum wells (QWs) grown by molecular beam epitaxy (MBE). The modulation doped QWs (MDQWs) used for the 2 dimensional electron gas experiments were grown by the group of Professor Art Gossard at UC Santa Barbara. The undoped QW samples used for comparison were grown at Sandia National Lab. In all cases, the same overall sample design was used, the difference lying only in the thickness and dopant concentration of the active regions. The sample structures are shown in Fig. 3.1. To start off, MBE GaAs is deposited onto the wafer, as thick as necessary to ensure the growth of clean epitaxial layers on top of the substrate. This is followed by a $0.5\mu$m layer of $Al_{0.3}Ga_{0.7}As$, which will serve as a stop etch layer to ease in the substrate removal during processing. Also, the layer separates the active region from the surface so that band–bending effects are avoided. The active layers of the sample are grown next, followed by another layer of AlGaAs to protect the sample from surface effects. The top layer grown on the sample is a thin cap layer of GaAs, grown to prevent the oxidation of the AlGaAs layer.

The active regions of all the samples were several alternating layers of $Al_{0.3}Ga_{0.7}As$ and GaAs. The MDQWs are grown by adding donor dopants, in this case silicon, to the central 120Åof the AlGaAs layers. The concentration of electrons in the wells at low temperatures is a complicated function of the density of silicon dopants added, the distance between the silicon layer and the GaAs QW, and the ratio of aluminum to gallium in the barrier region. The electron density can be estimated by semi–classical solutions of

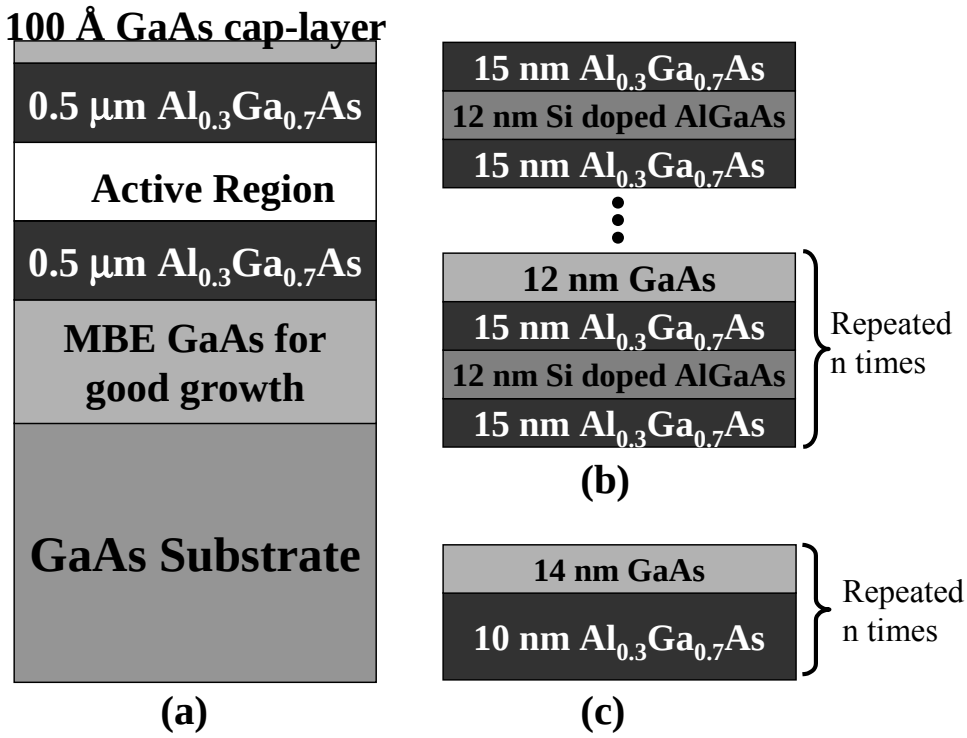


Figure 3.1: Structure of the MBE grown samples. (a) The general sample structure for all samples used. Also pictured are the active regions of (b) the MDQWs, and (c) the undoped QWs. The number of periods in the active region of the QWs n = 30 or 10.

Poisson's equation, but in practice the silicon dopant density and the barrier thickness must be adjusted by trial and error in order to fix the electron concentration. Several different MDQW samples were used in experiments. Two samples consisted of 30 periods of QWs with densities of 2.5 and 4.9 $\times 10^{11}$ electrons/cm$^2$ in each well, while one consisted of 10 periods with a density of $2.1 \times 10^{11}$ electrons/cm$^2$. The undoped QW samples were 10 period structures, consisting of 100ÅAlGaAs barriers and 140ÅGaAs wells. The properties of all the samples discussed in this work are presented in Table 4.1.

The samples must be processed before they can be used in transmission measurements, since the thick GaAs substrate on which the sample is grown absorbs the incident

laser light. To prepare the sample for transmission measurements, it was first anti–reflection coated, by depositing a $\lambda/4$ thick layer of $Sc_2O_3$, which has the correct index of refraction to minimize reflections off of GaAs surfaces (measured at 1.86), onto the polished surface of the wafer. A 2mm $\times$ 2mm piece was then cleaved from the wafer and glued, coated side down, to a sapphire window using UV cured epoxy (Norland optical adhesive 61). Sapphire was used because of its high thermal conductivity. The windows were 11mm in diameter and 1 mm thick, c–axis cut to avoid bi–refringence, but with a $1^\circ$ wedge to avoid interference from multiple reflections off the sapphire surfaces. The GaAs substrate was then sanded to a thickness of 100 $\mu$m, after which the remainder of the substrate was removed by a selective chemical etch, which dissolves GaAs greater than 10 times faster than $Al_{0.3}Ga_{0.7}As$ [56]. We used a jet etcher (Model 550D Single vertical Jet Electropolisher) to speed the etching process. After the stop etch layer was reached, the etched surface became very smooth. The etched surface was then anti–reflection coated as well, after which the sample was ready for transmission measurements.

## 3.3 The laser system

The laser used in these experiments was a Kerr–lens modelocked Ti:Sapphire laser, built from the NJA-2 kit, manufactured by Clark MXR. The laser produced output pulses with a temporal length (FWHM) between 90 and 400 fs, with an output power between 200 and 400 mW. The pulse repetition rate in this configuration, determined by the laser cavity length, was 100 MHz.

The laser was generally characterized by two measurements: the laser pulse spec-

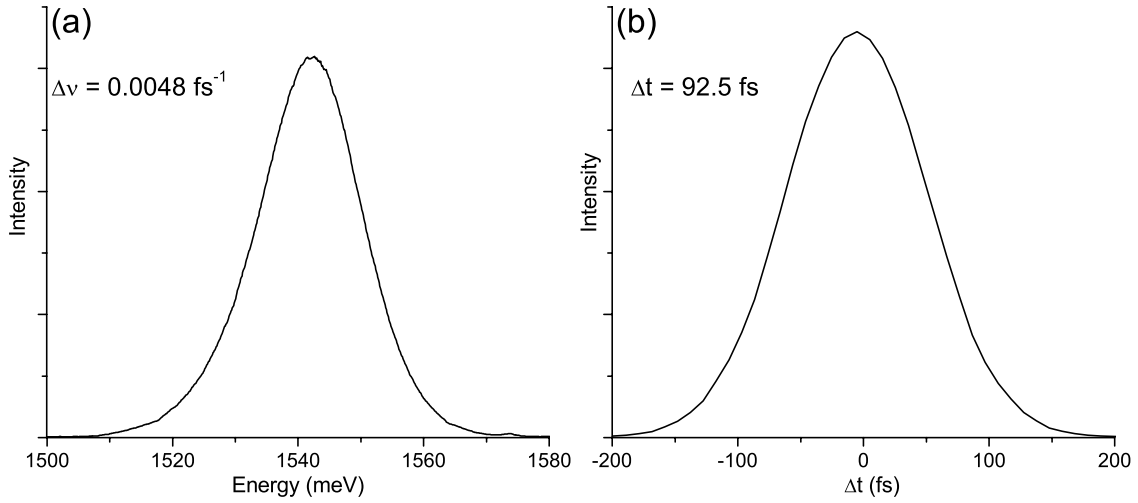


Figure 3.2: Typical laser spectrum and autocorrelation. $\Delta\nu\Delta t = 0.45$, where $\Delta\nu$ and $\Delta t$ are the FWHM values of the electric field intensity in the frequency and the time domain respectively. $\Delta\nu\Delta t = 0.4413$ for transform limited pulses.

trum and the autocorrelation (AC). The laser pulse spectrum was measured by sending a laser beam into a spectrometer (discussed in section 3.6). The AC was taken using the same two pulses used in the FWM measurements (beams 1 and 2 in Fig. 3.4), focused into a 0.5mm thick beta–barium borate (BBO) crystal. The BBO crystal was specially designed for second harmonic generation (SHG) of the 800 nm laser light. The two pulses were not colinear, so that the second harmonic generation at 400 nm propagated in a background free direction. The AC signal was detected with a Hamamatsu 931A photo–multiplier tube (PMT), and sent to a SR830 lock–in amplifier. The two beams were differentially chopped using a HMS double chopper, and the lock–in was referenced at the difference frequency. A typical laser pulse spectrum and AC measurement are shown in Fig. 3.2. The pulses were nearly Gaussian in profile, and within 10% of the transform limit. In some configurations, there was some structure in the wings of the laser spectrum, but the temporal behavior of

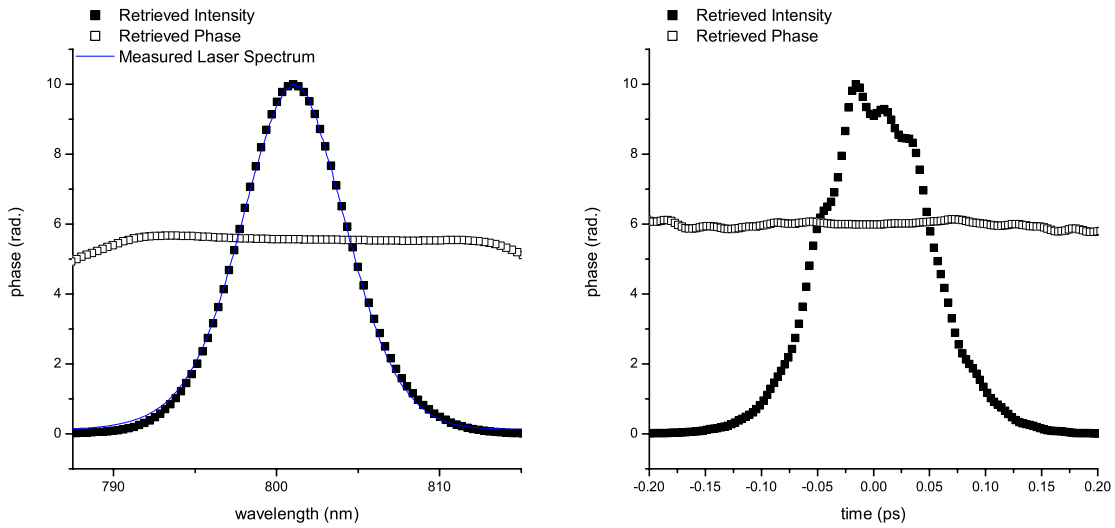


Figure 3.3: FROG measurement of the laser, giving both the phase and amplitude of the electric field pulse, in both frequency (left) and time (right). Courtesy of M. V. Marquezini

the pulses remained well behaved, and the experimental results were not affected by these abnormalities.

The laser was also characterized by frequency resolved optical gating (FROG)[26, 114]. For our measurements, the optical gate was the same BBO crystal used for second harmonic generation in the AC measurements. With this technique, both the amplitude and the phase of the electric field pulse can be determined. Fig. 3.3 shows the results of such a laser characterization. The pulse shape was well fit to a Gaussian, and the phase was essentially constant between the 2% points of the laser spectrum[71].

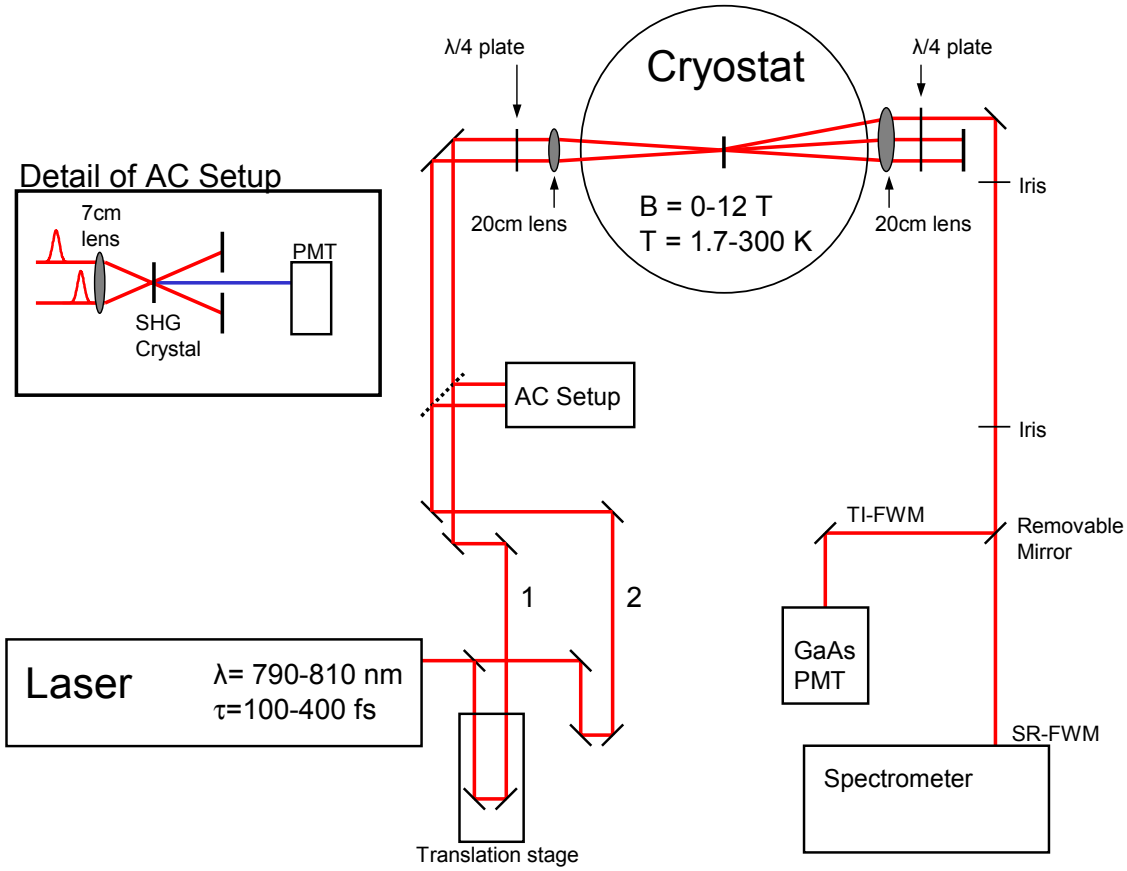


Figure 3.4: Layout of the optical table.

## 3.4 The experimental layout

The standard layout for FWM and pump/probe measurements is shown in Fig. 3.4. The output from the laser was divided into two equal intensity beams by a beamsplitter. The two beams were made to travel nearly equal length paths along the table, and then sent into the cryostat, described in detail in the next section, unless they are diverted into the AC setup shown in the inset to Fig. 3.4 by placing a mirror on a removable magnetic mount in the beam path. The mechanical stage in the path of beam 2 allowed us to adjust

the arrival time of beam 2 at the sample relative to the arrival of beam 1. The stage is a Klinger stepper motor, with 0.1$\mu$m step size, which allows time delay steps of 0.667 fs. The two beams were aligned parallel, approximately 1 cm apart and 14 cm above the table. The parallelism is confirmed by adjusting the separation between the beams at two points, one near the steering mirrors and the other several meters away.

Two mirrors aligned as a periscope were used to raise the beam to a height of 30 cm, to be sent through the cryostat windows. The beams were then sent through a zero–order $\lambda/4$ plate, which enabled us to change the polarization of the incident light from linear to circular, with a degree of polarization better than 99.9%. After the wave plate, the beams were focused into the cryostat using a two inch diameter, 200 mm focal length lens. The angle between the beams, or $\vec{k}_1$ and $\vec{k}_2$, was $2^\circ$.

To align the beams for a FWM measurement, they were first aligned parallel as carefully as possible. The time delay zero was found next by finding the AC signal. The zero delay given by the AC did not correspond exactly to the zero delay at the sample, because the AC was not taken at the same position, but they were never more than 100 fs different. The exact FWM zero delay could be determined by measuring the signal in both the $2\vec{k}_2 - \vec{k}_1$ and $2\vec{k}_1 - \vec{k}_2$ directions. These measurements should be symmetric around zero time delay. The next step to find the FWM signal is to get good spatial overlap at the sample. In practice, this was most easily accomplished by measuring and maximizing the pump/probe signal. It can also be done by imaging the sample surface with a CCD camera and looking for the interference of the two beams. However, because of the small aperture of the magnet windows, this was often difficult to see. Once the beams were spatially and

temporally well aligned, the FWM signal would be visible on either side of the transmitted beams with an infrared viewer. It is necessary to block the much stronger fundamental beams directly after the cryostat to see the weaker FWM signal in this way.

After the cryostat, all three beams (with wavevectors $\vec{k}_1, \vec{k}_2$, and the FWM signal $2\vec{k}_2 - \vec{k}_1$) were re–collimated with an identical 200mm focal length lens, sent through another $\lambda/4$ plate to restore linear polarization, and returned to a height of 14 cm by another set of periscope mirrors. The FWM signal was then sent directly through two irises which serve to align the beam into the detection setup. For pump/probe or linear absorption measurements, one of the fundamental beams would be aligned through the irises instead.

## 3.5 The magnet

The samples were measured inside a magneto–optic cryostat, which was designed and built by Oxford Instruments, Inc. The magnet itself was a superconducting split–coil magnet which operates between 0 and 12 Tesla, and is uniform to better than 0.25% within a 10mm diameter volume in the center of the coils. A cross section of the magnet is shown in Fig. 3.5. A variable temperature sample cell created a sample space in the uniform area of the magnetic field, with optical access both along the magnet axis and perpendicular to the field direction.

The samples were fixed to a flat metal sample holder with teflon tape. The sample holder was then mounted onto a 112cm sample arm, which was inserted into the sample cell. Once thermal equilibrium was reached, the sample position was stable to within 5$\mu$m.

A capillary tube connected the sample space to a helium reservoir. By opening a

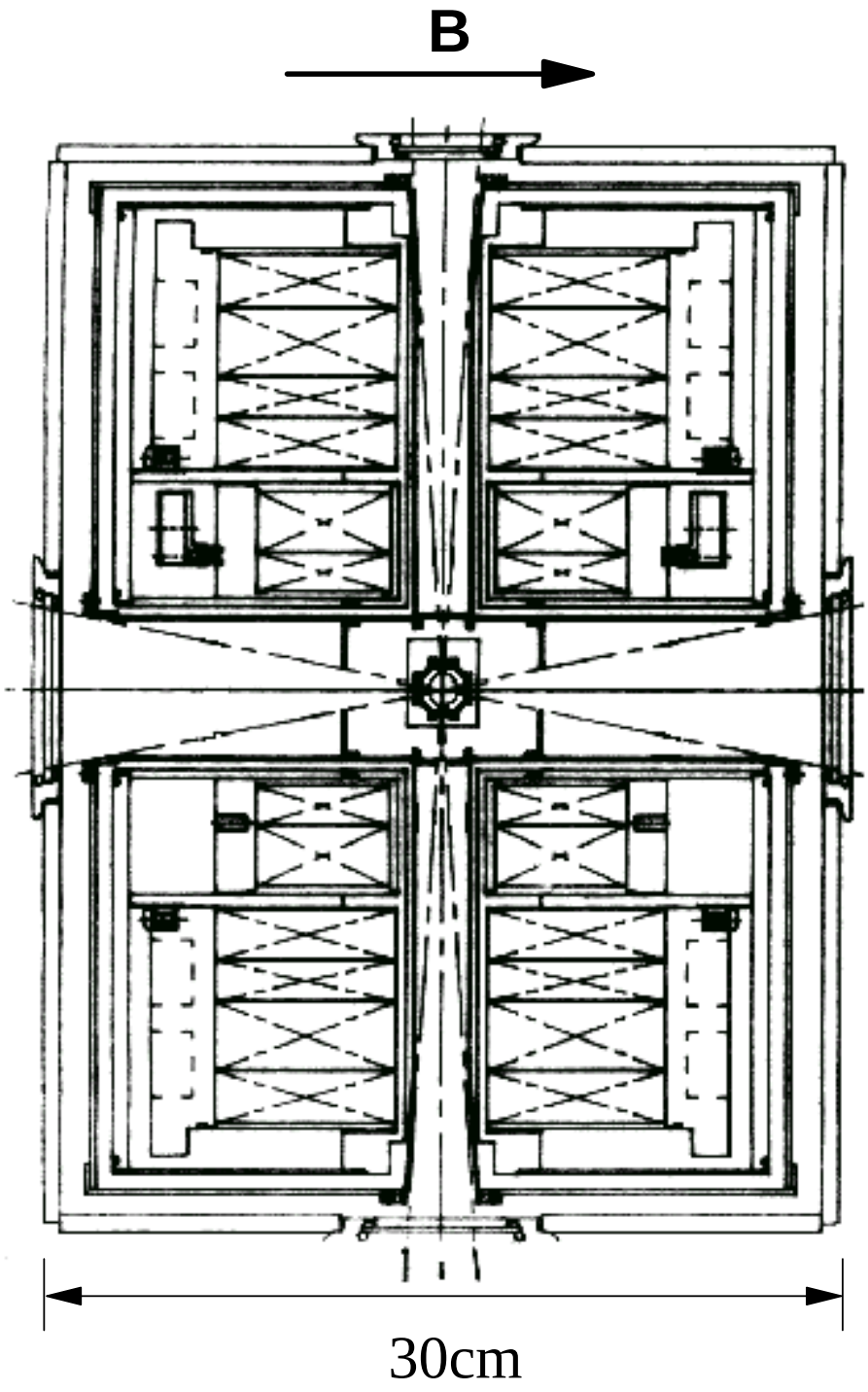


Figure 3.5: Magnet cross–section. The angular aperture is 25.5°.

needle valve in the capillary tube and pumping on the sample space, it was possible to fill the bottom of the sample cell with superfluid He4 at a temperature of 1.7K. The temperature of the sample was measured with a carbon–glass resistor mounted onto the sample holder.

There was also a temperature sensor and a resistive heater mounted at the base of the sample cell. By regulating the flow of helium into the sample cell and controlling the voltage applied to the heater automatically, the sample temperature could be controlled with a feedback loop. In practice, the flow of helium was kept constant, and a stable sample temperature could be reached simply by changing the power dissipated in the heater. We used an Edwards RV12 rotary vane pump with a displacement of 7 cfm to pump on the sample cell, which brought the sample to a temperature of 1.7K with a pressure of 5 torr in the sample cell.

## 3.6 Four–wave mixing measurements

In a FWM experiment, the FWM process, in which 2 light pulses arrive at the sample and cause the emission of a FWM pulse, is actually repeated at the repetition rate of the laser (∼every 10 ns), and the total power of the FWM signal is measured. In TI-FWM measurements, the entire signal was sent directly into a PMT, and the total power was measured as a function of the time delay, $\Delta t$. We used a RCA-C31034A PMT with a GaAs photocathode, in a Products for Research housing. For typical measurements, the PMT was biased at -1000V, and the FWM signal reduced by a factor of 300 before being sent into the PMT. To improve the signal to noise, the input beams, $\vec{k}_1$ and $\vec{k}_2$, were differentially chopped with a HMS light chopper, and the PMT output was converted to a

voltage using a trans–impedance preamplifier, and then measured with the SR830 lock–in amplifier, referenced to the HMS chopper frequency. The signal was then measured as the time delay of pulse 2 was varied.

In SR-FWM measurements, the power of the FWM emission was measured as a function of the emission wavelength, at a given time delay. The spectral resolution was provided by an Acton Research Corporation 750mm spectrometer (Spectra Pro 750). When possible, the signal was detected by an optical multichannel analyzer (OMA). A CCD array (Princeton Instruments) measured the spectrally resolved signal, which was sent to the OMA (Princeton Instruments controller ST-130), which was connected to the computer via an ISA serial connection. There were three gratings installed in the spectrometer: 150 gr/mm, 600 gr/mm, and 1200 gr/mm. The most commonly used grating was the 600 gr/mm, which gave a dispersion on the CCD array of 0.054 nm/pixel. The spectrometer was calibrated using an Oriel argon calibration lamp. A background signal due to scattering and luminescence is subtracted by measuring the spectrum with each beam blocked individually, and subtracting these spectra from the SR-FWM signal. If this background signal was too large, the subtraction would not work well. In these cases, the spectrometer was used as a monochromator, and the signal at each wavelength was measured as a function of time delay separately using a PMT at the output slit and the lock–in amplifier. This method drastically reduced the background noise, since the lock–in would only record signal chopped at the reference frequency of the light chopper. However, measurements made this way took much longer to complete.

## 3.7 Data collection software

The lock–in amplifier and the Klinger stepper–motor driver were both connected to a PC with GPIB connections. The OMA was connected to the same PC using a serial ISA card, and the spectrometer was connected through the RS-232 serial port. In this way, the various electronics could all be controlled remotely by a single computer. The data was collected using three different programs written in Visual Basic.

The program which controlled the OMA had the OMA take one spectrum, downloaded it to the PC and displayed it on the screen. One scan could be read and saved as a scan of the dark current in the CCD array, and it was then subtracted from all future scans. The program was also capable of collecting an array of scans as a function of the stepper motor position. In this way it was possible to measure the SR-FWM signal as a function of both wavelength and $\Delta t$.

The other two programs were used to read data from the lock–in amplifier. The first would scan the stepper motor position, waiting at each value for a specified amount of time before reading the value measured by the lock–in. The other would scan the grating position of the spectrometer, waiting at each wavelength position for a specified amount of time before reading the value measured by the lock–in. This program could also be used to scan both the grating and the time delay, generating an array of data vs. both wavelength and $\Delta t$, as in the OMA program.

## 3.8 Sample characterization measurements

It was necessary to measure the linear absorption of each QW sample, to characterize sample quality, and to help the analysis of the nonlinear measurements. The absorption of the sample was measured by transmission using an incandescent light bulb as a source. The light was focused through a pinhole, and the outgoing light was then collimated with another lens, and polarized using a Glan–Thompson polarizer. The light was then focused onto the sample in the cryostat using the FWM setup, and the transmitted light was sent into the spectrometer. The light spectrum was taken both with and without the sample in place, and the absorption coefficient was calculated using Beer's law,

$$\alpha(\omega) = \frac{-1}{L}\ln\frac{I_t(\omega)}{I_0(\omega)} \tag{3.1}$$

where L is the sample thickness, $I_t(\omega)$ is the transmission sample measured through the sample, and $I_0(\omega)$ is the spectrum measured without the sample.

Because the pinhole is not a perfect point source, the spot size of the focused beam on the sample is larger than the laser spot. Therefore the inhomogeneity of the sample due to well width fluctuations and strain will result in a larger linewidth measurement for the absorption spectra taken in this manner.

Linear absorption measurements were also taken using the laser pulses themselves, after the FWM signal was aligned in the detection setup, by sending the probe beam, instead of the FWM signal, into the spectrometer. This allowed us to adjust the excitation to meet specific criteria while doing the FWM measurements. However, the energy range for which the absorption spectrum could be measured was smaller than when the light bulb was used. Also, fluctuations in the laser central frequency and structure in the wings of the laser

pulse spectrum created background and additional structure in the calculated absorption spectrum $\alpha(\omega)$, which needed to be corrected manually. This was usually done by direct comparison with the light bulb absorption spectra. The linear absorption spectra for our samples are presented and discussed in detail in Ch. 4.

## 3.9 Spot size measurements

In order to estimate the number of carriers created by the laser pulses during the experiments, it is necessary to measure the size of the laser spot when focused on the sample. Since the measurements were performed inside the magnet cryostat, the spot size measurement could not be made directly at the sample position. Instead the beams were steered alongside the magnet, along an identical length path to the actual experiment, and focused using the same lens. An amount of glass equal to the thickness of the windows of the cryostat was placed between the lens and the focal plane, to reproduce the FWM measurement conditions as accurately as possible.

The spot size measurements were performed by passing a knife edge through the focused beam and recording the intensity of the light transmitted past the knife edge. The knife edge, typically a razor blade, was mounted on a linear translation stage along the beam direction and on a Klinger stage, so the data could be collected automatically. The power as a function of knife edge position was then fitted to an error function, to extract the beam waist $w_0$ assuming a Gaussian ($\mathrm{TEM}_0 0$) beam profile. The fits were in general quite good. By adjusting the linear translation stage along the beam direction, we could calculate the beam waist as a function of the lens position.

A typical measurement of the beam waist was 26$\mu$m. This value is a lower bound for the spot size, since we can't be sure whether the sample was exactly at the focus of the laser spot inside the cryostat.

## 3.10 Excitation density calculations

Once the spot size and $\alpha(\omega)$ are known, we could calculate the density of carriers excited by the laser during the experiment. The derivation of the carrier density formula is given here. The total power absorbed per unit area in the sample is

$$\int d\omega I(\omega)\left(1-e^{-\alpha L}\right) \quad \mathrm{W/cm^2} \tag{3.2}$$

where $I(\omega)$ is the laser intensity, and L is the sample thickness. The average number of carriers created by one pulse, in each individual QW, per unit area in the QW plane, is

$$N = \frac{1}{N_W f}\int d\omega \frac{I(\omega)}{\hbar\omega}\left(1-e^{-\alpha L}\right) \quad \mathrm{cm^{-2}} \tag{3.3}$$

where $N_W$ is the number of periods in th QW structure, and $f$ is the laser repetition rate.

However, The laser intensity is not uniform in the radial direction (in the plane). We will approximate the intensity $I(\omega)$ by averaging the intensity for $r < w_0$. For a Gaussian beam, the average intensity over that disc is

$$\tilde{I} = \frac{1}{\pi w_0^2}\int_0^{w_0} 2\pi r dr I(r) = \frac{0.865 P_T}{\pi w_0^2} \quad \mathrm{W/cm^2} \tag{3.4}$$

where $P_T$ is the total power in the beam, as measured by a power meter (Newport model 815 with attenuator). We can pull the average intensity out front, and normalize the Laser pulse spectrum $L(\omega)$ so that $\int d\omega L(\omega) = 1$. This gives the total carrier density formula

$$N = \frac{0.865 P_T}{\pi w_0^2 N_W f}\int d\omega \frac{L(\omega)}{\hbar\omega}\left(1-e^{-\alpha L}\right) \quad \mathrm{cm^{-2}}. \tag{3.5}$$

The integral was calculated numerically from the absorption spectra and the measured laser pulse.

In some experiments described here, it was desirable to know the number of carriers excited only into a specific level. In this case, the integral in Eq. (3.5) was only performed over a small frequency window containing only that level.

This calculation only gives an upper bound for the carrier density. The spot size is a lower bound, as discussed above, the quantum efficiency of the system is assumed to be 100%, the absorption is not corrected to account for bleaching or reflection, and the power measured is higher than the power incident on the sample due to the optical components between the sample and the position the measurement was made.

# Chapter 4

# Linear Absorption Measurements

## 4.1 Introduction

In order to understand the nonlinear optical response of our samples, it is important to characterize the sample as completely as possible. In this chapter, we discuss the results of linear absorption measurements, which will help us to understand the optical response of the samples, and will therefore give a good framework for understanding the results of the nonlinear optical measurements presented in the coming chapters.

## 4.2 Linear absorption in semiconductor structures

The dipole allowed optical transitions from the four hh and lh bands to the conduction band in GaAs QWs are shown schematically in Fig. 4.1. The transitions are induced by circularly polarized photons ($\sigma^{\pm}$), which are pure spin states, and correspond to a selection rule of $\Delta m_J = \pm 1$.

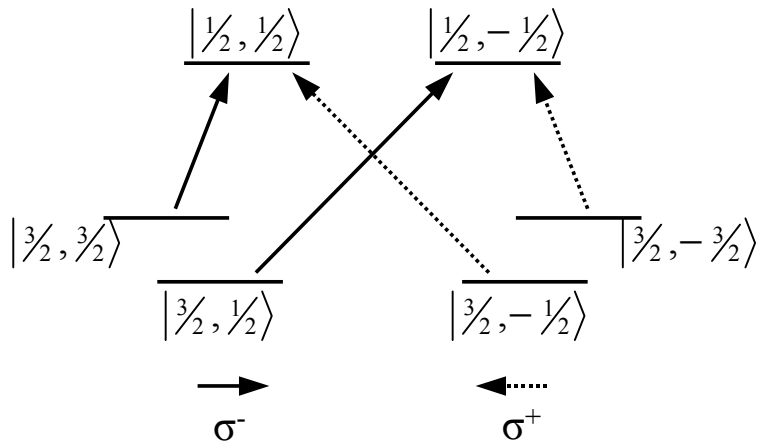


Figure 4.1: Selection rules for optical transitions across the bandgap.

The addition of a magnetic field lifts the degeneracy between the spin up and spin down conduction band states, as well as splitting the conduction band into a series of degenerate Landau levels. As discussed in Chapter 2.2.3, the dependence of the valence band structure on the magnetic field is complex, due to strong band mixing. Recall that the eigenvectors for the valence band states take on the four-component spinor form $(F_{3/2,n-2}, F_{1/2,n-1}, F_{-1/2,n}, F_{-3/2,n+1})$, where the first subscript is the $z$-component of the angular momentum $m_J$, and the second is the harmonic oscillator index which describes the nature of the Landau level associated with that $m_J$ state. The selection rules require, as above, that $\Delta m_J = \pm 1$. In addition, the photon can only couple states that have the same harmonic oscillator character $n$. For excitations into the lowest conduction band Landau levels, $n = 0$, The lowest energy transitions are shown in Fig. 4.2. All of the valence band states shown in this figure have the character of heavy holes at $B = 0$. These transitions were calculated to be the lowest in energy for GaAs QWs in high field [122]. As Fig. 4.2

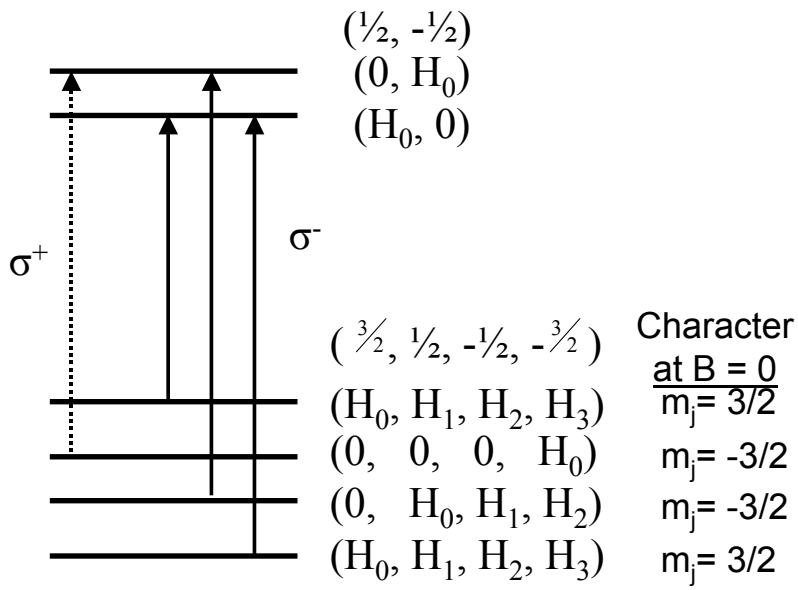


Figure 4.2: Selection rules for optical transitions in a magnetic field. Transitions can only be made to the lowest electron level, with harmonic oscillator index 0, from a valence band state with the same $n = 0$ character, and must also satisfy the change in angular momentum $\Delta m_J = \pm 1$.

shows, there are several transitions to both of the lowest electron Landau levels excited by $\sigma^-$ polarized light, and only one transition excited by $\sigma^+$. Because of this difference, we have performed our nonlinear experiments using $\sigma^+$ polarized light, to simplify the interpretation.

We have measured the FWM signal from numerous samples, both undoped QWs and MDQWs. I will discuss the results from several of these samples in the coming chapters. Some experiments were performed on other samples, not included in this work, to confirm our results. The doping levels and mobilities of the samples discussed here are given in Table 4.1. Here we present the linear absorption spectra from our undoped QW sample, sample D, and the spectra from one of our doped samples, sample A, to demonstrate the general features for the MDQW samples.

| Sample | A | B | C | D |
|---|---|---|---|---|
| Periods | 30 | 30 | 10 | 10 |
| Density ($\times 10^{11}$cm$^{-2}$) | 2.6 | 4.9 | 2.1 | undoped |
| Mobility ( $\times 10^4$cm$^2$/Vs) | 8.8 | 7.4 | 9.7 | N.A. |
| Field for onset of LL0 absorption (T) | 5.2 | 9.8 | 4.3 | N.A. |

Table 4.1: Properties for the samples measured in this work.

## 4.3 Absorption in undoped quantum wells

The absorption spectra presented here were measured using $\sigma^+$ polarized light from a light bulb as a broadband illumination source, as described in Ch. 3. The low temperature spectra for sample D at a series of magnetic fields are shown in Fig. 4.3. The spectra for $B = 0$T shows the heavy and light hole excitons, and the step-function like continuum of unbound exciton states. As expected, when the field is increased, the spectrum splits into a series of Landau levels. The valence band states complicate the picture somewhat, leading to a manifold of transitions for each Landau level. As mentioned above, using $\sigma^+$ polarized light helps to simplify this somewhat, although there are still pronounced heavy and light hole transitions to the lowest electron Landau level. Figure 4.4 shows the evolution of the energies and linewidths of the main (hh) transitions for the lowest Landau level (LL0) and the next highest level (LL1). The Landau level energy spacing increases linearly with magnetic field, as expected from the discussions in Ch. 2.2.2. The fluctuations in linewidth are relatively minor.

Absorption measurements were also taken with the laser pulse, in order to directly compare the absorption spectra with the FWM measurements taken at the same spot on the sample, in an attempt to avoid the sample inhomogeneity due to well width fluctuations and variations in strain. The LL energies are not significantly different in the laser

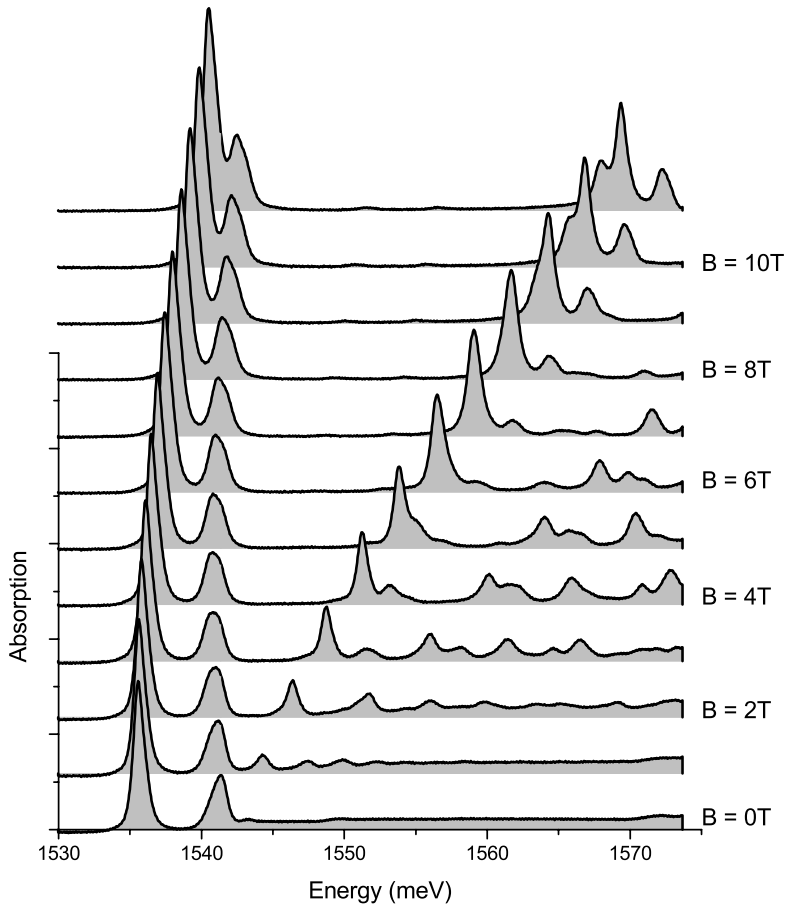


Figure 4.3: Absorption spectra of sample D in a magnetic field.

measurements, and the linewidths are only slightly narrower. The linewidths in the absorption spectra should correspond to decay times of the FWM measurements. The decay as a function of time delay for a homogeneously broadened system is $T_2/2 = \hbar/(2\gamma) \approx 0.4$ps for a typical linewidth measurement.

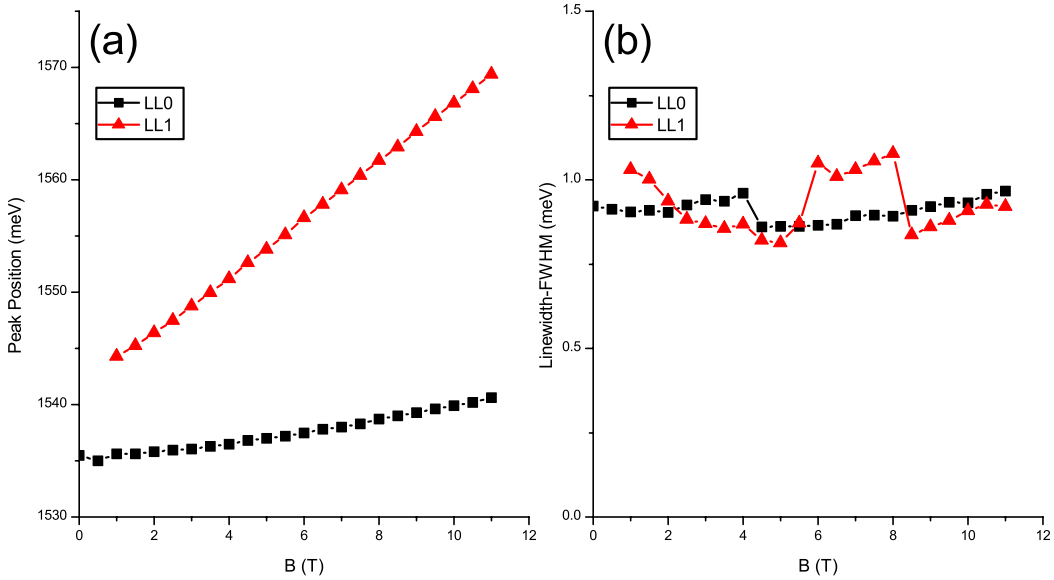


Figure 4.4: Peak energy and linewidth vs. magnetic field for sample D, for both the lowest (LL0) and next highest (LL1) Landau levels.

## 4.4 Absorption in modulation doped quantum wells

Even without the Coulomb interaction, the presence of the conduction band electrons changes the linear optics of the QW. The extra electrons fill the bottom of the conduction band, so additional electrons cannot be added to the system unless their energy is greater than the Fermi level. When the magnetic field is turned on, the electrons fill the lowest Landau levels. As the field increases, the degeneracy of each Landau level also increases. The filling factor is defined as $\nu = N_e/D = 2\pi l_c^2 N_e \propto 1/B$. At some field, all the electrons can fit into the lowest Landau level, with all the others empty ($\nu = 1$). It is only once we reach this point that we should be able to see absorption into the lowest Landau level. The effect of the increasing magnetic field on the filling factor is shown in the cartoon in Fig. 4.5.

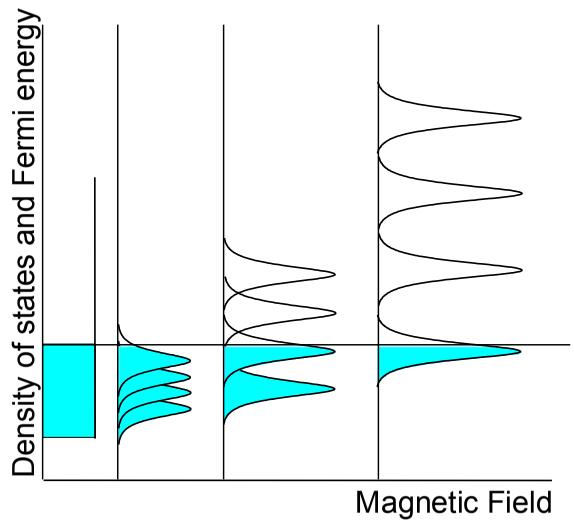


Figure 4.5: Filling factor dependence on magnetic field. As the field increases, we can fit more of the doped electrons in each Landau level, with fewer Landau levels completely occupied. Only in the final panel can we see the lowest Landau level in absorption measurements.

In addition to these phase space filling effects, the Coulomb correlation between the photo-excited electron-hole pairs and the Fermi sea leads to an enhancement of the band edge absorption, the so-called Fermi edge singularity (FES) at zero magnetic field. This enhancement can be seen in Fig. 4.6, which shows the low temperature absorption of both an undoped QW sample and a MDQW. The FES in MDQW absorption spectra has been studied in depth elsewhere [61, 81], and is not the subject of this work.

Figure 4.7 shows the linear absorption spectra of sample A, a MDQW, for many different magnetic fields. There are several differences between the doped and undoped sample absorption. In addition to the formation of the FES, we find that the presence of the doped carriers in the conduction band renormalizes the band energies and effective masses. This changes the cyclotron energy, and therefore the Landau level splitting at a given field. Also, as discussed above, the absorption into lower Landau levels only occurs

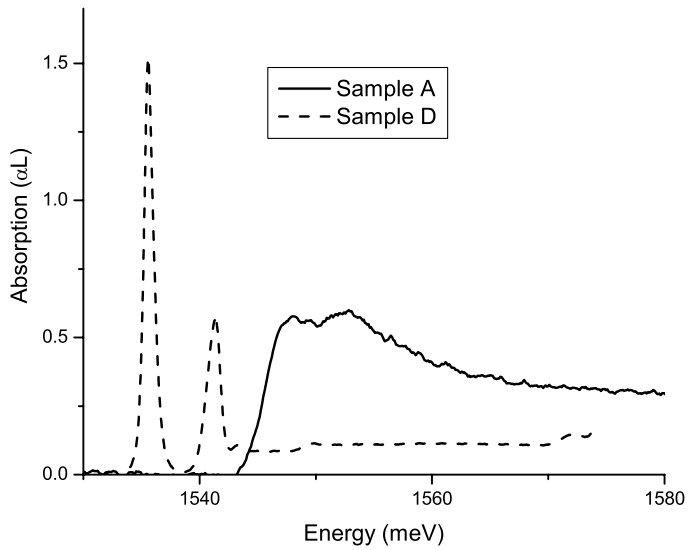


Figure 4.6: Absorption spectra of samples A and D at zero magnetic field. The solid line is the doped sample (A) showing a Fermi edge singularity from both the hh and lh valence band states, and the dashed line is the undoped QW (D), showing hh and lh excitonic transitions.

for sufficiently high fields, or low filling factors. Looking at Fig. 4.7, we can see the onset of absorption into the lowest Landau level, LL0, between $B = 5$T and $B = 6$T. Figure 4.8 looks at the peak height and area of LL0 as a function of the field. By extrapolating the LL0 peak height or area down to zero, we can confirm the doped carrier density. For sample A, the peak height and area reach zero at $B \sim 5.2$T, which confirms our electron density to be $n \approx 2.6 \times 10^{11}$ cm$^{-2}$.

Another difference appears in the linewidths of the Landau level peaks. Figure 4.9 shows the peak energy and linewidths of the lowest 2 Landau levels of sample A. While the linewidth of LL0 is approximately constant, the linewidth of LL1 increases significantly once LL0 starts to appear in the spectrum. This is an important point to notice: when the LL0 transition has finite oscillator strength, the LL1 peak is broadened significantly. Also,

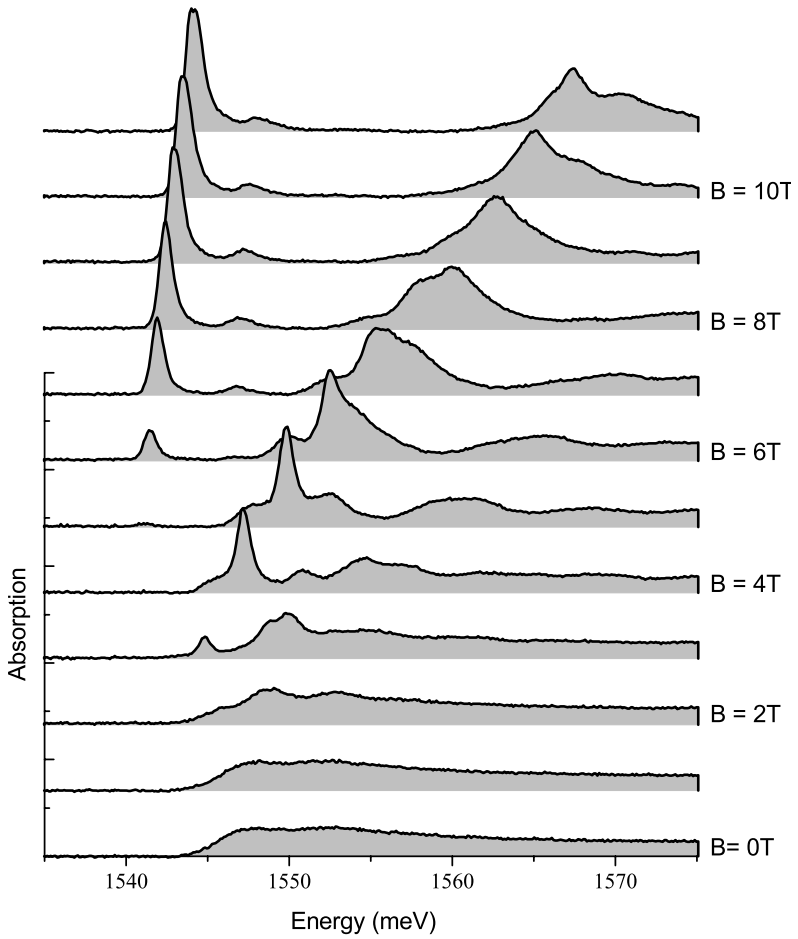


Figure 4.7: Absorption spectra of sample A in a magnetic field.

the LL1 peak seems to have a shoulder at higher energy. Although the broad peak disguises it, this shoulder is likely due to the lh LL1 transition, just as the small bump just above LL0 comes from the lh LL0 transition. In fact, the peak is quite well fit by two Lorentzian lines with comparable linewidths and a splitting roughly equal to the hh-lh splitting seen in LL0. The hh LL0 peaks are comparable in width to the undoped sample value, and are fairly well fit by a single Lorentzian line.

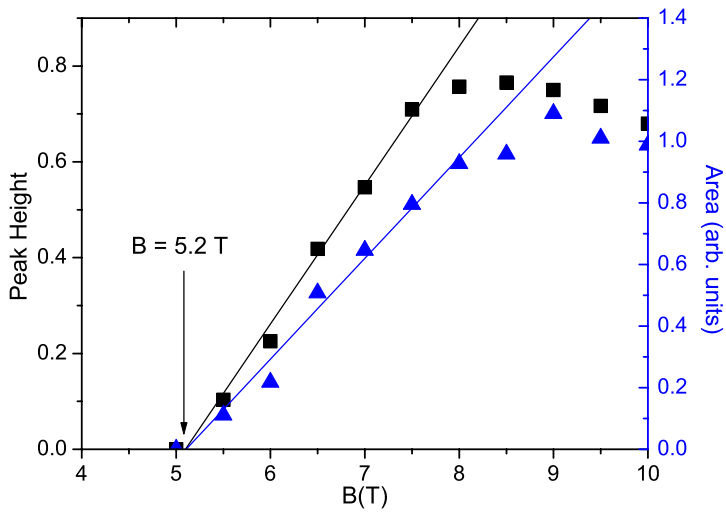


Figure 4.8: LL0 absorption peak height and area in a magnetic field, for sample A. Blue triangles are the peak area, black squares the peak height. Both extrapolate to zero at $\sim 5.2$T, giving a measurement of the density of doped electrons of $2.6 \times 10^{11}$ cm$^{-2}$.

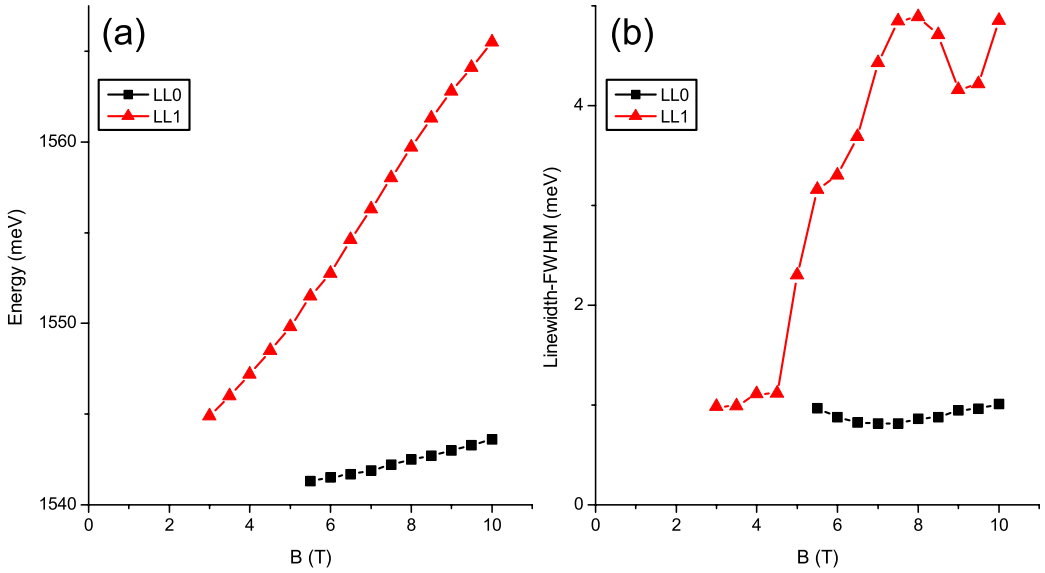


Figure 4.9: Peak energy and linewidth vs. magnetic field for sample A, for both the lowest (LL0) and next highest (LL1) Landau levels. Notice the sharp increase in the LL1 linewidth once LL0 starts to appear in the absorption spectrum.

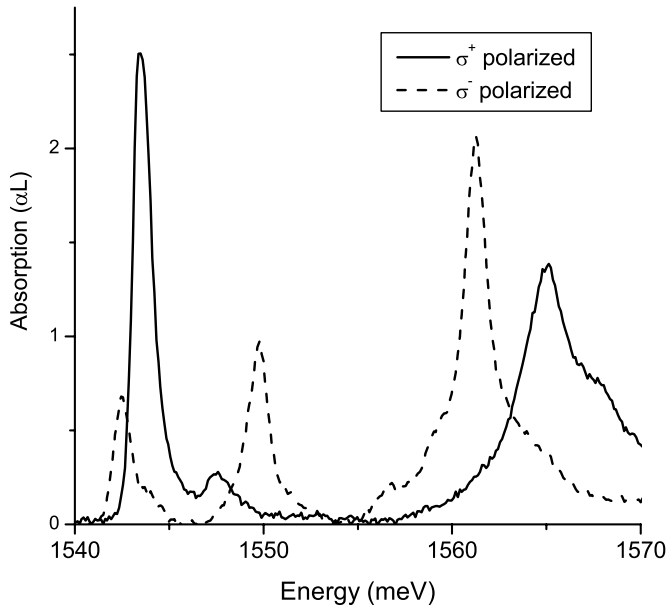


Figure 4.10: Absorption spectra for sample A at $B = 10$T, both $\sigma^+$ (solid) and $\sigma^-$ (dashed) polarized.

It is important to see how the absorption spectra is different for $\sigma^-$ polarized light. Figure 4.10 shows the absorption spectra at $B = 10$T for both the $\sigma^+$ and $\sigma^-$ polarizations. The $\sigma^-$ spectrum is more complicated, with a double peaked lowest energy transition, and an additional light hole peak a bit higher in energy. These additional peaks make analysis of the FWM signal more complicated, since the lowest peak is actually several transitions to different spin states of the conduction band (see Fig. 4.2).

A similar analysis to that above was performed on samples B and C. The absorption spectra as a function of magnetic field show the same qualitative features as described here. Transport measurements were also performed on all the doped samples to characterize the growth, and measured values for the electron mobilities are given in Table 4.1.

## 4.5 Conclusion

We have seen how the presence of the electron gas changes many of the linear optical properties. The excitons are no longer part of the linear absorption, but instead we find a strong FES at zero field. Also, at high field, the 2DEG in the lowest Landau level causes the higher transitions to broaden significantly. We shall see the effects of this behavior in the nonlinear optical response of the MDQW samples in Chs. 6 and 7.

# Chapter 5

# Intra–Landau level excitations

## 5.1 Introduction

In this chapter we investigate the dephasing of the interband polarization in a single Landau level (LL) which is partially filled by the 2DEG. We observe very strong variation of the interband dephasing time, $T_2$, as a function of the filling factor, as well as direct evidence of memory effects in the dynamics [32]. In a strong magnetic field, such that the 2DEG occupies only the lowest Landau level (LL0), there are no interactions between the photo–excited pairs, unless there is an asymmetry between electron and hole wavefunctions [57]. The concept of electron–hole symmetry was introduced in Ch. 2.2.2, and will be discussed in more detail in Ch. 7. When LL0 is partially filled, the dephasing originates mainly from the scattering of the photo–excited carriers with the intra–LL collective excitations of the strongly correlated 2DEG [33, 41, 91]. We present a model based on magnetorotons that accounts for most of the observed effects.

We will present the experimental results first, and then discuss the interpretation.

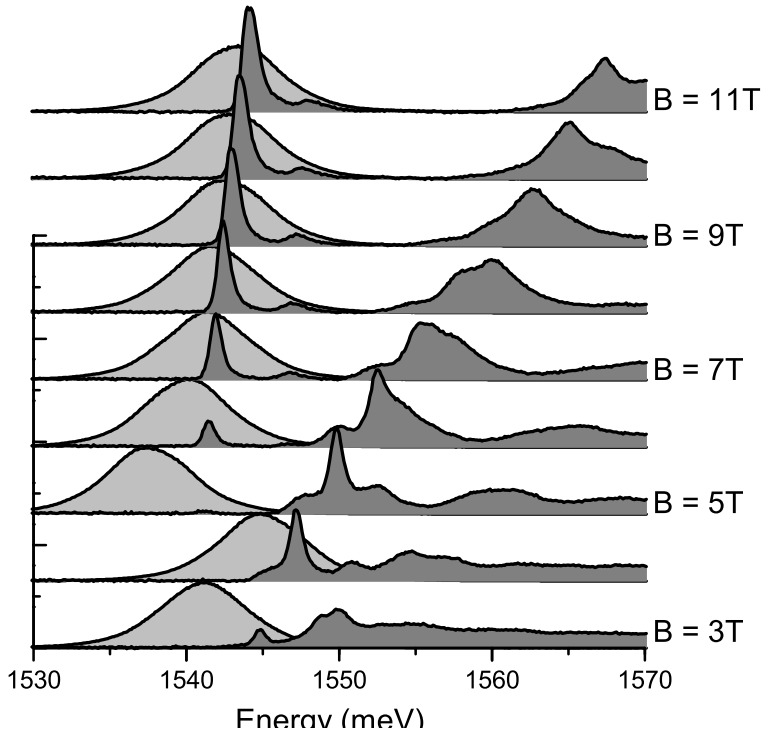


Figure 5.1: Absorption spectra and laser excitation of sample A. The light gray curves are the laser pulses, and the dark gray are the absorption spectra. The laser is tuned in this experiment to excite only into the highest partially occupied LL, i.e. to the Fermi energy.

We performed these experiments on samples A and B, which have carrier densities of 2.6 and 4.9 $\times 10^{11}\text{cm}^{-2}$ (see Table 4.1). Following the quantum Hall effect convention, we calculate the filling factor using the spin split LLs, so that the LL0 peak starts to appear at $\nu = 2$. We used spectrally narrow $\tau = 400$ fs laser pulses to resonantly excite only one LL in strong magnetic fields. The excitation intensity was kept low enough for the density of photo–generated $e$–$h$ pairs, $n_{eh}$, to remain small compared to the doping density of electrons, typically $n_{eh} \leq n/10$. In these experiments the pulses were tuned to excite electrons only into the highest partially occupied LL, which contains the Fermi energy, $E_F$. The excitation is detailed in Fig. 5.1, which shows the absorption spectra of sample A, and

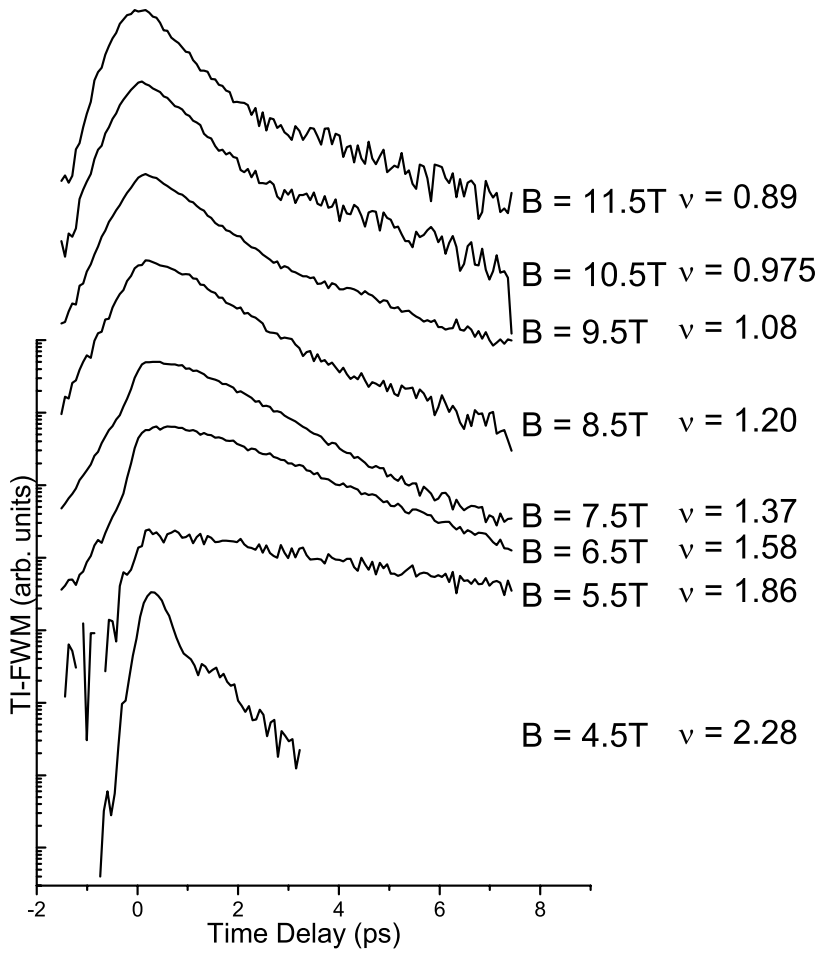


Figure 5.2: TI-FWM signal measured in sample A for $B = 4.5$ T$\rightarrow$ 11.5 T.

the overlap with the exciting laser pulses. We measured both TI-FWM and SR-FWM for the two samples.

## 5.2 Time integrated four–wave mixing

Typical measurements of the TI-FWM signal, $S_{TI}(\Delta t)$, in sample A are shown in Fig. 5.2, for $B = 4.5$ T$\rightarrow$ 11.5 T. For 5.5 T$\leq B \leq$ 6.5 T the $S_{TI}(\Delta t)$ profile is a single

exponential with an unusually long decay time, especially when we are close to the filling factor $\nu = 2$. For $B \geq 7.5$ T the profile is more complicated, showing non–exponential behavior for short time delays. By extracting an overall decay time we can get a direct measure of the interband polarization dephasing time $T_2$. This analysis of the experimental data to get the decay times is equivalent to the Markovian approximation (see Ch. 2.3.3), in which the memory kernel ($\Gamma(t - t')$) is replaced by a delta function ($\Gamma\delta(t - t')$). The results are displayed in the upper panel of Fig. 5.3 for sample A and in the lower panel for sample B. It is striking to note the very large jump of $T_2$ each time the system passes through even filling factors and in particular at $\nu = 2$. Since these features are reproducible as a function of $\nu$ for samples with different densities, we can assert that this is an effect of the cold 2DEG. Notice that as we approach filling factor $\nu = 2$ from below (higher field), the oscillator strength of the LL0 transition goes to zero, so that while the decay time gets very long, the signal becomes too weak to measure. Because of this, we cannot be measure the maximum value of $T_2$ in this case. Similarly, for filling factors below $\nu = 2$ (lower field), $T_2$ becomes very short, but we are unable to accurately measure this since the decay time becomes shorter than the $\sim$ 400fs pulse duration. In fact, the jump in dephasing time may be larger than what we have presented here.

## 5.3 Spectrally resolved four–wave mixing

The non–exponential behavior of the TI-FWM signal at high field is characterized by a change of slope that occurs in sample A at $\Delta t \approx 4.2$ ps$\rightarrow$ 2.5 ps as $B \approx 7.5$ T$\rightarrow$ 11.5 T. This change of slope indicates memory effects in the polarization dynamics, which are

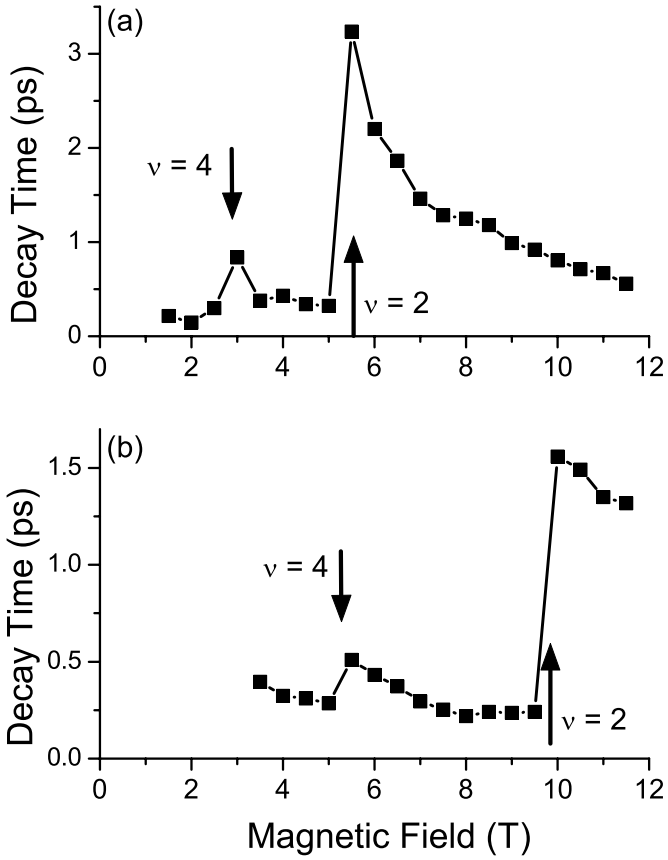


Figure 5.3: TI-FWM decay times versus magnetic field for samples A and B. The decay times were calculated by fitting the TI-FWM signal (shown in Fig. 5.2) to a single exponential decay curve.

also seen in the frequency domain. Figure 5.4 displays the SR-FWM signal, $S_{SR}(\Delta t, \omega)$, (a) at fixed $\Delta t = 0$ for $B = 5.5$ T$\rightarrow$ 11.5 T, and (b) at fixed $B = 11$ T for $\Delta t = 0 \rightarrow 6$ ps. Clearly the $S_{SR}(\omega)$ profile changes from a Lorentzian with a constant width, $\Gamma \propto T_2^{-1}$, to an asymmetric one that would correspond to a frequency dependent linewidth, $\Gamma(\omega)$. This occurs in sample A for $B \geq 7.5$ T at $\Delta t = 0$ , or for $\Delta t \leq 3$ ps for $B = 11$T. Such a profile indicates a polarization relaxation term $\propto \Gamma(\omega)P(\omega)$. As discussed in Ch. 2.3.3, a frequency dependent scattering rate $\Gamma(\omega)$ is a result of non–Markovian dynamics, or dephasing with

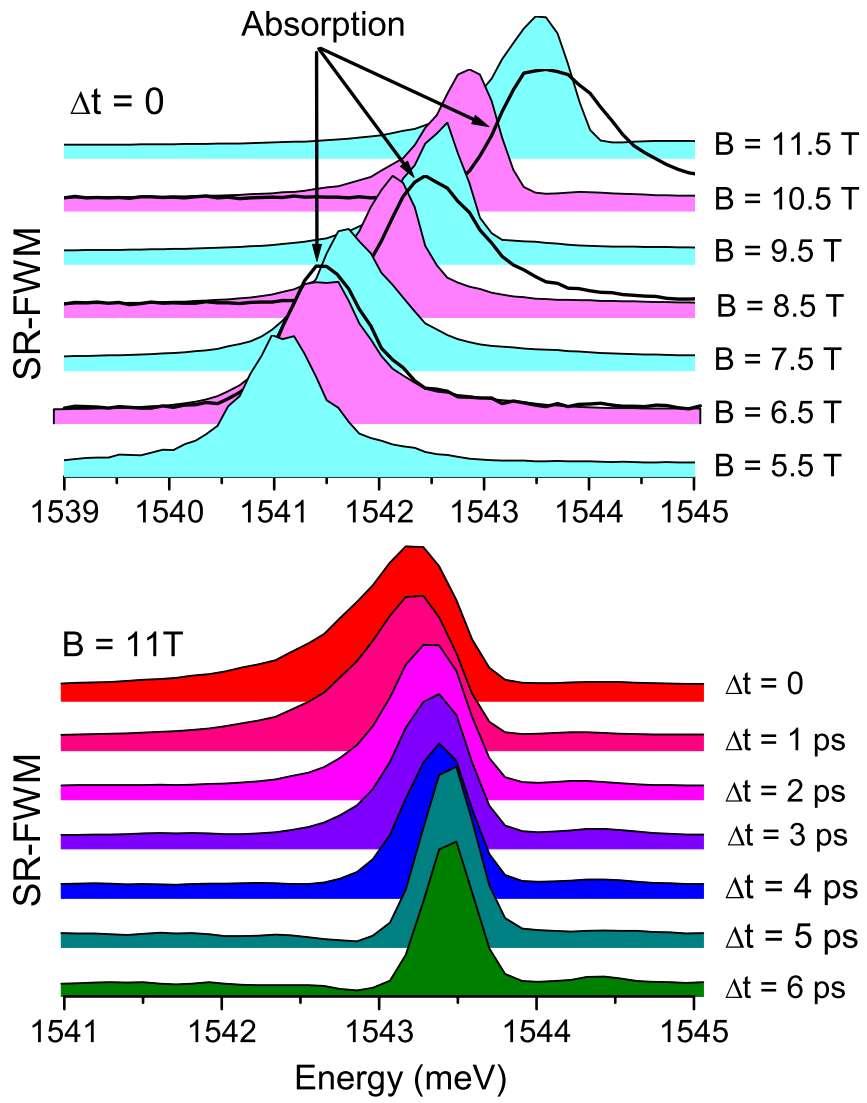


Figure 5.4: SR-FWM signal in sample A, (a) at fixed $\Delta t = 0$ for $B = 5.5$ T$\rightarrow$ 11.5 T, and (b) at $B = 11$ T for $\Delta t = 0 \rightarrow 6$ ps. The thick, unshaded lines in (a) show the linear absorption spectra, $\alpha(\omega, B)$, for $B = 6.5$, 8.5 and 10.5 T. (corresponding to the purple SR-FWM curves). Notice the asymmetric shape of the FWM peaks at higher field or at shorter $\Delta t$ , and the redshift of the peaks in those cases.

a memory kernel, which gives a scattering term $\propto \int \Gamma(t-t')P(t')dt'$ in the time domain. We note also that if the $S_{SR}(\omega)$ spectra are asymmetric, they are redshifted from the $\alpha(\omega)$, while if they are Lorentzian they almost coincide with the $\alpha(\omega)$ peaks. We will discuss this spectral shift at the end of the next section.

## 5.4 Interpretation

We would like to know what interactions cause these effects. The memory kernel within the lowest LL can be presented as $\Gamma(t-t') = (2\nu^{-1}-1)\kappa(t-t')$, where the factor $(2\nu^{-1}-1)$, expected on general physical grounds, is proportional to $N_s$, the number of empty states available for scattering within the LL containing $E_F$. It has the form $N_s \propto (2(N+1)-\nu)/\nu$ in the $N$th LL (factor of 2 for the spin).

As discussed in Ch. 2.6, there is an energy scale which for higher magnetic field is less than the cyclotron energy. The Coulomb correlation energy, $\sim e^2/l$ where $l$ is the magnetic length. It is these low energy excitations of the electron gas within LL0 that scatter with the photo–excited electron–hole pairs at high field.

In addition to scattering with the intra–LL collective excitations, there are several other relaxation processes which contribute to the dephasing at weaker fields, e.g., phonon and impurity scattering, Auger–like processes, etc. These background processes lead to Markovian dephasing, $\kappa(t) \to \delta(t)$, with $T_{2,bg} = [N_s F(B)]^{-1}$, where $F(B)$ depends only weakly on $B$ (mainly via inhomogeneous LL broadening). We have plotted $N_s^{-1}$ in Fig. 5.5, compared to the experimental $T_2$ points.

We have fit these curves to the experimental data by setting the maximum points

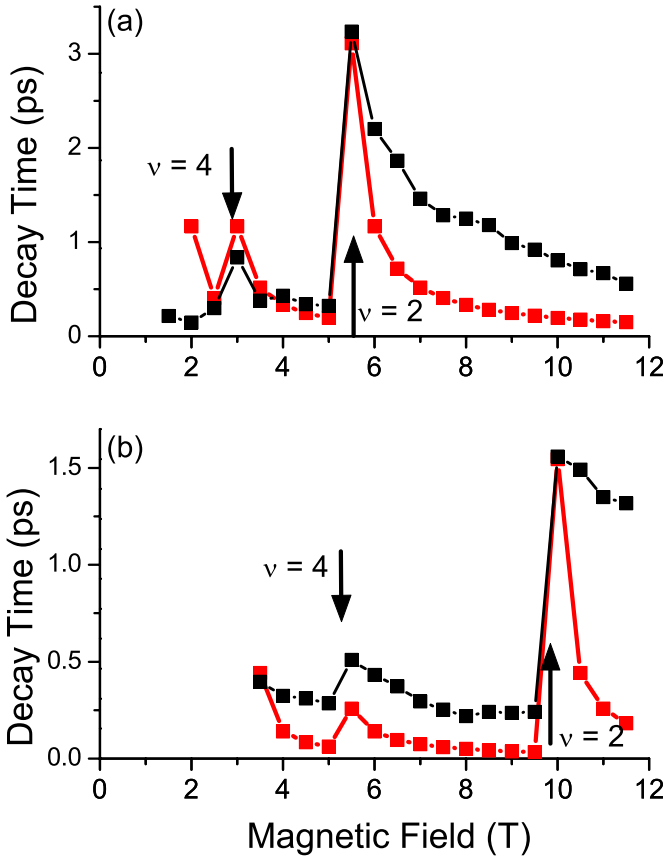


Figure 5.5: $N_s^{-1}$ versus magnetic field for samples A and B (in red), plotted over the experimental decay times for the TI-FWM signal (in black). For low fields, the agreement is quite good, but there are strong deviations at higher field.

equal to one another. As mentioned above, we are unsure exactly how high the maximum $T_2$ is, or how low the minimum value is. Nevertheless, the agreement is striking in terms of the location and magnitude of the steps. However, there are significant differences in the $B$–dependence of $T_2$ for strong field. In particular, the change in behavior occurs for sample A at $B \geq 7.5$ T, where we begin to see the non–exponential behavior in Fig. 5.2, or the asymmetry in Fig. 5.4. Also, above this field, the dephasing rate begins to differ considerably from $N_s^{-1}$.

We attribute this observed transition from Markovian to non–Markovian behavior to a suppression of the inter–LL scattering relative to the dynamical response of the collective excitations of the 2DEG. At large magnetic fields, where the cyclotron energy, $\hbar\omega_c$, is large compared to other characteristic energies of the system, relaxation is dominated by intra–LL processes. Scattering by collective excitations involves the matrix elements of the dynamically screened interaction, $U^{<}_{ij}(t,t')$, which in the lowest LL have the form:

$$U^{<}_{ij}(t,t') \quad = \quad \int \frac{d\mathbf{q}}{(2\pi)^2} e^{-q^2 l_c^2/2} v_q^2 \, \bar{\chi}^{<}_q(t,t') c_{ij}(q)\,, \tag{5.1}$$

where $\bar{\chi}^{<}_q(t,t') = \langle \bar{\rho}_{\mathbf{q}}(t')\bar{\rho}_{-\mathbf{q}}(t)\rangle$ is the density–density correlation function projected onto the lowest LL [34, 41], and $\bar{\rho}_{\mathbf{q}}(t)$ is the corresponding density operator. Also, $v_q$ is the unscreened Coulomb interaction, $l_c = (\hbar/eB)^{1/2}$ is the magnetic length, and $c_{ij}(q)$ (with $i,j \to e,h$) models the asymmetry in the electron–electron and electron–hole interaction matrix elements, which originates from the difference between electron and hole LL wavefunctions. Because of the breakdown of the perturbation theory due to LL degeneracy in 2D systems at high fields, it is incorrect to evaluate the strength of such scattering processes (or the interaction strength $U^{<}_{ij}(t,t')$) within the standard RPA theory of Ref. [39]. Instead, one should account for the true excitations of the interacting 2DEG. Several models can be found in the literature, and we base our discussion on the magnetoroton model (introduced in Ch. 2.6), which is the one best suited for our filling factors. The most salient features are, however, general and model independent. The scattering rates for the density matrix elements, i.e. interband polarization and occupation numbers, can then be calculated using the general non–equilibrium formalism given in Ref. [39]. The magnetoroton dephasing mechanism is somewhat similar to that of acoustic phonon scattering. In our experimen-

tal conditions to a very good approximation, the intra–LL collective excitations are not affected by the small density of photo–generated carriers, so one can use the equilibrium density correlation function [34], and

$$\left.\frac{\partial\hat{\rho}_{ij}}{\partial t}\right|_{scatt} = i\sum_k \int_{-\infty}^{t} dt' G_i^r(t-t')G_j^a(t'-t)$$
$$\times\left([U_{ik}^{<}(t-t') - U_{kj}^{<}(t-t')]\rho_{ik}^{<}(t')\rho_{kj}^{>}(t') - (<\leftrightarrow>)\right), \tag{5.2}$$

where $G_i^{r/a}(t)$ is the retarded/advanced Green function, $\rho_{ij}^{<} = \rho_{ij}$, and $\rho_{ij}^{>} = \delta_{ij} - \rho_{ij}$. If all $U_{ij}$ are equal, i.e. $c_{ij}(q) = 1$, then the polarization scattering term vanishes[57]. This corresponds to identical electron and hole wavefunctions in the lowest LL. In practice, there is always some asymmetry between electrons and holes, due to, e.g., differing band offsets and masses, lateral confinement and disorder, as discussed in Ch. 2.2.2. Using the results of Ref. [34], Eq. (5.1) takes the form

$$U^{<}(t) = -\frac{in}{2\pi}\int \frac{d\mathbf{q}}{(2\pi)^2} e^{-q^2l^2/2} v_q^2 c_{ij}(q)$$
$$\times \bar{s}_q[(N_q+1)e^{i\omega_q t} + N_q e^{-i\omega_q t}], \tag{5.3}$$

where $N_q$ is the Bose distribution function for magnetorotons of energy $\omega_q$, and $\bar{s}_q$ is the static structure factor of the 2DEG in the lowest LL. This contains the information about the dispersion relation of the 2DEG excitations, such as magnetorotons, in the lowest LL [34]. By studying Eq. (5.2), we see that the $\omega$ dependence of $\Gamma(\omega)$ is determined by the Fourier transform of $U^{<}(t)$, which is governed by the $q$ dependence of $\bar{s}_q$. In the lowest LL $\bar{s}_q = (2\nu^{-1}-1)\tilde{s}_q$ where $\tilde{s}_q \sim (ql)^4$ for $ql \ll 1$, $\sim \exp(-q^2l^2/2)$ for $ql \gg 1$, and $\tilde{s}_q$ displays a peak for $ql \sim 1$[34] that leads to the magnetoroton excitations. The corresponding resonance in $\Gamma(\omega)$ near the magnetoroton energy leads to non–Markovian behavior with a characteristic

response time of approximately the inverse of this energy. The latter is estimated from the gap at the magnetoroton dispersion minimum, $\Delta \sim 0.1(e^2/\epsilon l)$ for our range of $\nu$[33, 34], which for $B = 10$ T is $\approx 1.5$ meV.

The experimental results strongly support our interpretation, since they imply a reaction time $T_r \approx 2.5$ ps$\rightarrow$ 4 ps for the 2DEG collective excitations. We note that this corresponds to an energy $\approx 1$ meV$\rightarrow$ 2 meV. Clearly, a much more involved theoretical treatment is needed to identify the details of the interaction processes in this regime.

The non–Markovian behavior of 2DEG excitations is well documented at zero field, where the ultrafast nonlinear response of a Fermi sea of electrons is determined by the continuum of electron–hole pairs excited by the Coulomb potential of the photo–induced carriers. The small characteristic energy of these excitations gives rise to a non–adiabatic Fermi sea response leading to a non–exponential polarization decay (absent in the Hartree–Fock approximation) [85, 94]. We also see here (in Fig. 5.4) similar effects in the $B$– and $\Delta t$–dependent shifts of the SR-FWM signal. For large field, e.g., $B = 10.5$ T, $S_{SR}(\omega)$ is redshifted from the $\alpha(\omega)$ resonance due to a lowering of the 2DEG energy by the attractive potential of a photo–excited hole, a process similar to that known for the Fermi edge singularity [89, 90, 84]. This dynamical redshift comes from the real part of the magnetoroton–induced self energy. Since the latter is also proportional to $N_s$, the redshift is absent for nearly filled lowest LL, i.e., at $\nu \approx 2$ or $B \approx 5.5$ T (in sample A); the reason is that a 2DEG in an incompressible state cannot readjust to screen the hole potential.

## 5.5 Conclusion

In this chapter we investigated the quantum coherence of photo–excited electron–hole pairs within the lowest LL in MDQW samples the quantum Hall regime. We observed a clear transition from Markovian to non–Markovian behavior with increasing magnetic field. In the former case, the dephasing was dominated by inter–LL relaxation of the photo–excited carriers, and the $B$–dependence of the dephasing time followed that of the number of available scattering states, exhibiting peaks at even Landau level filling factors. At high magnetic field, the FWM signal showed strong evidence of memory effects. We proposed a model based on scattering of the photo–excited electrons with magnetoroton excitations in the lowest Landau level that qualitatively accounts for the main features of the experimental observations.

It is natural to ask how the 2DEG will alter the optical response of the MDQW samples when we tune the laser to excite carriers into the next highest LL, either in addition to or instead of the lowest LL. We will discuss these effects in the next chapter.

# Chapter 6

# Inter–Landau level excitations

## 6.1 Introduction

In this chapter, we present an investigation of the dynamics of the 2DEG inter–LL excitations. We observe strong, time dependent Coulomb coupling between the LLs induced by the 2DEG, enhancing the LL0 signal. The latter shows unusual behavior as a function of time delay, which cannot be understood in terms of the RPA. These results are compared directly with measurements on undoped quantum wells (QWs). We will study these results as a function of several experimental parameters, and also set the stage for an in depth theoretical analysis, which will be presented in Ch. 7.

These experiments were performed on sample C, a multiple period modulation doped quantum well (MDQW) whose active region consists of 10 periods of a 12 nm GaAs well and a 42 nm $Al_{0.3}Ga_{0.7}As$ barrier, the central 12 nm doped with Si. The carrier density is $n = 2.1 \times 10^{11}$ cm$^{-2}$ (see Table 4.1). Again, for most of the measurements in this study, the total number of carriers excited by the laser was kept below $2 \times 10^{10}$ cm$^{-2}$, or $n/10$.

We will discuss the dependence of our results on the excitation power later in the chapter. Comparison measurements were made on sample D, an undoped QW structure with similar well and barrier sizes. We used two criteria for these comparisons, by tuning the laser (i) to excite the same number of electron–hole pairs into each LL with a given laser pulse (The carrier density calculation is described in Ch. 3.10), or (ii) to produce the same FWM signal in the nonlinear susceptibility approximation, $S \propto |P^{(3)}|^2 = |\chi^{(3)}|^2 I_L^3$, where $P^{(3)}$ is the third order polarization, and $I_L^3$ the laser intensity. In our resonance conditions the third order susceptibility is assumed (based on single frequency calculations of the polarization) to be proportional to the square of the absorption coefficient, $\chi^{(3)} \approx (\chi^{(1)})^2 \approx Im[\chi^{(1)}]^2 \approx \alpha^2(\omega)$ [31]. The effects reported here were observed for comparisons using both criteria. We performed SR-FWM experiments, with a laser pulse duration of $100 \leq \tau \leq 200$ fs. The laser was tuned to excite varying proportions of the lowest LL (LL0) and the next highest LL (LL1), and the beams were $\sigma^+$ circularly polarized.

## 6.2 SR-FWM: Transfer of signal strength

Typical SR-FWM signals, $S_{SR}(\Delta t, \omega)$, for samples C and D are shown in Fig. 6.1, with the laser tuned to excite both LL0 and LL1 equally (laser and sample absorption spectra are projected on the back panels). Several unusual features are immediately apparent in the signal from the doped sample, $S_{SR}^{doped}(\Delta t, \omega)$, Fig. 6.1(a). The most striking is that despite an equal excitation of both LLs, the MDQW shows a LL0 signal which is 35 times larger than the LL1 signal. Measurement of the undoped QW, $S_{SR}^{undoped}(\Delta t, \omega)$, Fig. 6.1(b), shows almost equal emission from both LL's, in proportion to the excitation. Comparing

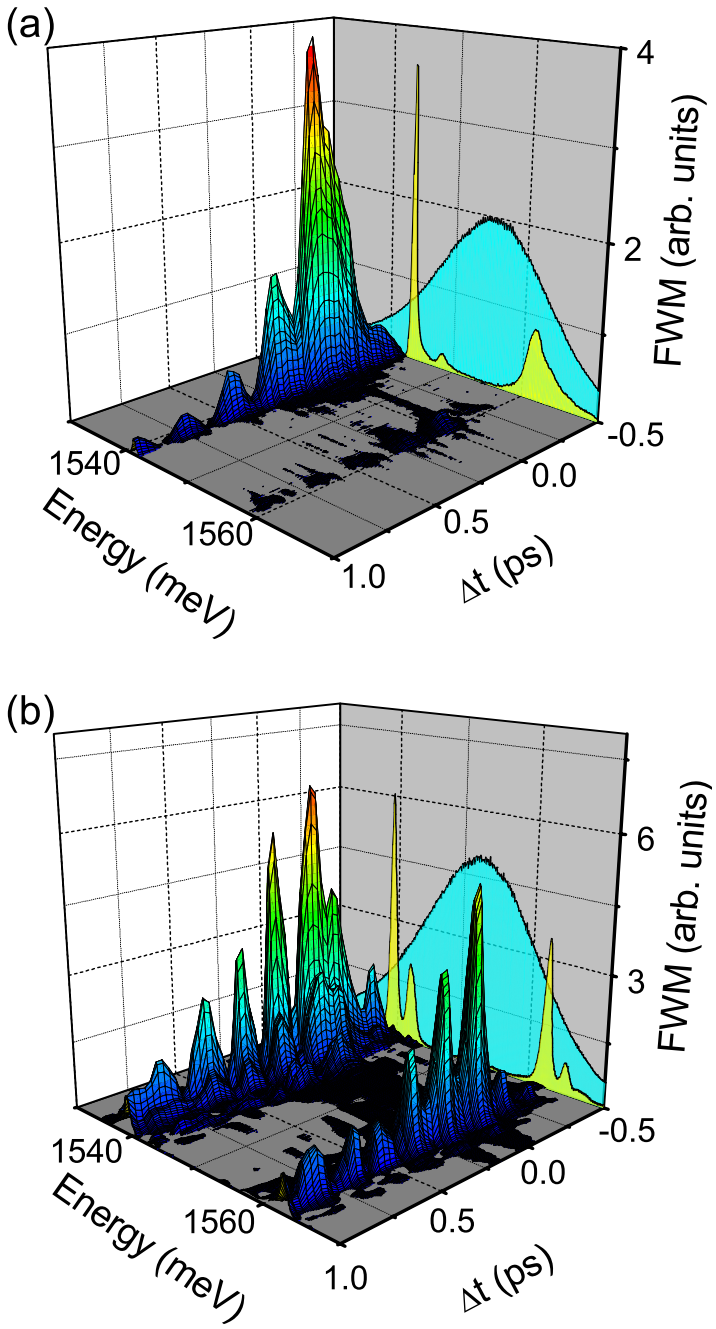


Figure 6.1: Spectrally resolved FWM signal at $B = 8$T for excitation of an equal number of electron–hole pairs into both LL0 and LL1, for (a) sample C, a MDQW, and (b) sample D, an undoped QW. The back screens show the laser and sample absorption spectra.

these figures to the results for a three–level atomic system, discussed in Ch. 2.4.2 and shown in the upper panel of Fig. 2.2, we see that the spectral distribution of the signal from sample D approximately follows the simple three–level atom picture, but the signal from the MDQW, sample C, is drastically different.

The picture only becomes more intriguing when we tune the laser frequency to excite mostly into LL1, with only the tail of the laser pulse exciting LL0. Figure 6.2 shows $S_{SR}(\Delta t = 0\ ,\ \omega)$, the FWM spectra for $\Delta t = 0$ , for both samples under these excitation conditions. It is clear that the signal from LL0 is greatly enhanced relative to LL1 in the MDQW. In the undoped sample, there is almost no signal from LL0, as expected from the excitation (60:1 excitation of LL1 over LL0, shown in the inset), while in the doped sample the LL0 signal is comparable to the LL1 signal. We can get an estimate for how large this enhanced LL0 signal is by comparing the relative emission of the two LLs with the excited carriers in each level. We define the relative emission ratio $R$ as

$$R = \frac{S_m^{LL0}/N_{LL0}}{S_m^{LL1}/N_{LL1}} \tag{6.1}$$

where $S_m^{LL0(LL1)}$ is the maximum signal emitted from LL0 (LL1), and $N_{LL0(LL1)}$ is the number of photo–excited pairs in LL0 (LL1). If the emission is in direct proportion to the excitation, as we expect from the FWM theory of Ch. 2, then we should find $R = 1$. $R > 1$ means that the LL0 signal is larger than expected from the excitation, while $R < 1$ means the LL0 signal is smaller than expected. For the signals shown in Fig. 6.2, we find that for the undoped sample $R^{undoped} = 1.3$, close to the expected $R = 1$, while for the MDQW sample $R^{doped} = 17.5$, a huge enhancement compared to the undoped signal. Since the calculated excitation densities are estimates, the value of $R$ is more of a guideline

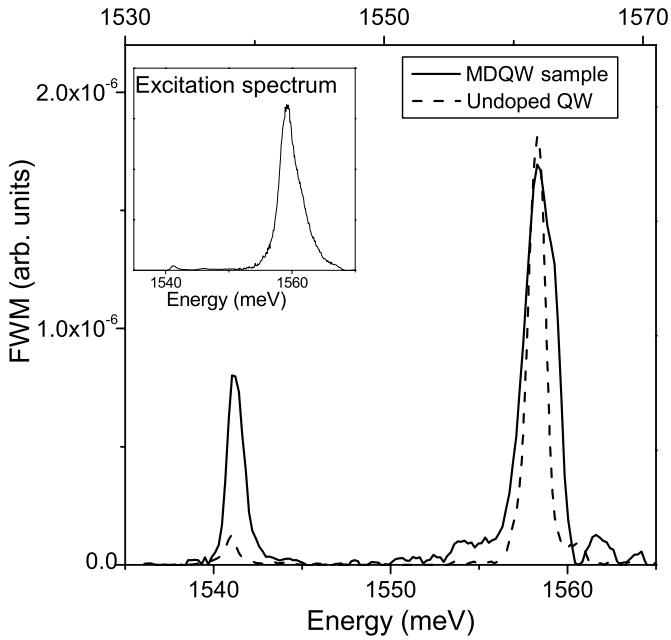


Figure 6.2: SR-FWM signal at B=8T, $\Delta t = 0$ ps from both sample C (solid) and D (dashed). The inset shows the excitation density spectrum, giving a ratio of 60:1 excitation of LL1 over LL0. The energy scales are different for the two samples, with the lower energy scale for the sample C.

than a precise measure of the enhancement. However, a difference of more than an order of magnitude is an unambiguous demonstration of the effects of the 2DEG on the FWM signal.

## 6.3 SR-FWM signal vs. time delay

### 6.3.1 Enhanced negative time delay signal

In addition to the transfer of oscillator strength to LL0, $S_{SR}^{doped}(\Delta t, \omega)$ also shows a very unique dependence on $\Delta t$ , seen most easily when the laser excites only LL1. According to the RPA theory for FWM in semiconductors, the rise time of the $\Delta t < 0$ signal should

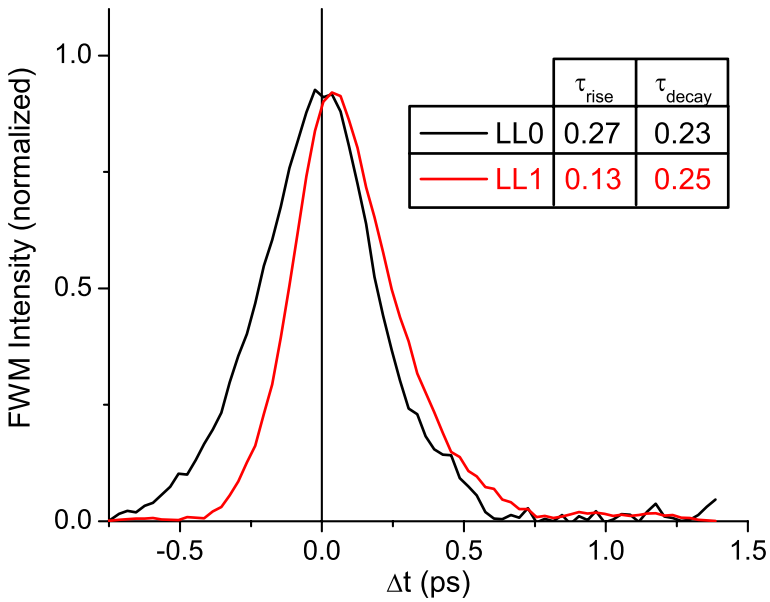


Figure 6.3: FWM vs. time delay $\Delta t$ for the MDQWs, sample C, at B = 8T. The black curve is the signal from LL0 and the red curve is from LL1. The laser is tuned to excite LL1 (60:1 over LL0), and the signals have been normalized for clarity. The decay time for both curves is $\approx$ 0.25ps. The rise time for the LL1 signal is 0.13 ps, as expected from mean–field theory, while for LL0 it is 0.27 ps.

be 1/2 the decay time for $\Delta t > 0$ (see Ch. 2.5.1), and this is the measured result for the undoped QW sample. This is also the measured result for the signal from LL1 in the MDQW, but surprisingly the signal from LL0 is almost symmetric as a function of $\Delta t$ , with comparable signals for $\Delta t < 0$ and $\Delta t > 0$. Figure 6.3 shows the dependence of $S_{SR}$ on $\Delta t$ for two values of $\omega$, corresponding to the maximum signal from LL0 and LL1, for sample C. Such a large signal for $\Delta t < 0$ can only be a result of correlation effects beyond the RPA [49]. However, the effect is only seen in the signal from LL0, and only in the doped sample, which implies that in this case the correlations are induced by the presence of the 2DEG in the doped sample. This will be discussed below, and in great detail in Ch. 7.

### 6.3.2 Beats in the FWM signal

Let us return to the case where the laser excites LL0 and LL1 equally. Although we saw emission almost entirely from LL0 (see Fig. 6.1), the signal has very pronounced beats as a function of $\Delta t$ , with a period given by the inverse of the energy difference between LL0 and LL1. Such strong beating in $\Delta t$ from only a single emission energy is a clear signal of non–Markovian dynamics. Comparing this to the signal from the undoped QW, we see that $S_{SR}^{undoped}(\Delta t, \omega)$ also shows beats, but from both emission peaks, as expected from the RPA theory of Ch. 2.5.1. This is made clearer in Fig. 6.4, which shows the dependence of the $S_{SR}$ on $\Delta t$ at the emission maxima of LL0 and LL1 for both samples. In addition, the beats in the signal from sample C are only pronounced for $\Delta t > 0$, and for negative time delay they are almost completely suppressed. In the undoped sample, the beats are stronger for negative time delay.

## 6.4 Summary

The results described above demonstrate the unusual experimental features exhibited by a QW sample containing a 2DEG in a magnetic field. The undoped QW sample, sample D, closely follows the expectations based on the RPA theory of Ch. 2.5.1. We see emission from LLs which are directly excited by the laser pulse, and quantum beating as a function of time delay, with a beat period given by $T_{beat} = h/\Delta E_{LL}$ where $\Delta E_{LL}$ is the energy difference between the LLs which emit the signal. The negative time delay signal decays roughly twice as fast as the positive delay signal, which is also an expected result of the mean–field theory. However, the signal measured from the MDQW sample, sample

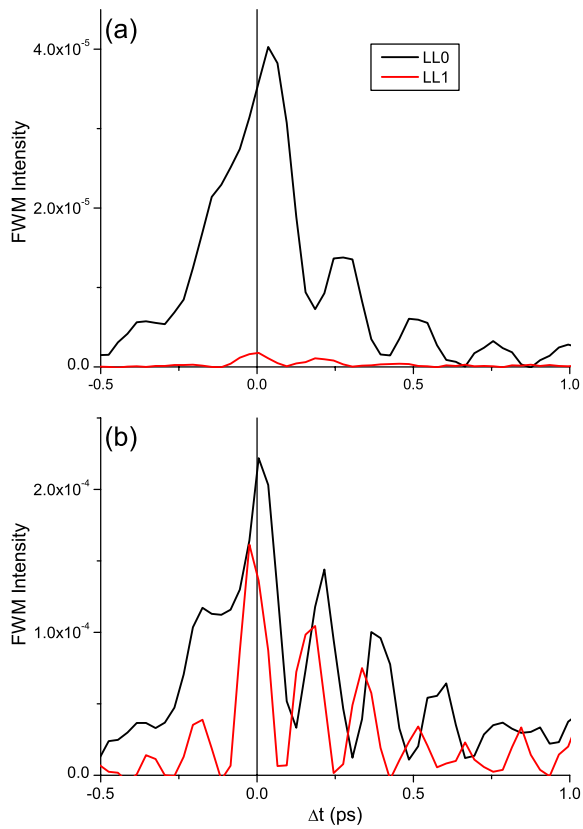


Figure 6.4: FWM vs. time delay for (a) sample C and (b) sample D at B = 8T, from the LL0 and LL1 maxima. The black curves are the signals from LL0, and the red curves are from LL1. The laser is tuned to excite both levels (LL0 and LL1) equally.

C, shows a large enhancement of the LL0 signal relative to the LL1 emission. When the laser is tuned to excite both levels equally, the LL0 signal dominates the LL1 signal, and when LL1 is excited 60 times more than LL0, the signals from the two levels are roughly equal. This corresponds to an enhancement of the LL1 signal which is more than an order of magnitude greater than the "normal" results of the undoped sample. When both levels are excited, we see strong beats from the LL0 signal, with the same period $T_{beat} = h/\Delta E_{LL}$, even though there is only emission from one level. When we excite LL1 preferentially, there is a strong enhancement of the LL0 signal for $\Delta t < 0$, so that it is as strong as the signal

for $\Delta t > 0$, with no beating. All of these effects are unexplained within the RPA theory, and are not seen in the undoped QW sample. We can conclude that these unusual effects are due to the interaction of the photo–excited electron–hole pairs with the 2DEG present in the MDQW samples.

Since we are exciting several LLs in these experiments, we expect that the inter–LL excitations of the 2DEG are important for understanding these results. These are the magnetoplasmons, discussed in Ch. 2.6. The magnetoplasmon (MP) energy is close to the inter–LL magnetoexciton energy, so we must account for the almost resonant creation and destruction of the MP excitations non–perturbatively. In particular, it is possible for a photo–excited LL1 electron to scatter into LL0 while exciting the 2DEG. The scattering to this new state provides additional dephasing for the LL1 photo–excited carriers, which will effect the FWM signal. Since this scattering process is nearly resonant, it is also possible that during the time evolution of the excited system, some of the excitation energy is temporarily stored in the MP excitation, leading to memory effects in the FWM signal. This process, which is analogous to coherent antiStokes Raman scattering except with MPs instead of phonons [58], is examined in more detail in the next chapter, when we investigate the 2DEG system theoretically. There we will show that we must include these nearly resonant exciton–2DEG interactions in order to understand the unusual effects in the optical response of the MDQW which we are describing here. For the remainder of this chapter, we will discuss some of the properties of the experimental effects, as we adjust various experimental knobs.

## 6.5 Properties of the MDQW signal

In this section, we will examine the dependence of the FWM signal from the MDQW, sample C, on the magnetic field, the excitation power, and the pulse duration. These experiments will help us to understand the nature of the correlation effects we have described above for the MDQW sample in a large magnetic field.

### 6.5.1 Magnetic field dependence

By changing the magnetic field, we confirmed that the beat frequency seen in the signal from LL0 when we excite both levels changes with the cyclotron energy, and is very close to the LL spacing. This is shown in Fig. 6.5, which shows $S_{SR}^{doped}(\Delta t\ )$ at the LL0 energy for $B = 6, 8$, and 10T when we excite both LL0 and LL1 equally. The inset shows a good agreement between the inverse beat period (in meV) and the LL spacing at several magnetic fields. Looking at the behavior of the signal from LL0 when we excite only into LL1, we see that the enhanced LL0 signal is only present for magnetic fields large enough that LL0 is partly empty (filling factor $\nu < 2$ in the quantum Hall notation). Figure 6.6 shows $S_{SR}^{doped}$ vs. $\Delta t$ at the LL0 energy for $B = 4, 6, 8$, and 10T when we excite directly to LL1 only. For $B > 4$T, we see similar curves (including the large signal for $\Delta t < 0$), but for $B = 4$T ($\nu > 2$) there is only a much weaker signal from LL0, and it does not have the symmetric time delay profile we see for the higher fields. We can infer that the enhancement of the LL0 signal only exists at magnetic fields for which there is available space in LL0 before the excitation.

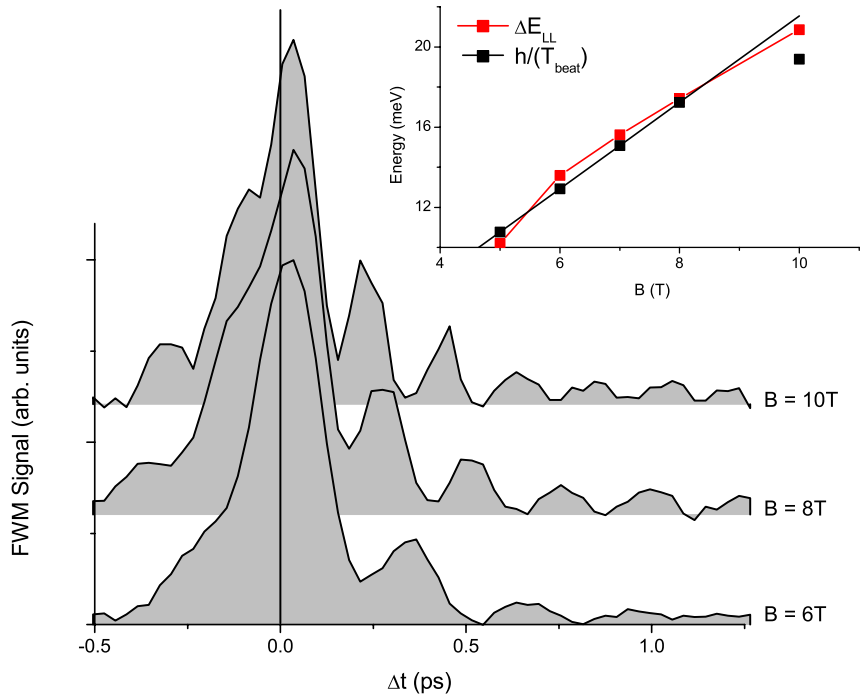


Figure 6.5: FWM emission from LL0 vs. time delay for sample C as a function of magnetic field, when the laser is tuned to excite both levels (LL0 and LL1) equally. The FWM curves are offset for clarity. The inset shows the comparison between the LL spacing measured in the absorption spectrum (in red) and the inverse of the beat period $T_{beat}$ seen in the LL0 FWM signal vs. $\Delta t$ (in black).

### 6.5.2 Intensity dependence

We have also measured $S_{SR}^{doped}(\Delta t, \omega)$ and $S_{SR}^{undoped}(\Delta t, \omega)$ as a function of the incident power, varying the photo–carrier density in the range $n/10 \rightarrow n$, where $n$ is the number of doped carriers in the MDQW (for sample C this is $2.1 \times 10^{11}$ carriers/cm$^2$, see Table 4.1), both when the laser preferentially excites LL1 (60:1 excitation ratio, as above), and when we excite both levels together.

When we excite only LL1 with the laser at low excitation power, we see the large "off–resonant" signal from LL0, which has a large negative time delay signal (nearly sym-

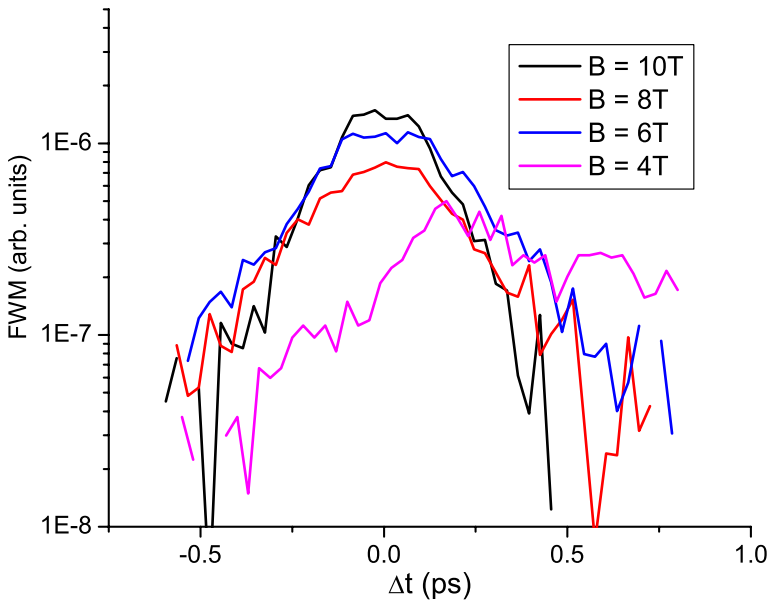


Figure 6.6: FWM emission from LL0 vs. time delay for sample C as a function of magnetic field, when the laser is tuned to excite only LL1 directly. For $B = 4$T ($\nu = 2.18$), there is no off–resonant signal from LL0, but for higher fields (once there is available space in LL0), we see the strong off–resonant signal with the nearly symmetric time delay dependence. Note: log scale.

metric as a function of $\Delta t$ ). The evolution of this signal as the excitation power is increased is shown in Fig. 6.7. The LL0 emission begins to develop weak beats as a function of $\Delta t$ , with a very pronounced minimum at $\Delta t = 0$ . The beats can also be seen more clearly in the black curve in Fig. 6.10(b). Notice that there is no real decrease in the signal for negative time delay.

When we tune the laser to excite both LL0 and LL1, the LL0 signal exhibits pronounced beats in $\Delta t$ at low power, but only for $\Delta t > 0$. As the power is increased, a large minimum at $\Delta t = 0$ which is absent at low power begins to emerge. Figure 6.8 shows a comparison of the LL0 FWM emission at low power (excitation density $\approx n/10$) and at high power ($\approx n$) for this laser position.

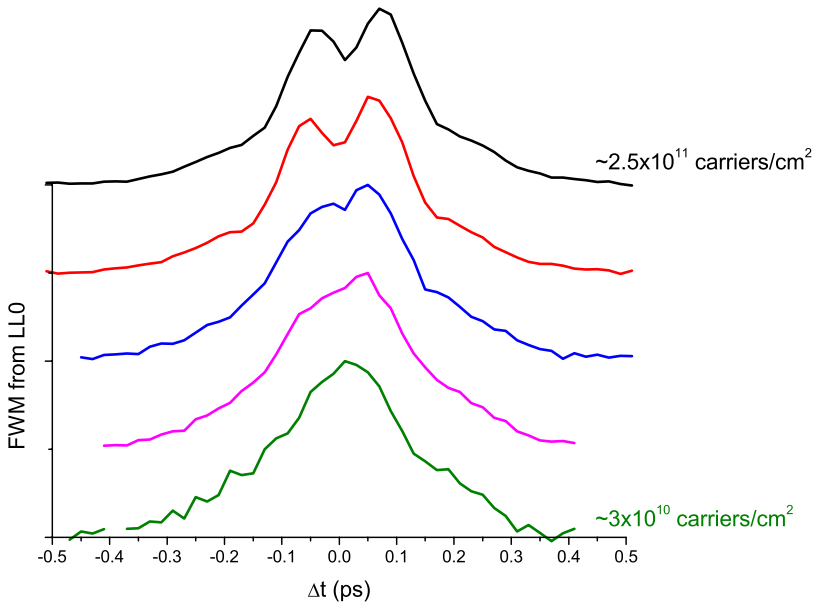


Figure 6.7: FWM emission from LL0 vs. time delay for sample C as a function of excitation density, at $B = 10$T, with only LL1 directly excited by the laser. The FWM curves are offset for clarity. As the excitation density is increased from $\approx n/10 \rightarrow n$, where $n$ is the number of doped carriers in the MDQW, we see the development of beats in the signal, with a pronounced minimum at $\Delta t = 0$ .

In addition to these beats, the unusual transfer of oscillator strength from LL1 to LL0 seen in sample C is affected by the increase in power. To see this we calculate the relative emission ratio $R$, introduced above, for both samples as a function of the exciting laser power. We find that increasing the overall excitation power causes $R^{doped}$ to decrease towards unity, for either laser excitation. This effect is more pronounced at lower fields. This can be understood since as the field is decreased, LL0 is closer to being completely full before excitation, so carriers can not be photo–excited or scatter into LL0 as efficiently. In fact, for the higher intensity measurements at $B = 6$T , we were attempting to excite more carriers into LL0 than there was available space in the level, so that for these measurements we cannot be sure what the excitation density ratio should be, and $R^{doped}$ is not a useful

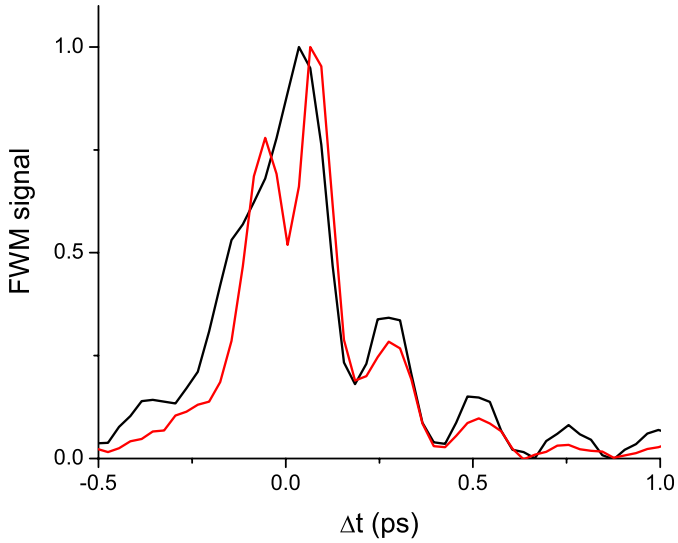


Figure 6.8: FWM emission from LL0 vs. time delay for sample C as a function of excitation density, at $B = 8$T, when both LL0 and LL1 are directly excited by the laser. The FWM curves are normalized for comparison. As the excitation density is increased from $\approx n/10 \rightarrow n$, we see the development of a pronounced minimum at $\Delta t = 0$ .

measure of the effects. The changes in $R^{doped}$ vs. excitation power for $B = 8, 10$T are shown by the black squares in Fig. 6.9. We have also measured the power dependence of $R^{undoped}$ from sample D, and found, surprisingly, the opposite effect, that high excitation density increases the relative size of the LL0 signal. This is also shown in Fig. 6.9. While the difference between the $R^{doped}$ and $R^{undoped}$ is still large (approximately a factor of 3) at our highest measured power (excitation density $\sim n$), it has decreased from the order of magnitude enhancement seen at low power.

These changes as a function of increasing excitation density are such that the doped and undoped samples begin to look more similar in their nonlinear optical response. This is illustrated in Fig. 6.10, which shows the signal from both samples C and D at both the low and high excitation powers. While the two samples look quite different at

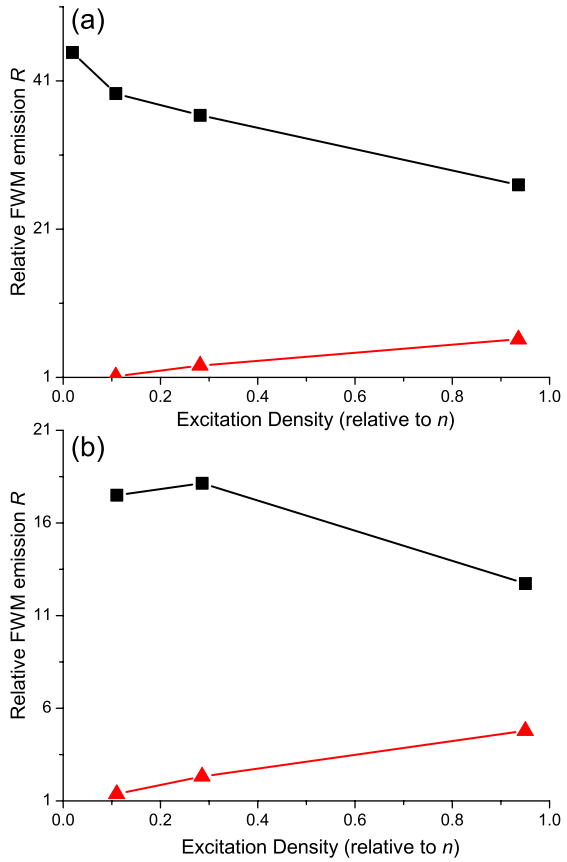


Figure 6.9: Relative FWM emission $R$ vs. excitation density for samples C and D, with only LL1 directly excited by the laser (60:1), (a) at $B = 10$T and (b) at $B = 8$T. The black squares are for sample C (the MDQW sample), and the red triangles are for sample D (the undoped QW). As the excitation density is increased from $\approx n/10 \rightarrow n$, we see a decrease in $R$ for sample C, and an increase for sample D

low density, the curves start to appear more similar at the higher density. This can be understood qualitatively, since as the density of photo–excited carriers approaches that of the electron gas, the mean–field exciton–exciton interactions (discussed in the semiconductor Bloch equations of Ch. 2.5.1) begin to dominate over the signal due to exciton–2DEG correlations. However, the $\Delta t = 0$ dip in LL0 for the doped case is always larger than any beat seen in undoped sample, and at least for the excitation densities we have measured,

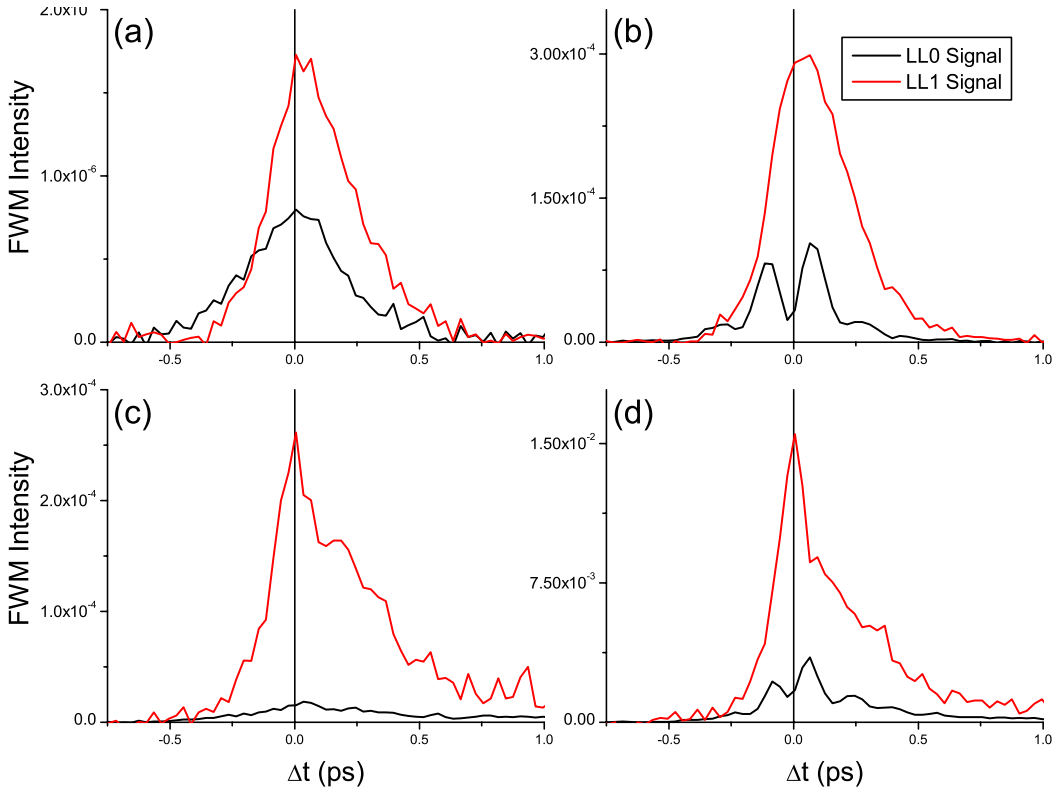


Figure 6.10: FWM vs. time delay for at B = 8T, from the LL0 and LL1 maxima. The black curves are the signals from LL0, and the red curves are from LL1. The laser is tuned to excite LL1 preferentially (60:1). The panels show the signals (a) from sample C at low density ($\approx n/10$), (b) from sample C at high density ($\approx n$), (c) from sample D at low density, and (d) from sample D at high density. There is a qualitative similarity between (b) and (d) at high density, despite the large differences in (a) and (c).

the negative time delay signal for the undoped QW sample is always less than the positive delay signal, while the negative time delay signal in the doped sample seems to remain as large as the positive time delay signal.

### 6.5.3 pulse duration dependence

By leaving the laser tuned directly to LL1, but varying the width of the exciting laser pulse in energy, we determined that the "off–resonant" signal from LL0 in that case

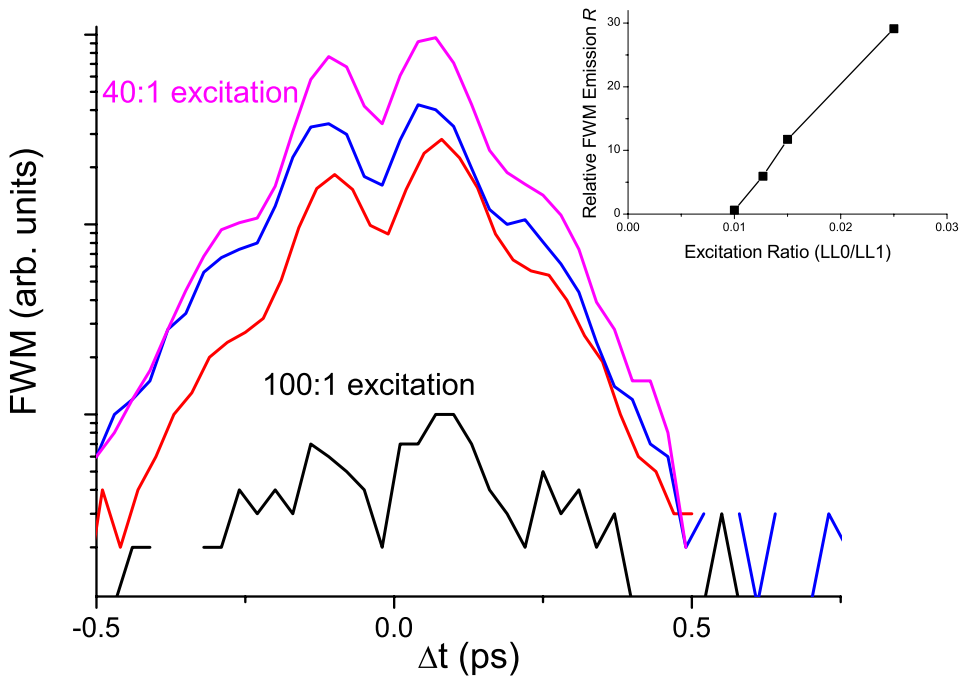


Figure 6.11: FWM emission from LL0 vs. time delay for sample C as a function of laser pulse width, when the laser is tuned to excite only LL1 directly. For an excitation of 100:1 into LL1, there is no signal from LL0, but for excitation of 50:1, we see a very strong signal from LL0. The inset shows the relative FWM emission $R$ as a function of the relative excitation of LL0. These measurements were performed at an intermediate excitation density, and therefore exhibit the beating described in the previous section. Note: log scale.

requires a small direct excitation of the level. When the pulse was narrowed so that only 1/100 of the carriers are excited into LL0 (rather than the 1/60 in the data discussed above), the LL0 signal dropped by nearly a factor of 30. This is shown in Fig. 6.11, which shows the LL0 signal from sample C for several different laser pulse widths, corresponding to excitations between 40:1 and 100:1 preferential excitation of LL1. As the figure makes clear, the strength of the off–resonant signal dropped off suddenly as we made the pulse narrower and excited less and less of the lowest level. We can conclude that while the 2DEG strongly enhances the signal from LL0 relative to LL1, this enhancement can only

be observed when there is a small direct excitation of LL0 as well.

## 6.6 Conclusion

In this chapter we described a series of FWM measurements, on both doped and undoped QW samples at high magnetic fields, in which the second lowest LL, LL1, was excited, either alone or along with LL0. While the undoped QW sample results were consistent with the mean–field theory of Ch. 2.5.1 or Ref. [112], there are a number of unusual features in the measurements on the MDQW sample. We observe a large transfer of signal strength from LL0 to LL1, and unusual features in the spectra as a function of the time delay. When LL1 and LL0 are excited equally, we see large beats in the signal from LL0 although there is no signal coming from LL1. When LL1 is excited preferentially, we see a large signal from LL0 for both positive and negative time delay, which is almost symmetric about $\Delta t = 0$ . These results require that LL0 is not completely full of doped electrons before excitation ($\nu < 2$), and that at least a small part of the laser pulse excites LL0. As the overall laser intensity is increased to excite more electron–hole pairs, beats with a pronounced minimum at $\Delta t = 0$ appear in the signal from LL0, and as the mean–field interactions between photo–excited carriers begin to dominate over the signal due to exciton–2DEG correlations, the doped and undoped signals begin to look more alike. As discussed above, we expect that these effects are due to correlations between the photo–excited carriers and the inter–LL excitations of the 2DEG, magnetoplasmons. In the next chapter we will describe in detail a theoretical formalism which includes the exciton–magnetoplasmon interactions, and which in the undoped case can be shown to include the DCTS theory of Ch. 2.5.2. We

will also present some model calculations based on this theory which qualitatively fit our experiments.

# Chapter 7

# Theory of FWM in doped Semiconductors

## 7.1 Introduction

In the previous chapter we described many unusual results seen in the FWM signal from a MDQW sample, which contains a strongly correlated 2DEG in the ground state. By comparing these effects with the signal from an undoped QW, we were able to determine that they are due to the correlations between the photo–excited carriers and the 2DEG excited states. We would like to develop a theoretical model which is capable of treating these exciton–2DEG interactions.

As discussed in Ch. 2.5, time dependent interactions and Coulomb correlations dominate the FWM response of semiconductors. These correlations result in non–Markovian dynamics which describe the propagation in time of long–lived collective excitation. To

describe these many–body effects in the FWM signal, we must truncate the infinite hierarchy of coupled equations for the correlation functions. For undoped semiconductors, we have seen in Ch. 2.5.2 that the dynamics controlled truncation scheme (DCTS) accomplishes this truncation through an expansion in terms of the optical fields [8]. However, as discussed there, the correspondence between the number of carriers in the system and the absorption of a photon breaks down if there are carriers doped into the system [9], as in our MDQW samples. Therefore, the DCTS cannot be applied to our system.

In this chapter we present an overview of a new theory based on the time dependent coherent state formalism of Refs. [82, 83, 85, 87, 88, 94, 108], which can be shown to include the DCTS theory, but which is also capable of describing a system with a strongly correlated ground state, such as our MDQW samples. A detailed derivation of the theory will be presented in the Appendices, and can also be found in Ref. [86]. Here we will simply discuss the new physics which must be accounted for, and which makes the use of the DCTS impossible, in our experiments. We will present a simplified "Average Polarization Model" (as in Ch. 2.5) based on the full theory, which we can compare qualitatively with the experimental results of the previous chapter.

## 7.2 Setup

We are interested in developing a comprehensive approach to the problem of the nonlinear optical response of a semiconductor QW containing a 2DEG in a large magnetic field. This system is described by the Hamiltonian [40] ($\hbar = 1$),

$$H_{\rm tot}(t) = H - \mu\mathcal{E}(t)\hat{X}^\dagger - \mu\mathcal{E}^*(t)\hat{X}. \tag{7.1}$$

Here, $H$ is the "bare" semiconductor Hamiltonian [40, 107, 23, 123],

$$H = \sum_{n,\mathbf{k}} \Omega_c^c (n+1/2) \hat{e}^\dagger_{\mathbf{k},n} \hat{e}_{\mathbf{k},n} + \sum_{n,\mathbf{k}} [E_g + \Omega_c^v (n+1/2)] \hat{h}^\dagger_{-\mathbf{k},n} \hat{h}_{-\mathbf{k},n} + V_{ee} + V_{hh} + V_{eh}, \quad (7.2)$$

$E_g$ is the bandgap, $V_{ee}, V_{eh}$, and $V_{hh}$ are the electron–electron , electron–hole, and hole–hole interactions respectively (among the photo–excited carriers *and* with the 2DEG as well), $\mathcal{E}(t)$ is the electric field of the applied laser pulse, and $\mu$ is the interband transition matrix element. The magnetic field splits the conduction and valence bands into electron ($e$) and hole ($h$) Landau Levels, $e$–LL$n$ and $h$–LL$n$. $\hat{e}^\dagger_{\mathbf{k},n}$ is the creation operator of the LL$n$ conduction band electron, $n = 0, 1, \cdots$, with cyclotron energy $\Omega_c^c$, and $\hat{h}^\dagger_{\mathbf{k},n}$ is the creation operator of the LL$n$ valence band hole, with cyclotron energy $\Omega_c^v$. Many novel properties of the 2DEG in a magnetic field originate from the fact that the carrier energies are independent of the momentum $\mathbf{k}$. The optical transition operator $\hat{X}^\dagger$ is given by

$$\hat{X}^\dagger = \sum_{n,\mathbf{k}} \hat{e}^\dagger_{\mathbf{k},n} \hat{h}^\dagger_{-\mathbf{k},n} = \sum_n \sqrt{N_n} \hat{X}^\dagger_n. \quad (7.3)$$

In the above equation we introduced the creation operator $\hat{X}^\dagger_n$ of the LL$n$ magnetoexciton state $|X_n\rangle = \hat{X}^\dagger_n |0\rangle$, where $|0\rangle$ is the ground state [107] and

$$\hat{X}^\dagger_n = \frac{1}{\sqrt{N_n}} \sum_{\mathbf{k}} \hat{e}^\dagger_{\mathbf{k},n} \hat{h}^\dagger_{-\mathbf{k},n}. \quad (7.4)$$

Here $N_n = N(1-\nu_n)$, and $N = L^2/2\pi l_c^2$ is the LL degeneracy, $l_c$ is the magnetic length, $L$ is the system size, and $\nu_n$ describes the filling of LL$n$. We will use the shorthand notation $X$ to designate a general magnetoexciton. The magnetic fields of interest for our experiments correspond to a partial filling of the lowest LL, i.e., the LL$n$ are empty ($\nu_n = 0$) for $n > 0$, while $0 < \nu_0 < 1$ (we neglect the spin in this discussion).

As in the theoretical approaches of Refs. [80, 79, 9, 7], we note the one to one correspondence between photon absorption/emission processes and $e$–$h$ pair creation/destruction. However, since there is a 2DEG present prior to excitation, when following the effects of the applied fields it is more convenient to count the number of valence band holes in a given state. We will use the shorthand notation 0–$h$, 1–$h$, 2–$h$ ... to label these states. As shown schematically in Fig. 7.1, states with three or more holes do not contribute to the third–order nonlinear polarization [73]. This cartoon demonstrates the time evolution of the semiconductor state $|\psi\rangle$ which results in coherent FWM emission. We can expand the state $|\psi\rangle$ in these terms,

$$|\psi\rangle = |\psi_0\rangle + |\psi_1\rangle + |\psi_2\rangle. \tag{7.5}$$

The intermediate 0–$h$, 1–$h$, and 2–$h$ states evolve in time according to the Schrödinger equation for the total Hamiltonian, Eq. (7.1), and they are coupled together by the absorption/emission of a photon ($|\psi_0\rangle$ is coupled to $|\psi_1\rangle$ by photon emission, $|\psi_1\rangle$ is coupled to $|\psi_0\rangle$ by photon absorption and to $|\psi_2\rangle$ by photon emission, and $|\psi_2\rangle$ is coupled to $|\psi_1\rangle$ by the absorption of a photon).

The $X$ states are not eigenstates of our semiconductor system Eq. (7.2), and during their time evolution they can interact with the 2DEG and create 2DEG excitations. As we mentioned in Ch. 6.4, for our experimental conditions, the dominant 2DEG excitations are the collective modes due to the coherent promotion of an electron from LL0 to a higher LL, or inter–LL magnetoplasmons (MP) [45, 65, 66]. Such MP eigenstates have the form [66]

$$|M_{\mathbf{q}}\rangle = \sum_{\mathbf{k}nn'} \rho_{nn'}(\mathbf{q}) \hat{e}^{\dagger}_{\mathbf{k}+\mathbf{q},n} \hat{e}_{\mathbf{k},n'} |0\rangle, \tag{7.6}$$

where $|0\rangle$ is the ground state and the amplitudes $\rho_{nn'}(\mathbf{q})$ are related to the LL$n'$ $\rightarrow$ LL$n$

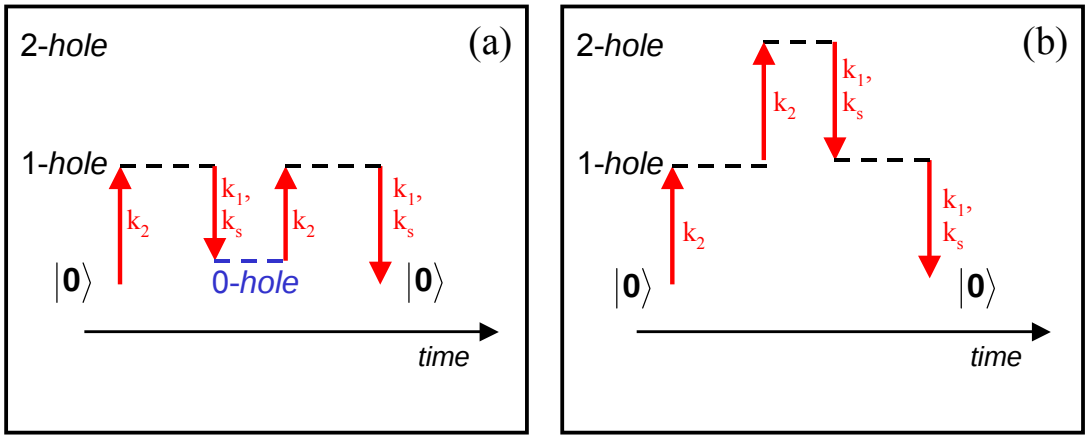


Figure 7.1: Cartoons of FWM processes in which the intermediate states are (a) 1–$h$ and 0–$h$ states, and (b) 1–$h$ and 2–$h$ states. In both cases, for a signal in the $2\vec{k}_2 - \vec{k}_1$ direction, the excitation is done by a $\vec{k}_2$ photon, and the de–excitation is done by either a $\vec{k}_1$ or a $\vec{k}_s$ photon (See Ch. 2.3). Since the FWM process is coherent, we must begin and end in the ground state, $|0\rangle$, but the intermediate 0–$h$ state in (a) need not be $|0\rangle$ for the doped sample.

contribution to the density operator [66]. For the magnetic fields of interest here, and for photo–excitation of only LL0 and LL1, the main contribution to the optical spectra comes from the LL0 $\rightarrow$ LL1 MPs (referred to from now on as the MP states), whose energy is close to the LL0 $\rightarrow$ LL1 energy and $\Omega_c^c$ [45, 65, 66]. The other MP excitations, and the incoherent particle–hole 2DEG excitations analogous to those in an ordinary Fermi liquid, have energies well above $\Omega_c^c$ and their contribution is therefore suppressed.

To help understand the differences between the MDQW system and an undoped semiconductor, we will discuss the qualitative structure of the Hilbert space of the system. From now on we will denote a general excited configuration of the electron gas by 2DEG*. The photo–excitations of the undoped system, or of the MDQW with the 2DEG at rest, consist of 1$e$–$h$, 2$e$–$h$, ...$\ell e$–$h$ pair states created in the different LLs. Similarly, the Hilbert

space of the 2DEG (with no photo–excited carriers) contains 1–MP, 2–MP,..,n–MP,... states. For the magnetic fields of interest in our experiments, the ground state $|0\rangle$ has all the $e$–LL$n$ and $h$–LL$n$ empty, except the e–LL0 which contains the 2DEG at rest. However, the total Hilbert space, $\mathcal{H}ilbert_{tot}$, contains many other 0–$h$ states which can be photo–excited via nonlinear optical processes assisted by inelastic Coulomb scattering. Also, QW states that cannot be optically excited in the absence of $X$–2DEG interactions (due to optical selection rules) do contribute to $\mathcal{H}ilbert_{tot}$, e.g. states with a MP and $e$ and $h$ not in LLs with the same indices. An example is the four–particle excitation {1–MP + 1–LL0–$e$ + 1–LL1–$h$}. As discussed below, such a state can result from the scattering of a LL1–$e$–$h$ pair with the 2DEG and plays an important role in the optical properties of the MDQW.

It is worth noting here that, because of the Coulomb interaction, the product of independent $e$–$h$ pair eigenstates and MP eigenstates is not an eigenstate of the total system, and moreover such product states do not form a complete basis set for our Hilbert space. To the first approximation, one can draw an analogy between the treatment of the $X$–MP effects of interest here and the transient $X$–phonon interaction effects studied in undoped semiconductors [118, 9, 7]. However, now we can see an important difference. In the undoped system, the electronic operators commute with the phonon operators, and one can separate out the electron–phonon interactions from the $X$-$X$ interaction effects. Also, the response of the ground state, which has an empty conduction band and a full valence band, to the photo–excited carriers can be neglected. One can therefore expand the state $|\psi\rangle$ in terms of a basis which consists of a product of the phonon wavefunctions times the $e$–$h$ pair wavefunctions [7, 107, 23]. In contrast to a phonon, a MP is made of electrons

(see Eq. (7.6)) and thus the MP operator does not commute with electronic operators, so we cannot simply separate out the different interaction processes as in the undoped system. Also, unlike for phonons, MPs do not strictly obey Bose statistics, so one must consider both $X$–MP and MP–MP Pauli blocking effects. Furthermore, the ground state 2DEG electrons are strongly correlated and can respond unadiabatically to the presence of the photo–excited carriers. Issues such as these make it impossible to use a set of simple basis states for describing the nonlinear optical response of the strongly correlated 2DEG system, which greatly complicates the calculation.

## 7.3 Time evolution of the photo–excited system

In this section we consider the time evolution of the photo–excited system, where we are particularly interested in the contributions to the semiconductor photo–excited state due to Coulomb interactions.

Let us examine in detail the 1–$h$ states. The evolution of the photo–excited $X$ state, $|X_n\rangle$, is determined by the action of the semiconductor Hamiltonian on that state. By subtracting out the contributions from all the $X$ states, the state $H|X_n\rangle$ can be written in the general form

$$H|X_n\rangle = \Omega_n|X_n\rangle - \sum_{n'\neq n} V_{n'n}|X_{n'}\rangle + |Y_n\rangle, \tag{7.7}$$

where

$$\Omega_n = \langle X_n|H|X_n\rangle \tag{7.8}$$

is the LL$n$ exciton energy,

$$V_{n'n} = -\langle X_{n'}|H|X_n\rangle = V^*_{nn'} \tag{7.9}$$

describes the Coulomb–induced coupling of the different LL excitons [112] (see Eq. (2.11)), and $|Y_n\rangle = \hat{Y}_n^\dagger|0\rangle$, where the operator

$$\hat{Y}_n = [\hat{X}_n, H] - \Omega_n \hat{X}_n + \sum_{n' \neq n} V_{nn'} \hat{X}_{n'}, \tag{7.10}$$

describes the interactions between the LL$n$ exciton and the rest of the carriers present in the system. Without the last term, $|Y_n\rangle$, Eq. (7.7) is equivalent to the theory of Ref. [112] used to model the undoped QW system (see Ch. 2.2.2 and Ch. 2.5.1). One can see by using the above three equations that $|Y_n\rangle$ is orthogonal to all the magnetoexciton states $|X_m\rangle$, $\langle Y_n|X_m\rangle = 0$, $n, m = 0, 1, \cdots$, and thus corresponds to a 2DEG* state, a state with an excited electron gas configuration.

The states $|Y_n\rangle$ describe new $\{1e\text{–}h\text{+}1\text{MP}\}$ four–particle excitations which deserve some explanation. Let us illustrate their meaning and origin by an example that is important in comparison with our experiments: the case where only LL0 and LL1 are significantly excited. Let us consider the LL1 exciton. The LL1 electron can scatter down to LL0 by emitting a MP. Since the MP energy is close to the $e$–LL0 $\rightarrow$ $e$–LL1 energy spacing, the above interaction process is nearly resonant. It therefore provides an efficient decay channel of the LL1 exciton to a {1–MP + 1–LL0–e + 1–LL1–h} four–particle excitation, which we will call a $Y$ excitation. This is shown schematically in Fig. 7.2. In the case of a LL0 exciton, the hole can scatter while emitting a MP. However, such an interaction process, which also results in a {1–MP + 1–LL0–e + 1–LL1–h} four–particle excitation, is non–resonant. Therefore, the decay of the LL0 $X$ is suppressed as compared to that of the LL1 $X$.

The scattering described above is a new interaction process between the photo–

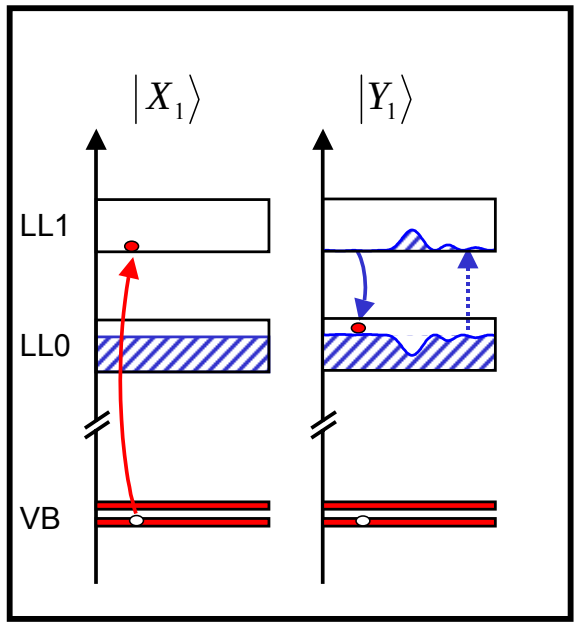


Figure 7.2: Cartoons of the states $|X_1\rangle$ and $|Y_1\rangle$. On the left, we excite the state $|X_1\rangle$ with a photon. On the right, we show the creation of a $|Y_1\rangle$ excitation, in which the LL1 $e$ scatters into LL0 while creating a MP excitation. This state is nearly resonant with the $|X_1\rangle$ state, $\bar{\Omega}_1 \sim \Omega_0 + \Omega_M \sim \Omega_1$, and therefore this interaction process can be greatly enhanced.

excited $X$ states and the 2DEG, which provides additional dephasing of our system. As we will see below, this dephasing is also non–Markovian, i.e. the processes are not instantaneous, producing a memory kernel in the time domain, or an there is an energy dependence to the dephasing rate in the frequency domain (recall the discussion in Ch. 2.3.3). Note that $W_{nn'} = \langle Y_n | Y_{n'} \rangle = \langle X_n | H | Y_n' \rangle$ describes the probability amplitude for such an $X \leftrightarrow Y$ scattering event, and is nonzero even if $n \neq n'$. By accounting for this scattering in our theory, we already present a qualitative difference between the MDQW system and an undoped QW system. In the case of undoped semiconductors studied in Refs. [9, 7], the operator $\hat{Y}_n$ in Eq. (7.10) can be decomposed into two parts: one is independent of the phonon variables and describes $X$-$X$ Coulomb interactions, while the other describes the phonon

creation/annihilation processes due to the electron–phonon interaction. Such a distinction is possible due to the fact that phonons are bosons that commute with all electronic variables. This decomposition can then be used to separate out the $X$-$X$ Coulomb interaction from the electron–phonon scattering contributions to the dephasing of the $X$ state. In fact, the former contribution corresponds to the correlation function $\bar{Z}$ of Refs. [9, 7], which mainly contributes to the six–wave mixing spectra [17, 6]. However, unlike for phonons, the MP excitations of the 2DEG are made of electrons, like the $X$. As a result, it is no longer possible to separate the MP creation/annihilation contribution to $\hat{Y}_n$ from the $X$-$X$ interaction processes.

We can perform a similar analysis on 2–$h$ states, which should be similar to the undoped system [107, 80, 79]. Starting from the photo–excited 2–$X$ state $|X_n X_m\rangle$, we allow the $X$ to interact with each other as well as with the 2DEG, as described by the equation

$$H|X_n X_m\rangle = (\Omega_n + \Omega_m)|X_n X_m\rangle - \sum_{m' \neq m} V_{m'm}|X_n X_{m'}\rangle - \sum_{n' \neq n} V_{n'n}|X_{n'} X_m\rangle + |X_n Y_m\rangle + |X_m Y_n\rangle + |B_{nm}\rangle, \qquad (7.11)$$

obtained by using Eq. (7.10) to calculate the state $[H, \hat{X}_n^\dagger \hat{X}_m^\dagger]|0\rangle$. The first term in Eq. (7.11) is the energy of the two non–interacting $X$, while the following two terms come from the Coulomb–induced LL coupling of Ref. [112]. The second line is easy to interpret. Similar to $|X_n X_m\rangle$, the states $|X_n Y_m\rangle = \hat{X}_n^\dagger \hat{Y}_m^\dagger |0\rangle$ describe an $X_n$ and a $Y_m$ excitation that do not interact with each other. Finally, the last term in Eq. (7.11),

$$|B_{nm}\rangle = [\hat{Y}_n^\dagger, \hat{X}_m^\dagger]|0\rangle = [[H, \hat{X}_n^\dagger], \hat{X}_m^\dagger]|0\rangle, \qquad (7.12)$$

comes from $X$-$X$ interactions [48, 49, 47, 80, 30, 17, 6, 107]. This interacting two–exciton state is a linear combination of two $e$–$h$ pairs with different center of mass momenta, with

the 2DEG in its ground state. It is therefore orthogonal to all the 2DEG* states, such as $|X_n Y_m\rangle$, and describes the biexciton bound, $X_2$, and scattering, $XX$, states. It is this state which is responsible for the large non–Markovian FWM signal which comes from $X$-$X$ interactions beyond the mean–field, random phase approximation (RPA), seen for example in bulk GaAs in a high magnetic field [48, 49, 30], or in ZnSe QW samples [17]. In Ref. [107] it was found that the $X$-$X$ correlations described by this state lead to a new time dependence as compared to the RPA theory only when the dephasing of the $X$-$X$ interacting states is sufficiently weak, or when bound biexcitons are present. We do not expect these conditions to occur in the case of our MDQW samples. Thus, for simplicity in our model we will treat the $X$-$X$ interactions at the RPA level, and neglect higher correlations.

Finally, we turn to the 0–$h$ state, which has a contribution proportional to the ground state $|0\rangle$, and also a $\{0\text{–}h/2\text{DEG}^*\}$ contribution, which is second order in the applied laser field. This second part includes the time evolution of the MP state excited via a second–order process analogous to the one that leads to the inelastic Raman scattering signal [92]. We now introduce the state

$$|M_{nm}\rangle = \hat{X}_n |Y_m\rangle. \tag{7.13}$$

Recalling that $|Y_m\rangle$ is an $X$–MP excitation and $\hat{X}_n$ annihilates an $X$, we see that the state $|M_{nm}\rangle$ is a MP state. The creation of such a MP state is described schematically in Fig. 7.3. This process contributes to both the nonlinear response and to the inelastic Raman scattering spectra, but is only observable due to the $e$–$h$ asymmetry in all real systems [92, 20], and the relaxation of the momentum conservation and MP decay induced by impurities and disorder (see for example [70]). We note again that without deviations

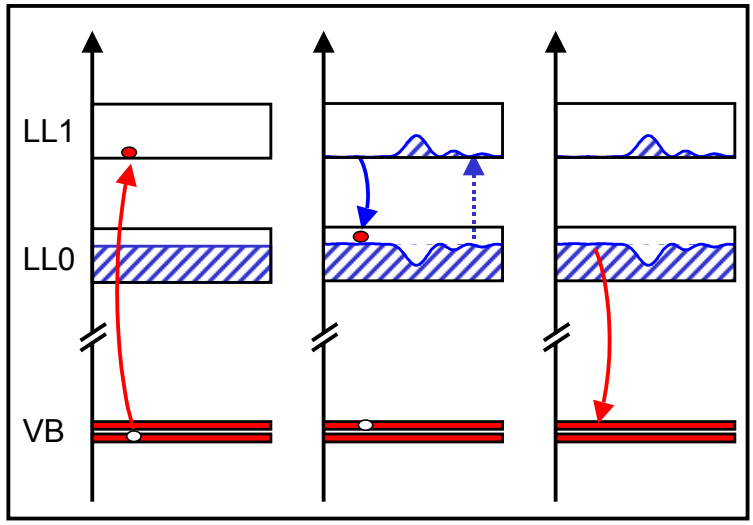


Figure 7.3: The creation of a magnetoplasmon excitation. In the first panel, we excite the state $|X_1\rangle$. In the second panel, the LL1 $e$ scatters to LL0 while emitting a MP. In the final panel, the $e$–$h$ pair recombines, leaving only a MP excitation. This process is equivalent to a Stokes Raman scattering process, and it can be reversed to describe MP destruction.

from the ideal case of $e$–$h$ symmetry, as discussed in Ch. 2.2.2, these contributions would be absent from the optical response.

## 7.4 Nonlinear polarization and average polarization model

Within the dipole approximation, the optical response is determined by the polarization of the photo–excited system,

$$P(t) = \mu\langle\psi|\hat{X}|\psi\rangle = \mu\sum_n \sqrt{N_n}P_n(t), \tag{7.14}$$

where $|\psi\rangle$ is the time dependent semiconductor wavefunction that evolves from the ground state $|0\rangle$ according to the Schrödinger equation for the total Hamiltonian, Eq. (7.1). In the last term of Eq. (7.14) we have expressed $P(t)$ in terms of the average values $P_n(t)$ of the

magnetoexciton operators,

$$P_n(t) = \langle\psi|\hat{X}_n|\psi\rangle. \tag{7.15}$$

Using the standard techniques of nonlinear optics, we will expand the polarization in powers of the electric field (up to third order), $P(t) = P^{(1)}(t) + P^{(3)}(t)$. We can then solve perturbatively, first for the linear polarization, then for the third order FWM polarization. From here, we will call the linear polarization $P_n^L(t) \equiv P_n^{(1)}(t)$, and the nonlinear polarization $P_n(t) \equiv P_n^{(3)}(t)$. To solve for $P_n^L(t)$ and $P_n(t)$, we must understand the time evolution of the state $|\psi\rangle$, which contains 0–$h$, 1–$h$ and 2–$h$ contributions to third order in the applied field.

Following the formalism of Refs. [82, 83, 85, 87, 88, 94, 108], we describe the evolution of the state $|\psi\rangle$ in terms of its non–interacting and correlated contributions. Starting with the states $|X_n\rangle$, $|Y_n\rangle$, $|B_{nm}\rangle$, and $|M_{nm}\rangle$, we can define additional basis states, using the recursive, or Lanczos, method [42, 76], to describe the dephasing and correlations between the photo–excited states. Similar to Eq. (7.7) that introduced the states $|Y_n\rangle$, we use the Lanczos method to obtain a new basis state by acting with the Hamiltonian $H$ on the previous state, and then orthogonalizing the result with respect to the existing basis states [42]. By choosing a suitable place to truncate the series of basis states created in this method, we can generate a closed set of equations to describe the FWM signal in our MDQW system. The full derivation of the nonlinear polarization $P_n(t)$ using this method is given in Appendix A.

In order to connect with our experimental results, it is useful at this point, as in Chs. 2.5.1 and 2.5.2, to introduce an average polarization model (APM), which will quali-

tatively account for the physics of our MDQW system, while simplifying the equations to make the interpretation transparent. To begin, we note that an ideal 2DEG under a strong magnetic field displays electron–hole symmetry since the electron and hole wavefunctions become identical (see Ch. 2.2.2 for a discussion about the causes of electron–hole asymmetry in real QW systems). We will start from the symmetric limit, which is analyzed in Appendix B, and only add the asymmetry effects that lead to new dynamics absent in the ideal system. We will also truncate our basis set at $|Y\rangle$, and introduce a phenomenological dephasing rate for the $Y$ excitations. Finally, we will consider only the two LLs excited in the experiments, LL0 and LL1, which will leave us with only a small set of coupled equations, depending on only a few parameters and simple enough to be integrated numerically on a PC. This will allow us to describe the dynamics due to the main physical processes in a straightforward way. We note that the qualitative features of the dynamics are robust and do not depend sensitively on our assumptions about the different interaction parameters.

In Appendix B we show that in the electron–hole symmetric limit

$$\hat{Y}_1 = -\hat{Y}_0 = \hat{Y}. \tag{7.16}$$

This symmetry relation implies that $|Y_0\rangle$ and $|Y_1\rangle$ describe the same state $|Y\rangle$, with a single energy $\bar{\Omega}$. In Appendix C we use this symmetry relation to derive a number of simplifications for our model. For example, we find that there is only one MP state $|M\rangle$ needed to describe the MP correlation effects, with a single effective MP energy $\Omega_M$.

Taking all of these approximations together, and neglecting some additional source terms that do not add new information about the system and are comparatively small, we can write a closed set of equations which must be solved to simulate our FWM experiment.

The coupled first order polarization equations are:

$$i\frac{\partial}{\partial t}P_0^L(t) = (\Omega_0 - i\Gamma_0)P_0^L(t) - V_{01}P_1^L(t) - \bar{P}^L(t) - \mu\mathcal{E}(t)\sqrt{N_0} \tag{7.17}$$

$$i\frac{\partial}{\partial t}P_1^L(t) = (\Omega_1 - i\Gamma_1)P_1^L(t) - V_{10}P_0^L(t) + \bar{P}^L(t) - \mu\mathcal{E}(t)\sqrt{N_1} \tag{7.18}$$

$$i\frac{\partial}{\partial t}\bar{P}^L(t) = (\bar{\Omega} - i\gamma)\bar{P}^L(t) + W\left(P_1^L(t) - P_0^L(t)\right). \tag{7.19}$$

These equations describe the first order response of the sample to the electric field pulse of the laser, $\mathcal{E}(t)$. The linear polarization $P_n^L(t)$ oscillates in time like a harmonic oscillator, with frequency $\Omega_n$, damped by a phonon induced dephasing rate $\Gamma_n$, and driven by the electric field of the exciting laser. These are the first and last terms, respectively, in Eqs. (7.17) and (7.18). The parameter $V_{01} = V_{10}^*$ describes the LL coupling of Ref. [112], explained in the undoped case in Chs. 2.2.2 and 2.5.1. We expect that the screening caused by the doped electrons in the 2DEG should lower the value of this coupling parameter for the MDQW case. The function $\bar{P}^L(t)$ describes the dephasing of the linear polarization $P^L(t)$ through the $X \leftrightarrow Y$ scattering process described in the previous section. It also behaves like a driven harmonic oscillator, but evolves in time according to its own energy $\bar{\Omega} \sim \Omega_0 + \Omega_M \sim \Omega_1$, and a dephasing rate $\gamma$ which accounts approximately for all of the states into which $|Y\rangle$ can scatter. The coupling parameter $W = \langle Y|Y\rangle = \langle X|H|Y\rangle$ gives the probability amplitude of the $X \leftrightarrow Y$ scattering process which drives $\bar{P}^L(t)$.

It is important to note that the dephasing of the optical polarization obtained within this model is non–Markovian. This can be clearly seen at the linear polarization level. We can solve Eqs. (7.17)-(7.19) analytically by Fourier transform:

$$\left[\omega - \Omega_n(\omega)\right] P_n^L(\omega) + V_{nn'}(\omega)P_{n'}^L(\omega) = -\mu\mathcal{E}(\omega)N_n^{1/2}, \tag{7.20}$$

where $n, n' = 0, 1$ and $n \neq n'$. The exciton energy $\Omega_n(\omega)$ and the LL coupling $V_{nn'}(\omega)$ now include frequency–dependent self–energy corrections due to the $X$–2DEG scattering,

$$\Omega_n(\omega) = \Omega_n + \frac{W}{\omega - \bar{\Omega} + i\gamma} - i\Gamma_n, \tag{7.21}$$

and

$$V_{nn'}(\omega) = V_{nn'} + \frac{W}{\omega - \bar{\Omega} + i\gamma}. \tag{7.22}$$

The frequency–dependence of the above magnetoexciton energies and coupling constants is a manifestation of the non–Markovian behavior of the system. This arises because part of the optical excitation is temporarily stored in the shake–up excitations described by $\bar{P}^L(t)$. This effect is exacerbated when we consider higher orders in the applied field.

The polarization $P^L(\omega) = P_0^L(\omega) + P_1^L(\omega)$ can be fit to the linear absorption data for our sample, in order to fix the parameters $V_{01}$, $W$, $\Gamma_n$, and $\gamma$.

At second order in the electric field, we must consider the influence of 2–$h$ and correlated 0–$h$ states. We approximate the $X$-$X$ interactions at the mean–field RPA level, in which we factorize the biexciton correlation function (see Ch. 2.5.1). Within the electron–hole symmetric limit of Eq. (7.16), there is only one second order equation necessary for our model, the equation for the magnetoplasmon correlation function $\mathcal{M}(t)$,

$$i\frac{\partial}{\partial t}\mathcal{M}(t) = (\Omega_M - i\gamma_M)\mathcal{M}(t) + W_M P_0^{L*}(t)\left[P_1^L(t) - P_0^L(t)\right]. \tag{7.23}$$

This correlation function describes the time evolution of the MP state, and the scattering during the two photon process that excites the 2DEG. The driving term of Eq. (7.23) is similar to a coherent density, $\propto |P^L|^2$, and describes the creation of a MP excitation from the photo–excited $X$ states as presented above in Fig. 7.3. The time dependence of $\mathcal{M}(t)$,

which is found from the integration of this equation, will lead to additional non–Markovian effects in the dynamics of the nonlinear polarization. Recall that the MP induced FWM signal, like the MP–Raman scattering signal, requires a deviation from the ideal symmetric limit (see Section 7.3). The parameter $W_M = \langle M|M\rangle$, which gives the strength of the MP correlation contribution to the FWM signal, is also a measure of the electron–hole asymmetry in the system.

Finally we can write the equations of motion for the third–order nonlinear polarization which gives the FWM signal:

$$\begin{aligned} i\frac{\partial}{\partial t}P_0(t) &= (\Omega_0 - i\Gamma_0)P_0(t) - V_{01}P_1(t) - \bar{P}(t) \\ &+\frac{2\mu\mathcal{E}(t)}{\sqrt{N_0}}P_0^L(t)P_0^{L*}(t) + V^{XX}\left(P_1^{L*}(t) - P_0^{L*}(t)\right)P_1^L(t)P_0^L(t) \\ &-\frac{1}{N_0}P_0^L(t)P_0^L(t)\bar{P}^{L*}(t) + \mathcal{M}^*(t)\left(P_1^L(t) - P_0^L(t)\right), \end{aligned} \tag{7.24}$$

describes the LL0 nonlinear polarization $P_0(t)$. Let us discuss the meaning of the source terms in this equation before presenting the other third–order equations.

The first line of Eq. (7.24) contains, as in the linear case of Eq. (7.17), the energy and damping for the oscillation of the LL0 polarization, as well as the coupling between the LLs, $V_{01}P_1(t)$, and the $\bar{P}(t)$ term which describes the additional dephasing from the $X \leftrightarrow Y$ scattering. This dephasing is enhanced in the nonlinear regime, due to the time dependence of the photo–excitations, as we will discuss below.

The second line of Eq. (7.24) gives the driving terms for $P_0(t)$ which are similar to the undoped RPA level model of Ch. 2.5.1. The first term is the familiar Pauli blocking nonlinearity (PB), which exists even in atomic systems (see Ch. 2.4), and comes from the fact that the excitations obey the Pauli exclusion principle. It is proportional to the coherent

density $|P_n^L(t)|^2$, and can be thought of as the scattering of a laser photon with the coherent density of photo–excited carriers. The second term is the nonlinearity due to the RPA $X$-$X$ interactions. Similar to the Pauli blocking term above, we can describe this term as the scattering of the photo–excited polarization with the coherent density of photo–excited carriers. The parameter $V^{XX}$, which describes the strength of the $X$-$X$ nonlinearity, is shown in Appendix C to have a simple relationship with $V_{01}$. As in Ch. 2.5, we refer to this nonlinearity as the bare Coulomb interaction (BCI). While these effects are found in the RPA model of FWM in undoped semiconductors, the additional dephasing and screening from the 2DEG will lead to a qualitative difference in th FWM spectrum.

The third line of Eq. (7.24) describes effects which are entirely absent in the undoped case, and come from the 2DEG excitations. The first term, which we call the Shake–up term, describes the shake–up of the 2DEG during the exciton recombination that leads to the coherent emission. In particular, the situation where the photo–excitation of two $X$ is followed by the recombination of one them assisted by the shake–up of a MP excitation. The above process leaves the system in the $\{1\text{–}h/2\text{DEG}^*\}$ state $|Y_m\rangle$, which is then annihilated by the optical field. The last term in Eq. (7.24), which describes the MP correlations (MPC), comes from photo–excitation and time evolution of the MP state, described by $\mathcal{M}(t)$. This source term describes processes such as the following, shown schematically in Fig. 7.4. A photo–excited $X$ decays into a $Y$, or $\{X\text{–MP}\}$ excitation. The $e$–$h$ pair in this state recombines leading to the coherent emission, which leaves the system in the MP state $|M\rangle$. This MP propagates in time and then interacts with the second photo–excited $X$ into a new $X$ state, which is subsequently annihilated by the optical field. It is

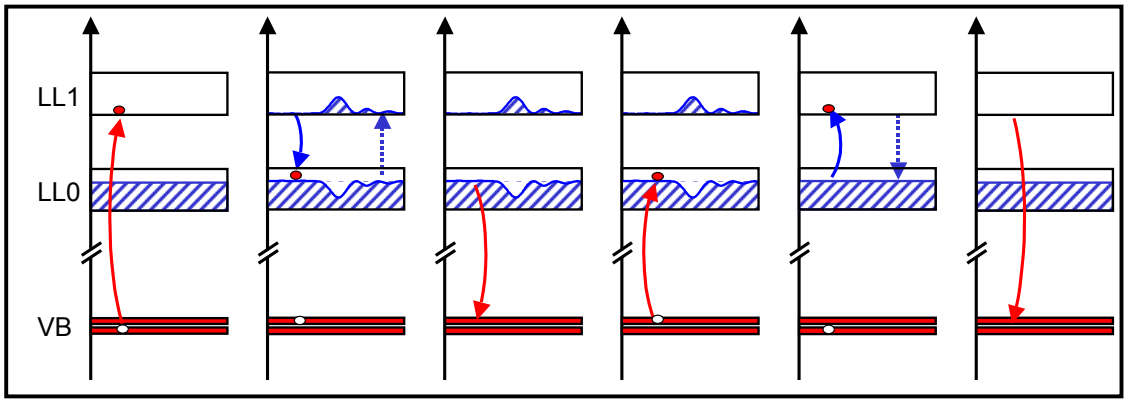


Figure 7.4: Magnetoplasmon correlation (MPC) contribution to the FWM signal. The first three panels describe the Stokes Raman scattering process for the creation of a MP excitation, as in Fig. 7.3. The reverse, antiStokes Raman process which returns the system to the ground state, is shown in the final three panels. Not the similarity of this process to coherent antiStokes Raman scattering with phonons.

interesting to note the similarity of this process to the familiar one of coherent antiStokes Raman scattering [58] that, however, involves phonons. This process will contribute the the FWM signal with a new time dependence which comes from the equation of motion for $\mathcal{M}(t)$.

The equation of motion for $P_1(t)$ contains similar source terms,

$$\begin{aligned} i\frac{\partial}{\partial t}P_1(t) &= (\Omega_1 - i\Gamma_1)P_1(t) - V_{10}P_0(t) + \bar{P}(t) \\ &+\frac{2\mu\mathcal{E}(t)}{\sqrt{N_1}}P_1^L(t)P_1^{L*}(t) - V^{XX}\left(P_1^{L*}(t) - P_0^{L*}(t)\right)P_1^L(t)P_0^L(t) \\ &-\frac{1}{N_1}\left(P_1^L(t)P_1^L(t)\bar{P}^{L*}(t) + 2P_1^L(t)P_0^L(t)\bar{P}^{L*}(t)\right), \end{aligned} \tag{7.25}$$

and is of course coupled to $P_0(t)$ by the LL coupling $V_{01}$. Note that the MPC terms only contribute in the $P_0(t)$ equation, due to the symmetry relation Eq. (7.16) and its consequences, as described in Appendix B.

Both $P_0(t)$ and $P_1(t)$ are coupled to $\bar{P}(t)$, which describes the dephasing of the

nonlinear polarization due to the $X \leftrightarrow Y$ scattering, as discussed above for the linear polarization. This serves to reinforce the dephasing induced by this scattering, as well as introduce time dependent corrections to the coupling. The full equation of motion for $\bar{P}(t)$ contains many driving terms which come from the interactions among the 2DEG* excited states. However, all of these terms, proportional to $\bar{P}^L(t)$, are damped by an additional dephasing width $\gamma$, and thus lead to a broad incoherent contribution to the FWM spectrum. We will neglect all of these terms, and keep only the source terms which are not as strongly damped. The equation of motion for $\bar{P}(t)$ is

$$i\frac{\partial}{\partial t}\bar{P}(t) = (\bar{\Omega} - i\gamma)\bar{P}(t) + W(P_1(t) - P_0(t))$$
$$+W\left(\frac{2}{N_1}P_1^L(t)P_0^L(t)P_1^{L*}(t) - \frac{1}{N_1}P_1^L(t)P_1^L(t)P_1^{L*}(t) - \frac{1}{N_0}P_0^L(t)P_0^L(t)P_0^{L*}(t)\right). \quad (7.26)$$

The first line of this equation gives the energy and dephasing of $\bar{P}(t)$, and the coupling to the nonlinear polarizations $P_n(t)$, as in the linear case. Since $\bar{P}(t)$ describes the dephasing of the polarization, the source terms of Eq. (7.26) describe the excitation–induced dephasing, or the time dependent changes to the dephasing due to the excitation of additional carriers. The second line can be thought of as describing, to lowest order in the optical field, the excitation–induced correction to the scattering amplitude $W$ that is proportional to the coherent density. This effectively gives a time dependence to the coupling parameter $W$ coming from the presence of the photo–excited carriers. Keeping additional source terms in Eq. (7.26) will add a broad incoherent background signal, and as long as we treat the dephasing of the $Y$ states by a phenomenological parameter $\gamma$ there is no reason to include them.

In the next section we present the numerical solutions to these equations, resulting

in the FWM signal. We analyze the effects of the individual terms in Eqs. (7.24) - (7.26), and show that this average polarization model is able to qualitatively explain our experiments for the correct choice of parameters.

## 7.5 Simulations

Here we will solve the model equations presented in the last section, and compare the results to the experimental data from the previous chapter.

We start by assuming a laser excitation of the form $\mathcal{E}(t) = e^{i\vec{k}_2\cdot\vec{r}}\mathcal{E}_p(t) + e^{i\vec{k}_1\cdot\vec{r}}\mathcal{E}_p(t+\Delta t)$, where $\mathcal{E}_p(t)$ is the Gaussian envelope of the pulses emitted by the laser. We then solve the equations above as a function of time $t$ and time delay $\Delta t$, keeping only the terms leading to a nonlinear signal in the $2\vec{k}_2 - \vec{k}_1$ direction. We perform a Fourier transform of the nonlinear polarization to get $P(\Delta t, \omega)$. The FWM signal measured in our experiments is then $S_{SR}(\Delta t, \omega) \propto |P(\Delta t, \omega)|^2$.

As mentioned in the previous section, by fitting the calculated linear polarization spectrum to the linear absorption measurements taken to characterize our sample, we can fix the parameters $V_{01}$, $W$, and the dephasing parameters $\Gamma_n$ and $\gamma$, to within $\pm 50\%$. This is shown in Fig. 7.5, which compares the calculated absorption $\alpha(\omega) \propto Im\{\chi^{(1)}(\omega)\} = Im\{P^L(\omega)/\mathcal{E}(\omega)\}$ with our measured absorption spectra for sample C at $B = 8$T. The fit is quite good overall, giving the correct ratio of peak heights and widths. Recall that the valence band structure of the sample leads to additional peaks in the spectrum, which we do not include in our model. This gives the small peak just above the LL0 energy, and the shoulder on the high energy side of the LL1 peak in the absorption spectrum from sample

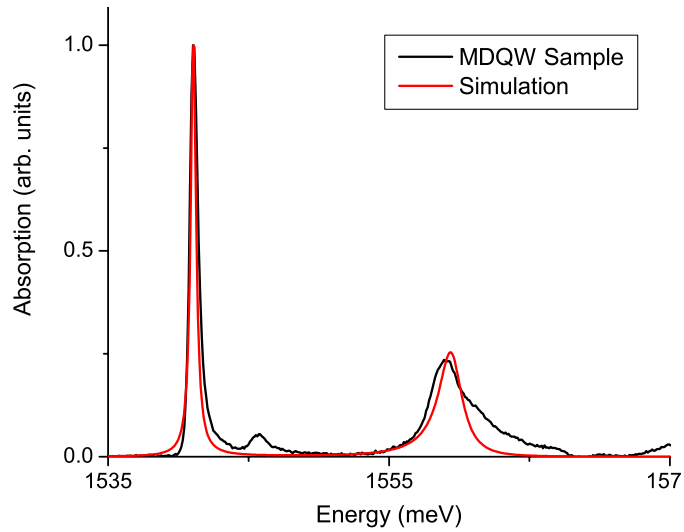


Figure 7.5: Simulation of the linear absorption spectrum. We fit the linear polarization calculated from the model (red curve) to the sample C absorption spectrum (black curve). This fit is for $V_{01} = 0.3$ meV, $W = 4.5$ meV$^2$, and $\gamma = 6.2$ meV. The fit is quite good in terms of the ratio of oscillator strength and peak width.

C. Varying the parameters within the fitting range ($\pm 50\%$) yields is no significant change to the calculated FWM signal. Essentially, this leaves us with two free parameters in the calculation of the nonlinear polarization, the strength of the MPC term, $W_M$, and the MP energy $\Omega_M$.

The simulated FWM signal with the optimal choice of parameters, $S_{SR}^{model}(\Delta t, \omega)$ is presented in Fig. 7.6, along with the experimental results $S_{SR}^{doped}(\Delta t, \omega)$, for the case where we excite the two LLs equally. As the figure clearly shows, the simulations are able to recreate both the transfer of signal strength to LL0 and the pronounced beats coming from only the single level. The beat period in the simulation is given by the inverse of the LL energy difference, as in the experiment.

When we move the laser to excite only into LL1, we can also recreate the transfer

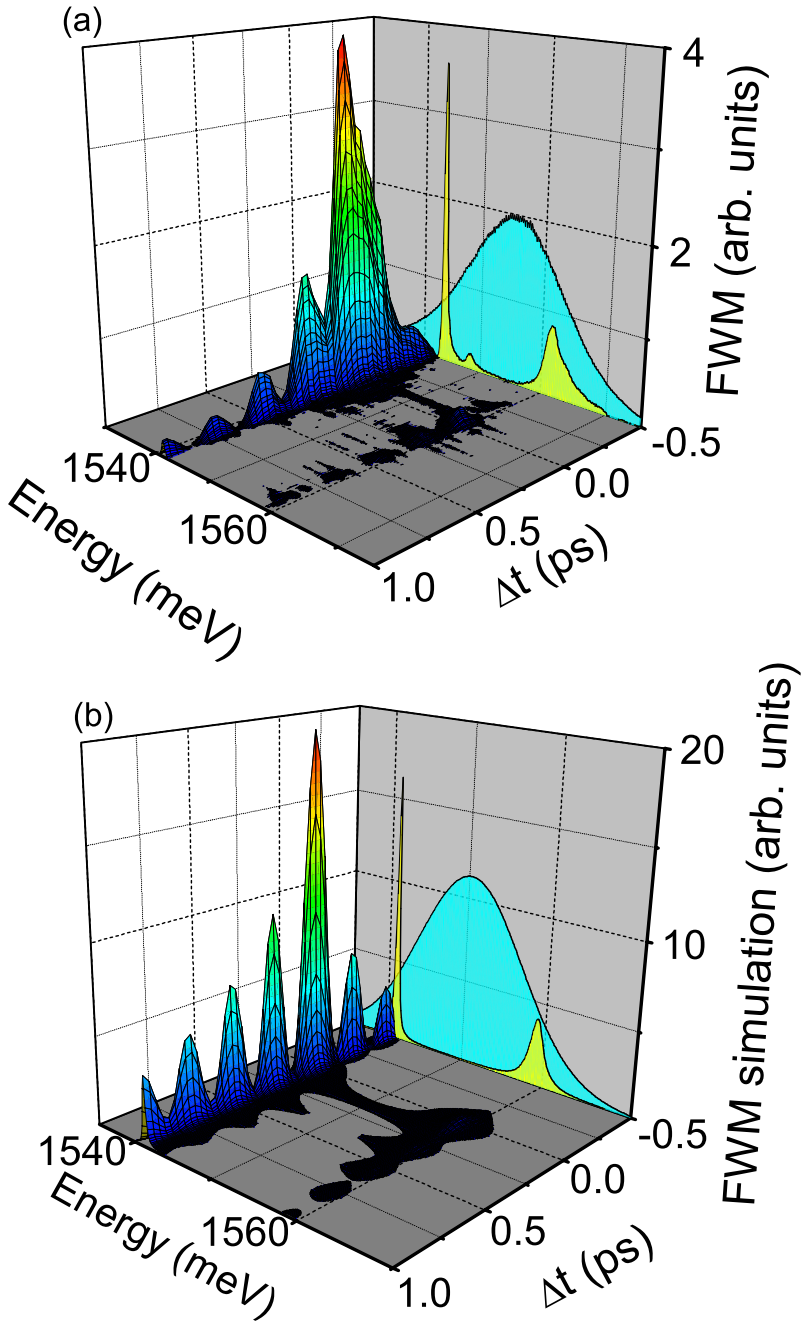


Figure 7.6: Simulation of the FWM signal for excitation of both LLs equally. (a) The signal from sample C for $B = 8$T, when we excite an equal number of $e$–$h$ pairs into both LL0 and LL1 (same as Fig. 6.1(a)). (b) The simulated signal $S_{SR}^{model}(\Delta t, \omega)$ for the same conditions as (a). The laser pulse and absorption spectra are projected on the back screen.

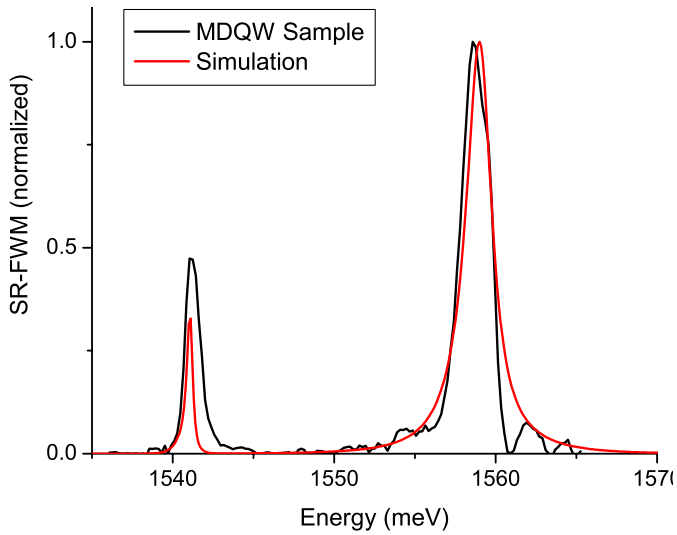


Figure 7.7: Simulation of the FWM signal at $\Delta t = 0$ for the preferential excitation of LL1. The black line shows the signal from sample C for $B = 8$T, at $\Delta t = 0$ , when we excite LL1 preferentially (60:1 excitation of LL1:LL0, same as Fig. 6.2), and the simulation for the same excitation is shown in the red line. The enhancement of the LL0 signal in the simulations is given by $R^{model} = 13.8$, within 20% of the experimental value.

of signal strength, as shown in Fig. 7.7. Again the signal from LL0 is greatly enhanced relative to LL1, just as in the experiment. Recall that for the experiments we calculated the relative emission ratio $R$, which gives an estimate for the amount of LL0 enhancement relative to the excitation density (see Eq. (6.1)). For the MDQW sample and this excitation condition, we found $R^{doped} = 17.5$, where $R = 1$ corresponds to a "normal" response. For the simulations we find $R^{model} = 13.8$, which is within 20% of the experimental value.

The model is able to describe the time dependence of this signal as well. Recall that for excitation of LL1, the LL0 signal had a very large $\Delta t < 0$ signal, so that the signal was almost symmetric as a function of time delay. In Fig. 7.8 we show $S_{SR}^{model}(\Delta t\ )$ at the LL0 and LL1 emission energies, compared to the experimental results. While we do not quite see a symmetric signal, the $\Delta t < 0$ signal is much larger from LL0 than from LL1, as

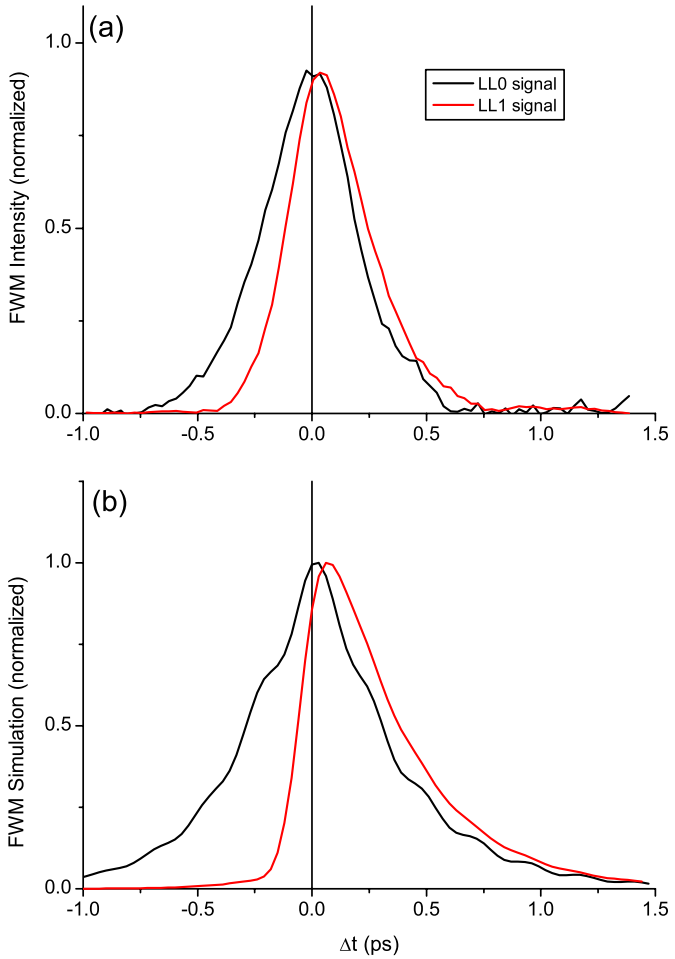


Figure 7.8: Simulation of the FWM signal as a function of $\Delta t$ for the preferential excitation of LL1. The experimental results are shown in (a), for sample C for $B = 8$T, when we excite LL1 preferentially (60:1 excitation of LL1:LL0, same as Fig. 6.3), at the LL0 emission energy (black curve) and the LL1 emission energy (red curve). The simulated data is shown in (b) for the same conditions. The signals have been normalized for clarity. Notice the large negative delay signal from the LL0 signal.

in the experiment. We believe that by including the center of mass scattering of the MPs in Eq. (7.23) and in $\gamma$, the signal could be made symmetric. However, this requires a more detailed calculation of the full theory in Appendix A, which is beyond the scope of this work.

Overall, our average polarization model can capture the main experimental results quite well. Let us analyze the different elements of the model, to see where the effects come from. To do this, it is easiest to look at the signal when we excite entirely into LL1. In Fig. 7.9, we show $S_{SR}^{model}(\Delta t\ )$ at the two LL emission energies, for each of the individual source terms which appear in Eqs. (7.24)-(7.25). In the upper panel, we see that the signal from LL1 is determined by the PB nonlinearity for positive times, with a very small negative time signal given by the Shake–up term. The BCI source term is very weak in this case, as we expect due to the screening of the Coulomb interaction by the 2DEG. The MPC contribution, which comes from the magnetoplasmon propagation as described in Fig. 7.4, is entirely absent from LL1, as discussed in the previous section. However, looking at the lower panel, we find that the MPC source term completely dominates the others in the signal from LL0, giving a large negative time delay signal, and an overall signal which is comparable in size to the LL1 signal, as we see in the experiment. The BCI and PB contributions are both more than an order of magnitude lower than the MPC contribution, and the Shake–up term is even weaker. We have kept the latter term in the model to demonstrate some of the additional ways that the 2DEG can influence the FWM signal, but in fact the term is quite weak in our model, and provides a time dependence similar to the BCI term. However, it is clear that the magnetoplasmon correlation term is essential

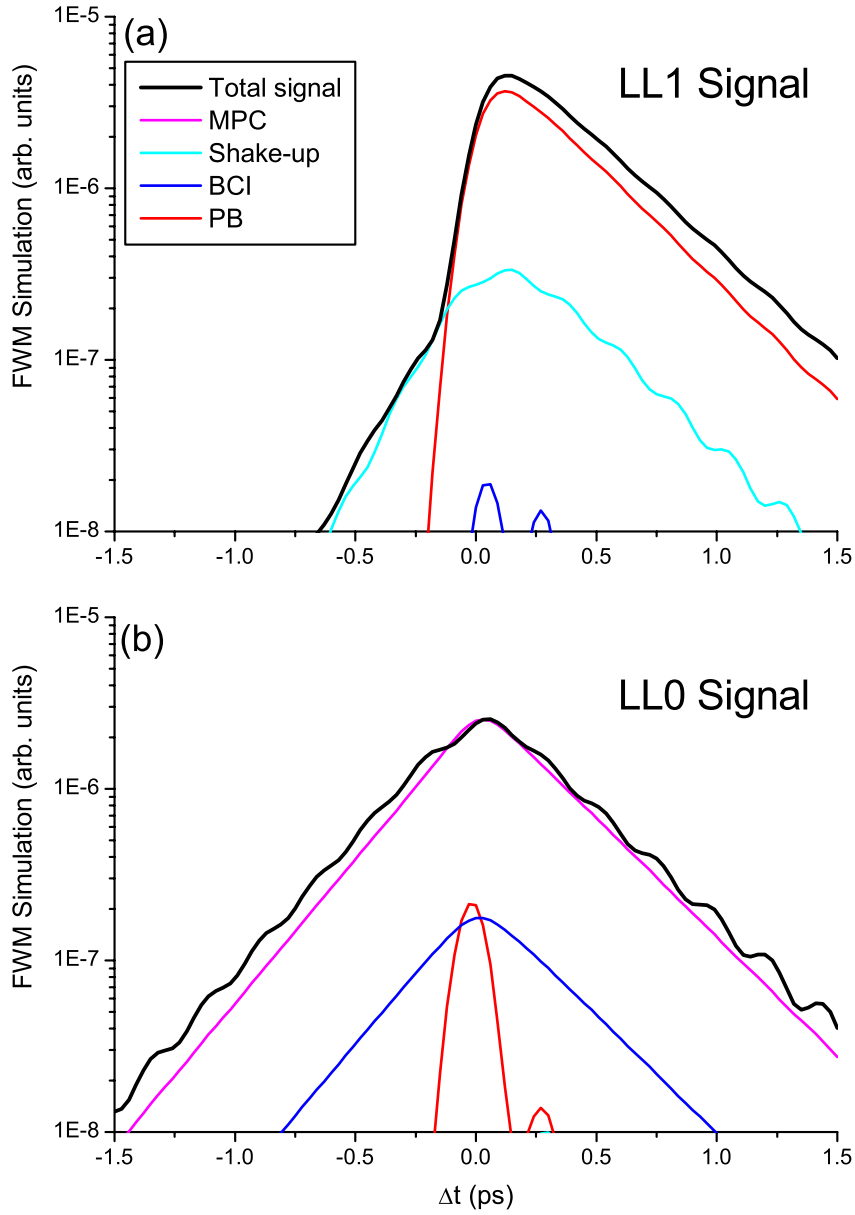


Figure 7.9: FWM vs. $\Delta t$ calculated from the model, showing each source term. The upper panel (a) shows the signal from LL1, and the lower panel (b) shows the signal from LL0, showing the contribution of the Pauli blocking (PB), bare Coulomb interaction (BCI), mean–field 2DEG shake–up interaction (Shake–up), and magnetoplasmon correlation (MPC) source terms to the total signal. We see that the LL1 signal is dominated by the PB contribution, while the LL0 signal is entirely determined by the MPC source term.

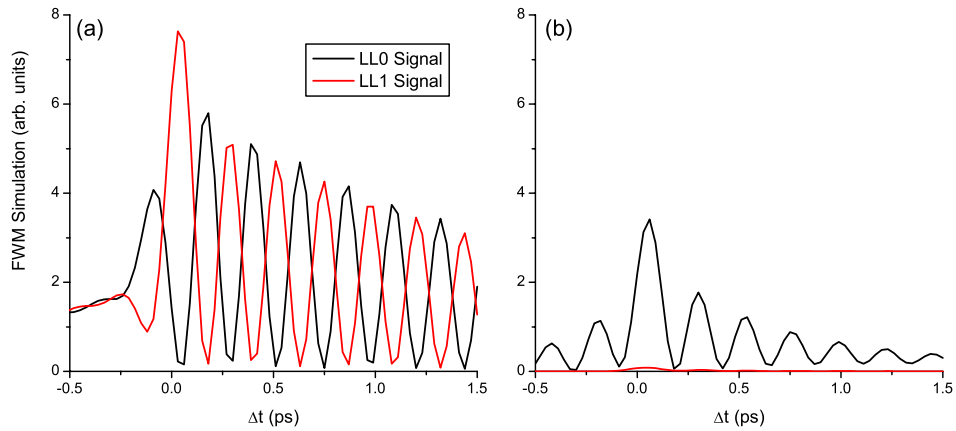


Figure 7.10: FWM vs. $\Delta t$ calculated from the model, with and without $W$. The fist panel (a) shows the signal vs. $\Delta t$ from LL1 (red) and LL0 (black) when $W = 0$ and there are no effects from the 2DEG. The second panel (b) shows the signal when $W = 4.5$ meV$^2$ and all the 2DEG interaction source terms are active. While the existence of the $X \leftrightarrow Y$ scattering channel decreases the LL0 signal slightly, it has a huge effect on the LL1 signal, reducing it by more than an order of magnitude.

to model the optical dynamics of the 2DEG system.

In the case where we excite into both levels equally, we expect there to be strong PB in both LL1 and LL0. The much stronger signal from LL0 in this case comes from the $X \leftrightarrow Y$ scattering process described by $\bar{P}(t)$ and with amplitude $W$. This can be seen in in Fig. 7.10, which shows the change in the strength of the FWM signal from each LL, as we turn on the coupling parameter $W$. The coupling induced by $W$ has a drastic effect on the LL1 signal, reducing it by almost two orders of magnitude. The LL0 signal is also reduced, but only by about a factor of 2, resulting in a much larger signal from LL0 relative to LL1.

## 7.6 Conclusion

In this chapter we have outlined some of the theoretical challenges which must be faced to understand the role of the correlated 2DEG in the optical response of our MDQW samples. We discussed the existence of new types of excited states, such as the four–particle state $Y$, with which the magnetoexcitons can interact, and the magnetoplasmon states which can be excited in Raman–like processes. We developed a generalized average polarization model (as in Ch. 2.5) based on the microscopic theory including these interactions (see Appendix A), and solved the model to simulate our experimental results. We have seen that the magnetoplasmon correlations and the $X \leftrightarrow Y$ scattering are necessary to explain the enhanced signal from LL0, and the large negative time delay signal seen in the experiments.

The model was based on several approximations, described here and in Apps. B and C, which significantly reduced the size of the calculation required to simulate our results. Work is continuing to go beyond these approximations, by keeping more basis states defined using the Lanczos method, for example to treat 2–MP scattering and center of mass motion directly. However, our model is able to qualitatively describe the unusual experimental results.

# Chapter 8

# Conclusion

## 8.1 Summary

We performed ultrafast two–pulse degenerate four–wave mixing on modulation doped GaAs quantum wells in high magnetic fields. The presence of a correlated two dimensional electron gas in the sample, capable of interacting with the photo–excited electron hole pairs, drastically affected the dynamics of the excited system. We interpreted this data using a theory which takes the electron gas in the ground state and its excitations into account, and develop a model which reproduces the most salient experimental results.

Measurements in which the laser was narrowed and tuned to excite only into the lowest partially empty Landau level showed a decay time which varied by an order of magnitude as a function of the filling factor of the electron gas, with a transition from Markovian to non–Markovian behavior with increasing magnetic field, due to the influence of the intra–Landau level electron gas excitations. In the former case, the dephasing of the signal was dominated by other relaxation processes (e.g. phonons or Auger effects), and the

dephasing time followed that of the number of available scattering states, exhibiting peaks at full Landau levels. At high magnetic field, the FWM signal showed strong evidence of memory effects, including an asymmetric four–wave mixing lineshape and a spectral shift, which could be understood in terms of scattering between the photo–excited carriers and the magnetoroton excitations of the electron gas within the lowest Landau level.

Four–wave mixing measurements in which the laser was tuned to excite carriers into both the lowest and next highest Landau levels (LL0 and LL1 respectively), or only into the upper level, gave insight into the correlations between the photo–excited carriers and the inter–Landau level excitations of the electron gas. We compared these measurements directly with similar measurements in undoped quantum wells, which are well described by the mean–field, RPA level theory (see Ch. 2.5.1). In the doped sample, we observe a large transfer of signal strength from LL0 to LL1, and unusual features in the spectra as a function of the time delay. When both levels are excited, we see only signal from LL0, but with very large beats as a function of time delay. When we excite only into LL1, we see a strong signal from LL0 for both positive *and negative* time delay, which is almost symmetric around $\Delta t = 0$ . We found that these results require that LL0 is not completely full of doped electrons before excitation ($\nu < 2$), and that at least a small part of the laser pulse excites LL0. As the overall laser intensity was increased to excite more electron–hole pairs, beats appeared in the signal from LL0, and as the mean–field interactions between the photo–excited carriers began to dominate over the signal due to exciton–electron gas correlations, the doped and undoped signals began approach one another.

By including in our theory, in addition the exciton–exciton interactions present in

undoped semiconductors, the interaction between the photo–excited carriers and the inter–Landau level magnetoplasmon excitations of the electron gas, we were able to interpret these results, and qualitatively simulate the effects of these interaction effects. Processes such as (1) the scattering of a photo–excited electron–hole pair into a nearly resonant four–particle state consisting of an electron–hole pair and a magnetoplasmon and (2) time dependent inter–Landau level carrier scattering mediated by magnetoplasmons, similar to coherent antiStokes Raman scattering, were shown to lead to the transfer of signal strength to LL0 and the unusual time dependence of the signal.

## 8.2 Future work

This research demonstrates the power of ultrafast spectroscopy to explore interesting and open questions in many–body physics, and opens the door to several possibilities for future exploration.

Having started down the road to understanding the dynamics of the excitations of the two dimensional electron gas in a high magnetic field, the next logical step is to measure the dynamics of the quasiparticle excitations of the fractional quantum Hall system. This requires lower temperatures, such as in a He3 cryostat or a dilution refrigerator, and also higher mobility samples. To significantly improve on the mobility we must grow high–quality single heterojunction samples (capable of mobilities well over $10^6$ cm$^2$/Vs).

Another interesting issue which we have not addressed is the interactions between the different hole states. While our interpretation is able to qualitatively explain the data, we are prevented from a quantitative analysis until the presence of additional valence band

states can be taken into account. Also, experiments performed with other polarization states can access several different hole states at once, as shown in the linear absorption spectra in Ch. 4. These additional valence band states can have an effect on the interactions as well.

In addition to the charge excitations of the electron gas, there are spin excitations, which can have very long lifetimes. The spin dynamics of this system, particularly near integer filling factors, is a topic of some interest. For example, at filling factor $\nu = 1$ (the so–called "quantum Hall ferromagnet") the lowest lying charged excitation is a Skyrmion, or spin texture [25, 93]. In the interacting system, it becomes energetically favorable to spread a single flipped spin over several electrons, leading to a spatial spin pattern, or texture. Skyrmions have been observed using several techniques [1, 12, 78, 69], but the dynamics of the system have never been investigated.

# Bibliography

[1] E. H. Aifer, B. B. Goldberg, and D. A. Broido, *Evidence of Skyrmion excitations about nu =1 in n-modulation-doped single quantum wells by interband optical transmission*, Phys. Rev. Lett. **76**, 680 (1996).

[2] O. Akimoto and H. Hasegawa, *Interband optical transitions in extremely anisotropic semiconductors. II. Coexistence of exciton and the Landau levels*, J. Phys. Soc. Jpn. **22**, 181 (1967).

[3] L. Allen and J. H. Eberly, *Optical Resonance and Two-Level Atoms*, Dover, New York, 1987.

[4] M. Altarelli, U. Ekenberg, and A. Fasolino, *Calculations of hole subbands in semiconductor quantum wells and superlattices*, Phys. Rev. B, **32**, 5138 (1985).

[5] V. M. Axt, *Dynamische dichtematrixtheorie kohärente erzeugter korrelationen an der halbleiterbandkante*, Ph.D. thesis, Rheinisch-Westfälischen Technischen Hochschule, 1994.

[6] V. M. Axt, S. R. Bolton, U. Neukirch, L. J. Sham, and D. S. Chemla, *Evidence*

*of six-particle Coulomb correlations in six-wave-mixing signals from a semiconductor quantum well*, Phys. Rev. B, **63**, 115303/1 (2001).

[7] V. M. Axt and S. Mukamel, *Nonlinear optics of semiconductor and molecular nanostructures; a common perspective*, Rev. Mod. Phys. **70**, 145 (1998).

[8] V. M. Axt and A. Stahl, *A dynamics-controlled truncation scheme for the hierarchy of density matrices in semiconductor optics*, Z. Phys. B, **93**, 195 (1994).

[9] V. M. Axt, K. Victor, and A. Stahl, *Influence of a phonon bath on the hierarchy of electronic densities in an optically excited semiconductor*, Phys. Rev. B, **53**, 7244 (1996).

[10] S. Bar-Ad and I. Bar-Joseph, *Exciton spin dynamics in GaAs heterostructures*, Phys. Rev. Lett. **68**, 349 (1992).

[11] S. Bar-Ad, I. Bar-Joseph, Y. Levinson, and H. Shtrikman, *Coherent optical spectroscopy of electron scattering in a two-dimensional electron gas in high magnetic fields*, Phys. Rev. Lett. **72**, 776 (1994).

[12] S. E. Barrett, G. Dabbagh, L. N. Pfeiffer, K. W. West, and R. Tycko, *Optically pumped NMR evidence for finite-size Skyrmions in GaAs quantum wells near Landau level filling* $\nu = 1$, Phys. Rev. Lett. **74**, 5112 (1995).

[13] G. Bartels, A. Stahl, V. M. Axt, B. Haase, U. Neukirch, and J. Gutowski, *Identification of higher-order electronic coherences in semiconductors by their signature in four-wave-mixing signals*, Phys. Rev. Lett. **81**, 5880 (1998).

[14] G. Bastard, *Wave mechanics applied to semiconductor heterostructures*, Halstead Press, New York, 1988.

[15] G. E. W. Bauer and T. Ando, *Theory of magnetoexcitons in quantum wells*, Phys. Rev. B, **37**, 3130 (1988).

[16] J. P. Blaizot and G. Ripka, *Quantum theory of finite systems*, MIT Press, Cambridge, MA, 1986.

[17] S. R. Bolton, U. Neukirch, L. J. Sham, D. S. Chemla, and V. M. Axt, *Demonstration of sixth-order Coulomb correlations in a semiconductor single quantum well*, Phys. Rev. Lett. **85**, 2002 (2000).

[18] I. Brener, W. H. Knox, and W. Schaefer, *Virtual excitation of the Fermi-edge singularity in modulation-doped quantum wells*, Phys. Rev. B, **51**, 2005 (1995).

[19] D. A. Broido and L. J. Sham, *Effective masses of holes at GaAs-AlGaAs heterojunctions*, Phys. Rev. B, **31**, 888 (1985).

[20] E. Burstein, A. Pinczuk, and D. L. Mills, *Inelastic light scattering by charge carrier excitations in two-dimensional plasmas: theoretical considerations*, Surf. Science **98**, 451 (1980).

[21] D. S. Chemla, *Ultrafast transient nonlinear optical processes in semiconductors*, Nonlinear optics in semiconductors (R. K. Willardson and A. C. Beers, eds.), Academic Press, New York, 1999.

[22] D. S. Chemla and J. Shah, *Many body and correlation effects in semiconductors*, Nature **411**, 549 (2001).

[23] V. Chernyak, S. Yokojima, T. Meier, and S. Mukamel, *Effective Frenkel Hamiltonian for optical nonlinearities in semiconductors: Application to magnetoexcitons*, Phys. Rev. B, **58**, 4496 (1998).

[24] S. L. Chuang, *Physics of Optoelectronic Devices*, Wiley, New York, 1995.

[25] N. R. Cooper and D. B. Chklovskii, *Theory of photoluminescence of the nu =1 quantum Hall state: excitons, spin waves, and spin textures*, Phys. Rev. B, **55**, 2436 (1997).

[26] K. W. DeLong, D. N. Fittinghoff, and R. Trebino, *Practical issues in ultrashort-laser-pulse measurement using frequency-resolved optical gating*, IEEE J. Quantum Electron. **32**, 1253 (1996).

[27] J. P. Eisenstein, L. N. Pfeiffer, and K. W. West, *Coulomb barrier to tunneling between parallel two-dimensional electron systems*, Phys. Rev. Lett. **69**, 3804 (1992).

[28] U. Ekenberg and M. Altarelli, *Subbands and Landau levels in the two-dimensional hole gas at the GaAs-Al$-xGa_{1-x}As$ interface*, Phys. Rev. B, **32**, 3712 (1985).

[29] D. N. Fittinghoff, J. L. Bowie, J. N. Sweetser, R. T. Jennings, M. A. Krumbugel, K. W. DeLong, R. Trebino, and I. A. Walmsley, *Measurement of the intensity and phase of ultraweak, ultrashort laser pulses*, Opt. Lett. **21**, 884 (1996).

[30] N. A. Fromer, P. Kner, D. S. Chemla, R. Lovenich, and W. Schafer, *Correlation effects*

*beyond Hartree-Fock theory and polarization dependence of four-wave mixing in bulk GaAs at high magnetic field*, Phys. Rev. B, **62**, 2516 (2000).

[31] N. A. Fromer, C. E. Lai, D. S. Chemla, I. E. Perakis, D. Driscoll, and A. C. Gossard, *Dynamics of inter-Landau level excitations of a two dimensional electron gas in the quantum Hall regime*, submitted to Phys. Rev. Lett., (2002).

[32] N. A. Fromer, C. Schuller, D. S. Chemla, T. V. Shahbazyan, I. E. Perakis, K. Maranowski, and A. C. Gossard, *Electronic dephasing in the quantum Hall regime*, Phys. Rev. Lett. **83**, 4646 (1999).

[33] S. M. Girvin, A. H. MacDonald, and P. M. Platzman, *Collective-excitation gap in the fractional quantum Hall effect*, Phys. Rev. Lett. **54**, 581 (1985).

[34] S. M. Girvin, A. H. MacDonald, and P. M. Platzman, *Magneto-roton theory of collective excitations in the fractional quantum Hall effect*, Phys. Rev. B, **33**, 2481 (1986).

[35] S. Glutsch, U. Siegner, and D. S. Chemla, *Spatiotemporal dynamics of photon echoes from continuum states in semiconductors*, Phys. Rev. B, **52**, 4941 (1995).

[36] B. B. Goldberg, D. Heiman, A. Pinczuk, L. Pfeiffer, and K. West, *Optical investigations of the integer and fractional quantum Hall effects: energy plateaus, intensity minima, and line splitting in band-gap emission*, Phys. Rev. Lett. **65**, 641 (1990).

[37] C. Hanyou and C. Yia-Chung, *Theory of line shapes of exciton resonances in semiconductor superlattices*, Phys. Rev. B, **39**, 10861 (1989).

[38] M. Hartmann and W. Schaefer, *Real time approach to relaxation and dephasing processes in semiconductors*, Phys. stat. sol. (b) **173**, 165 (1992).

[39] H. Haug and A.-P. Jauho, *Quantum kinetics in transport and optics of semiconductors*, Springer series in solid state sciences, vol. 123, Springer, Berlin, 1996.

[40] H. Haug and S. W. Koch, *Quantum Theory of the Optical and Electronic Properties of Semiconductors*, World Scientific, Singapore, 1990.

[41] R. Haussmann, *Electronic spectral function for a two-dimensional electron system in the fractional quantum Hall regime*, Phys. Rev. B, **53**, 7357 (1996).

[42] R. Haydock, Solid State Phys. **35**, 215 (1980).

[43] D. Heiman, B. B. Goldberg, A. Pinczuk, C. W. Tu, A. C. Gossard, and J. H. English, *Optical anomalies of the two-dimensional electron gas in the extreme magnetic quantum limit*, Phys. Rev. Lett. **61**, 605 (1988).

[44] F. Jahnke, M. Koch, T. Meier, J. Feldmann, W. Schafer, P. Thomas, S. W. Koch, E. O. Gobel, and H. Nickel, *Simultaneous influence of disorder and Coulomb interaction on photon echoes in semiconductors*, Phys. Rev. B, **50**, 8114 (1994).

[45] C. Kallin and B. I. Halperin, *Excitations from a filled Landau level in the two-dimensional electron gas*, Phys. Rev. B, **30**, 5655 (1984).

[46] D. S. Kim, J. Shah, J. E. Cunningham, T. C. Damen, S. Schmitt-Rink, and W. Schafer, *Carrier-carrier scattering in a degenerate electron system: strong inhibition of scattering near the Fermi edge*, Phys. Rev. Lett. **68**, 2838 (1992).

[47] P. Kner, S. Bar-Ad, M. V. Marquezini, D. S. Chemla, R. Lovenich, and W. Schafer, *Effect of magnetoexciton correlations on the coherent emission of semiconductors*, Phys. Rev. B, **60**, 4731 (1999).

[48] P. Kner, S. Bar-Ad, M. V. Marquezini, D. S. Chemla, and W. Schafer, *Magnetically enhanced exciton-exciton correlations in semiconductors*, Phys. Rev. Lett. **78**, 1319 (1997).

[49] P. Kner, W. Schafer, R. Lovenich, and D. S. Chemla, *Coherence of four-particle correlations in semiconductors*, Phys. Rev. Lett. **81**, 5386 (1998).

[50] W. H. Knox, D. S. Chemla, G. Livescu, J. E. Cunningham, and J. E. Henry, *Femtosecond carrier thermalization in dense Fermi seas*, Phys. Rev. Lett. **61**, 1290 (1988).

[51] I. V. Kukushkin, R. J. Haug, K. V. von Klitzing, and K. Ploog, *Hierarchy of the fractional quantum Hall effect states studied by time-resolved magnetoluminescence*, Phys. Rev. Lett. **72**, 736 (1994).

[52] A. V. Kuznetsov, *Coherent and nonMarkovian effects in ultrafast relaxation of photoexcited hot carriers: a model study*, Phys. Rev. B, **44**, 13381 (1991).

[53] A. V. Kuznetsov, *Interaction of ultrashort light pulses with semiconductors: effective Bloch equations with relaxation and memory effects*, Phys. Rev. B, **44**, 8721 (1991).

[54] K. Leo, M. Wegener, J. Shah, D. S. Chemla, E. O. Gobel, T. C. Damen, S. Schmitt-Rink, and W. Schafer, *Effects of coherent polarization interactions on time-resolved degenerate four-wave mixing*, Phys. Rev. Lett. **65**, 1340 (1990).

[55] L. Lepetit, G. Cheriaux, and M. Joffre, *Linear techniques of phase measurement by femtosecond spectral interferometry for applications in spectroscopy*, J. Opt. Soc. Am. B, Opt. Phys. **12**, 2467 (1995).

[56] J. J. LePore, *An improved technique for selective etching of GaAs and* $Ga_{1-x}Al_xAs$, J. Appl. Phys. **51**, 6441 (1980).

[57] I. V. Lerner and Y. E. Lozovik, *Two-dimensional electron-hole system in a strong magnetic field as an almost ideal exciton gas*, Zh. Eksp. Teor. Fiz. **80**, 1488 (1981).

[58] M. Levenson, *Introduction to nonlinear laser spectroscopy*, Academic Press, New York, 1982.

[59] M. Lindberg, R. Binder, and S. W. Koch, *Theory of the semiconductor photon echo*, Phys. Rev. A, **45**, 1865 (1992).

[60] M. Lindberg and S. W. Koch, *Effective Bloch equations for semiconductors*, Phys. Rev. B, **38**, 3342 (1988).

[61] G. Livescu, D. A. B. Miller, D. S. Chemla, M. Ramaswamy, T. Y. Chang, N. Sauer, A. C. Gossard, and J. H. English, *Free carrier and many-body effects in absorption spectra of modulation-doped quantum wells*, IEEE J. Quantum Electron. **24**, 1677 (1988).

[62] S. G. Louie, *First-Principles Theory of Electron Excitation Energies in Solids, Surfaces, and Defects*, Topics in computational materials science (C. Y. Fong, ed.), World Scientific, Singapore, 1997, p. 96.

[63] D. J. Lovering, R. T. Phillips, G. J. Denton, and G. W. Smith, *Resonant generation of biexcitons in a GaAs quantum well*, Phys. Rev. Lett. **68**, 1880 (1992).

[64] J. M. Luttinger, *Quantum theory of cyclotron resonance in semiconductors: general theory*, Phys. Rev. **102**, 1030 (1956).

[65] A. H. MacDonald, *Hartree-Fock approximation for response functions and collective excitations in a two-dimensional electron gas with filled Landau levels*, J. Phys. C, **18**, 1003 (1985).

[66] A. H. MacDonald, H. C. A. Oji, and S. M. Girvin, *Magnetoplasmon excitations from partially filled Landau levels in two dimensions*, Phys. Rev. Lett. **55**, 2208 (1985).

[67] A. H. MacDonald and D. S. Ritchie, *Hydrogenic energy levels in two dimensions at arbitrary magnetic fields*, Phys. Rev. B, **33**, 8336 (1986).

[68] M. Z. Maialle and L. J. Sham, *Interacting electron theory of coherent nonlinear response*, Phys. Rev. Lett. **73**, 3310 (1994).

[69] M. J. Manfra, E. H. Aifer, B. B. Goldberg, D. A. Broido, L. Pfeiffer, and K. West, *Temperature dependence of the spin polarization of a quantum Hall ferromagnet*, Phys. Rev. B, **54**, R17327 (1996).

[70] I. K. Marmorkos and S. Das Sarma, *Magnetoplasmon excitation spectrum for integral filling factors in a two-dimensional electron system*, Phys. Rev. B, **45**, 13396 (1992).

[71] M. V. Marquezini, P. Kner, S. Bar-Ad, J. Tignon, and D. S. Chemla, *Density depen-*

*dence of the spectral dielectric function across a Fano resonance*, Phys. Rev. B, **57**, 3745 (1998).

[72] E. J. Mayer, G. O. Smith, V. Heuckeroth, J. Kuhl, K. Bott, A. Schulze, T. Meier, S. W. Koch, P. Thomas, R. Hey, and K. Ploog, *Polarization dependence of beating phenomena at the energetically lowest exciton transition in GaAs quantum wells*, Phys. Rev. B, **51**, 10909 (1995).

[73] S. Mukamel, *Principles of Nonlinear Optical Spectroscopy*, Oxford University Press, New York, 1995.

[74] U. Neukirch, S. R. Bolton, N. A. Fromer, L. J. Sham, and D. S. Chemla, *Polariton-biexciton transitions in a semiconductor microcavity*, Phys. Rev. Lett. **84**, 2215 (2000).

[75] U. Neukirch, S. R. Bolton, L. J. Sham, and D. S. Chemla, *Electronic four-particle correlations in semiconductors: Renormalization of coherent pump-probe oscillations*, Phys. Rev. B, **61**, R7835 (2000).

[76] K. Ohno, K. Esfarjani, and Y. Kawazoe, *Computational materials science*, Springer Verlag, Berlin, 1999.

[77] K. Ohtaka and Y. Tanabe, *Theory of the soft-X-ray edge problem in simple metals: historical survey and recent developments*, Rev. Mod. Phys. **62**, 929 (1990).

[78] J. L. Osborne, A. J. Shields, M. Y. Simmons, N. R. Cooper, D. A. Ritchie, and M. Pepper, *Excitonic recombination processes in spin-polarized two-dimensional electron gases*, Phys. Rev. B, **58**, R4227 (1998).

[79] T. Ostreich, K. Schonhammer, and L. J. Sham, *Exciton-exciton correlation in the nonlinear optical regime*, Phys. Rev. Lett. **74**, 4698 (1995).

[80] T. Ostreich, K. Schonhammer, and L. J. Sham, *Theory of exciton-exciton correlation in nonlinear optical response*, Phys. Rev. B, **58**, 12920 (1998).

[81] I. E. Perakis, *Many-body effects in metals, modulation doped quantum wells and doped semiconductors*, Ph.D. thesis, University of Illinois at Urbana-Champaign, 1992.

[82] I. E. Perakis, *Many-body effects in nonlinear spectroscopy: a time-dependent transformation approach*, Chem. Phys. **210**, 259 (1996).

[83] I. E. Perakis, I. Brener, W. H. Knox, and D. S. Chemla, *Nonlinear optical study of the Fermi edge singularity: differences from atomic excitons in the virtual excitation regime*, J. Opt. Soc. Am. B, **13**, 1313 (1996).

[84] I. E. Perakis and Y. C. Chang, *Noncanonical-transformation approach to the problem of an itinerant particle interacting with a Fermi sea*, Phys. Rev. B, **47**, 6573 (1993).

[85] I. E. Perakis and D. S. Chemla, *AC Stark effect of the Fermi edge singularity: observation of "excitonic polarons"?*, Phys. Rev. Lett. **72**, 3202 (1994).

[86] I. E. Perakis, N. A. Fromer, and D. S. Chemla, *Collective effects in the ultrafast dynamics of a 2DEG in the quantum Hall regime*, To Be Published, (2002).

[87] I. E. Perakis and T. V. Shahbazyan, *Canonical transformation approach to the ultrafast nonlinear optical dynamics of semiconductors*, Int. J. Mod. Phys. B **13**, 869 (1999).

[88] I. E. Perakis and T. V. Shahbazyan, *Many-body correlation effects in the ultrafast non-linear optical response of confined Fermi seas*, Surf. Sci. Rep. **40**, 3 (2000).

[89] I. E. Perakis and C. Yia-Chung, *Noncanonical-transformation approach to the X-ray-edge problem*, Phys. Rev. B, **44**, 5877 (1991).

[90] I. E. Perakis and C. Yia-Chung, *Singularities in the optical spectra of a system involving a Fermi sea of electrons and a localized hole: a method for obtaining many-body wave functions*, Phys. Rev. B, **43**, 12556 (1991).

[91] A. Pinczuk, B. S. Dennis, L. N. Pfeiffer, and K. West, *Observation of collective excitations in the fractional quantum Hall effect*, Phys. Rev. Lett. **70**, 3983 (1993).

[92] A. Pinczuk, J. P. Valladares, D. Heiman, A. C. Gossard, J. H. English, C. W. Tu, L. Pfeiffer, and K. West, *Observation of roton density of states in two-dimensional Landau-level excitations*, Phys. Rev. Lett. **61**, 2701 (1988).

[93] T. Portengen, J. R. Chapman, V. Nikos Nicopoulos, and N. F. Johnson, *Optics with quantum Hall Skyrmions*, Int. J. Mod. Phys. B **12**, 1 (1998).

[94] N. Primozich, T. V. Shahbazyan, I. E. Perakis, and D. S. Chemla, *Coherent ultrafast optical dynamics of the Fermi-edge singularity*, Phys. Rev. B, **61**, 2041 (2000).

[95] S. Das Sarma and A. Pinczuk (eds.), *Perspectives in quantum Hall effects*, Wiley, New York, 1997.

[96] K. El Sayed, S. Schuster, H. Haug, F. Herzel, and K. Henneberger, *Subpicosecond plasmon response: buildup of screening*, Phys. Rev. B, **49**, 7337 (1994).

[97] W. Schafer, D. S. Kim, J. Shah, T. C. Damen, J. E. Cunningham, K. W. Goosen, L. N. Pfeiffer, and K. Kohler, *Femtosecond coherent fields induced by many-particle correlations in transient four-wave mixing*, Phys. Rev. B, **53**, 16429 (1996).

[98] W. Schafer, R. Lovenich, N. A. Fromer, and D. S. Chemla, *From coherently excited highly correlated states to incoherent relaxation processes in semiconductors*, Phys. Rev. Lett. **86**, 344 (2001).

[99] S. Schmitt-Rink and D. S. Chemla, *Collective excitations and the dynamical stark effect in a coherently driven exciton system*, Phys. Rev. Lett. **57**, 2752 (1986).

[100] S. Schmitt-Rink, D. S. Chemla, and H. Haug, *Nonequilibrium theory of the optical Stark effect and spectral hole burning in semiconductors*, Phys. Rev. B, **37**, 941 (1988).

[101] S. Schmitt-Rink, D. S. Chemla, and D. A. B. Miller, *Linear and nonlinear optical properties of semiconductor quantum wells*, Adv. Phys. **38**, 89 (1989).

[102] S. Schmitt-Rink, J. B. Stark, W. H. Knox, D. S. Chemla, and W. Schafer, *Optical properties of quasi-zero-dimensional magneto-excitons*, Appl. Phys. A, **A53**, 491 (1991).

[103] J. R. Schrieffer, *Theory of Superconductivity*, The Benjamin/Cummings Publishing Co., Reading, MA., 1964.

[104] L. Schultheis, J. Kuhl, A. Honold, and C. W. Tu, *Picosecond phase coherence and orientational relaxation of excitons in GaAs*, Phys. Rev. Lett. **57**, 1797 (1986).

[105] J. Shah, *Ultrafast spectrisopy of semiconductors and semiconductor nanostructures*, Springer, Heidelberg, 1999.

[106] T. V. Shahbazyan, I. E. Perakis, and M. E. Raikh, *Spin correlations in nonlinear optical response: light-induced Kondo effect*, Phys. Rev. Lett. **84**, 5896 (2000).

[107] T. V. Shahbazyan, N. Primozich, and I. E. Perakis, *Ultrafast Coulomb-induced dynamics of quantum well magnetoexcitons*, Phys. Rev. B, **62**, 15925 (2000).

[108] T. V. Shahbazyan, N. Primozich, I. E. Perakis, and D. S. Chemla, *Femtosecond coherent dynamics of the Fermi-edge singularity and exciton hybrid*, Phys. Rev. Lett. **84**, 2006 (2000).

[109] L. J. Sham, *Theory of the Shallow Impurity States in Semiconductors*, Phys. Rev. **150**, 720 (1966).

[110] M. Shinada and S. Sugano, *Interband optical transitions in extremely anisotropic semiconductors. I. Bound and unbound exciton absorption*, J. Phys. Soc. Jpn. **21**, 1936 (1966).

[111] M. Shinada and K. Tanaka, *Interband optical transitions in extremely anisotropic semiconductors. III. Numerical studies of magneto-optical absorption*, J. Phys. Soc. Jpn. **29**, 1258 (1970).

[112] C. Stafford, S. Schmitt-Rink, and W. Schaefer, *Nonlinear optical response of two-dimensional magnetoexcitons*, Phys. Rev. B, **41**, 10000 (1990).

[113] H. L. Stormer, D. C. Tsui, and A. C. Gossard, *The fractional quantum Hall effect*, Rev. Mod. Phys. **71**, S298 (1999).

[114] R. Trebino and D. J. Kane, *Using phase retrieval to measure the intensity and phase of ultrashort pulses: frequency-resolved optical gating*, J. Opt. Soc. Am. A, Opt. Image Sci. **10**, 1101 (1993).

[115] T. Uenoyama and L. J. Sham, *Many-body theory of magneto-optical spectra in doped quantum wells*, Phys. Rev. B, **39**, 11044 (1989).

[116] K. Victor, V. M. Axt, and A. Stahl, *Hierarchy of density matrices in coherent semiconductor optics*, Phys. Rev. B, **51**, 14164 (1995).

[117] H. Wang, J. Shah, T. C. Damen, S. W. Pierson, T. L. Reinecke, L. N. Pfeiffer, and K. West, *Carrier-distribution-dependent band-gap renormalization in modulation-doped quantum wells*, Phys. Rev. B, **52**, R17013 (1995).

[118] M. Wegener and D. S. Chemla, *Coherent control of electron-phonon quantum kinetics: exploring the weak and the strong coupling regime*, Chem. Phys. **251**, 269 (2000).

[119] M. Wegener, D. S. Chemla, S. Schmitt-Rink, and W. Schafer, *Line shape of time-resolved four-wave mixing*, Phys. Rev. A, **42**, 5675 (1990).

[120] S. Weiss, M. A. Mycek, J. Y. Bigot, S. Schmitt-Rink, and D. S. Chemla, *Collective effects in excitonic free induction decay: do semiconductors and atoms emit coherent light in different ways?*, Phys. Rev. Lett. **69**, 2685 (1992).

[121] S. R. E. Yang, D. A. Broido, and L. J. Sham, *Holes at GaAs-$Al_xGa_{1-x}As$ heterojunctions in magnetic fields*, Phys. Rev. B, **32**, 6630 (1985).

[122] S. R. Eric Yang and L. J. Sham, *Theory of magnetoexcitons in quantum wells*, Phys. Rev. Lett. **58**, 2598 (1987).

[123] S. Yokojima, T. Meier, V. Chernyak, and S. Mukamel, *Femtosecond four-wave-mixing spectroscopy of interacting magnetoexcitons in semiconductor quantum wells*, Phys. Rev. B, **59**, 12584 (1999).

# Appendix A

# Derivation of the theory

## A.1 Introduction

In this appendix we present the full derivation of the theory outlined in Ch. 7. The theory is based on a canonical transformation and time dependent coherent states, as in Refs. [82, 83, 85, 87, 88, 94, 108], to describe the coherent dynamics of a system containing a strongly correlated ground state with long lived low energy excitations.

In Section A.2 we set up the general problem and discuss the nature of the states that contribute to the optical spectra for the filling factors of interest. In Section A.3 we study the time evolution of a general two–band strongly correlated system, without any assumptions about its nature. We introduce a decomposition of the photo–excited many–body states that allows us to separate out the contributions to the time evolved states which are due to the interaction and correlation effects. In Section A.4 we use the above decomposition in order to obtain the equation of motion for the third–order nonlinear polarization of a general strongly correlated system. We separate out the contributions

that are analogous to those in a multi–level system, and identify the new time dependent contributions that arise from the interactions and the correlations. In Section A.5 we discuss the different dephasing contributions and introduce a basis of many–body states, derived using a Lanczos–like recursive method [42].

## A.2 Problem setup

We are interested in developing a comprehensive approach to the problem of the nonlinear optical response of a semiconductor QW containing a 2DEG in a large magnetic field. This system is described by the Hamiltonian [40] ($\hbar = 1$),

$$H_{\rm tot}(t) = H - \mu\mathcal{E}(t)\hat{X}^\dagger - \mu\mathcal{E}^*(t)\hat{X}. \tag{A.1}$$

Here, $H$ is the "bare" semiconductor Hamiltonian [40, 107, 23, 123],

$$H = \sum_{n,\mathbf{k}} \Omega_c^c(n+1/2)\hat{e}^\dagger_{\mathbf{k},n}\hat{e}_{\mathbf{k},n} + \sum_{n,\mathbf{k}}[E_g + \Omega_c^v(n+1/2)]\hat{h}^\dagger_{-\mathbf{k},n}\hat{h}_{-\mathbf{k},n} + V_{ee} + V_{hh} + V_{eh}, \tag{A.2}$$

$E_g$ is the bandgap, $V_{ee}, V_{eh}$, and $V_{hh}$ are the electron–electron , electron–hole, and hole–hole interactions respectively (among the photo–excited carriers *and* with the 2DEG as well), $\mathcal{E}(t)$ is the applied optical field, and $\mu$ is the interband transition matrix element. The magnetic field splits the conduction and valence bands into electron ($e$) and hole ($h$) Landau Levels, $e$–LL$n$ and $h$–LL$n$. $\hat{e}^\dagger_{\mathbf{k},n}$ is the creation operator of the LL$n$ conduction band electron, $n = 0, 1, \cdots$, with cyclotron energy $\Omega_c^c$, and $\hat{h}^\dagger_{\mathbf{k},n}$ is the creation operator of the LL$n$ valence band hole, with cyclotron energy $\Omega_c^v$. The optical transition operator $\hat{X}^\dagger$ is given by

$$\hat{X}^\dagger = \sum_{n,\mathbf{k}} \hat{e}^\dagger_{\mathbf{k},n}\hat{h}^\dagger_{-\mathbf{k},n} = \sum_n \sqrt{N_n}\hat{X}^\dagger_n. \tag{A.3}$$

In the above equation we introduced the creation operator $\hat{X}_n^\dagger$ of the LL$n$ magnetoexciton state $|X_n\rangle = \hat{X}_n^\dagger|0\rangle$, where $|0\rangle$ is the ground state [107] and

$$\hat{X}_n^\dagger = \frac{1}{\sqrt{N_n}} \sum_{\mathbf{k}} \hat{e}_{\mathbf{k},n}^\dagger \hat{h}_{-\mathbf{k},n}^\dagger. \tag{A.4}$$

Here $N_n = N(1-\nu_n)$, and $N = L^2/2\pi l_c^2$ is the LL degeneracy, $l_c$ is the magnetic length, $L$ is the system size, and $\nu_n = \frac{1}{N}\sum_{\mathbf{k}}\langle 0|\hat{e}_{\mathbf{k},n}^\dagger \hat{e}_{\mathbf{k},n}|0\rangle$ describes the filling of LL$n$. We will use the shorthand notation $X$ to designate a general magnetoexciton. The magnetic fields of interest for our experiments correspond to a partial filling of the lowest LL, i.e., the LL$n$ are empty ($\nu_n = 0$) for $n > 0$, while $0 < \nu_0 < 1$ (we neglect the spin in this discussion).

The magnetoexciton operators of Eq. (A.4) do not obey the commutation relationship of point boson operators, reflecting the fact that they are composite objects built out of fermions. Instead, they satisfy the commutation relation

$$[\hat{X}_n, \hat{X}_m^\dagger] = \delta_{nm}\left(1 - \frac{\Delta\hat{N}_n}{N_n}\right), \tag{A.5}$$

which expresses the underlying Fermi statistics. Here the number operator

$$\Delta\hat{N}_n = \sum_{\mathbf{k}} \left(\hat{h}_{-\mathbf{k},n}^\dagger \hat{h}_{-\mathbf{k},n} + \hat{e}_{\mathbf{k},n}^\dagger \hat{e}_{\mathbf{k},n}\right) - N\nu_n \tag{A.6}$$

describes the fluctuations of the LL$n$ carrier number due to Pauli blocking, or phase space filling effects.

Within the dipole approximation, the optical response is determined by the polarization of the photo–excited system,

$$P(t) = \mu\langle\psi|\hat{X}|\psi\rangle = \mu\sum_n \sqrt{N_n}P_n(t), \tag{A.7}$$

where $|\psi\rangle$ is the semiconductor wavefunction that evolves from the ground state $|0\rangle$ according to the Schrödinger equation for the total Hamiltonian $H_{tot}(t)$. In the last term of Eq.

(A.7) we have expressed $P(t)$ in terms of the average values $P_n(t)$ of the magnetoexciton operators,

$$P_n(t) = \langle\psi|\hat{X}_n|\psi\rangle. \tag{A.8}$$

As in the theoretical approaches of Refs. [80, 79, 9, 7], we note the one to one correspondence between photon absorption/emission processes and $e$–$h$ pair creation/destruction. However, since there is a 2DEG present prior to excitation, when following the effects of the applied fields it is more convenient to count the number of valence band holes in a given state. We will use the shorthand notation 0–$h$, 1–$h$, 2–$h$ ... to label these states. We can decompose the time evolved state $|\psi\rangle$ in this manner, yielding

$$|\psi\rangle = |\psi_0\rangle + |\psi_1\rangle + |\psi_2\rangle, \tag{A.9}$$

where $|\psi_i\rangle$, $i = 0, 1, 2$, describes the contribution of the $i$–$h$ states. Substituting the above decomposition in the Schrödinger equation with the Hamiltonian $H_{tot}(t)$, we obtain up to third–order in the optical field

$$i\frac{\partial}{\partial t}|\psi_0\rangle - H|\psi_0\rangle = -\mu\mathcal{E}^*(t)\hat{X}|\psi_1\rangle, \tag{A.10}$$

$$i\frac{\partial}{\partial t}|\psi_1\rangle - H|\psi_1\rangle = -\mu\mathcal{E}(t)\hat{X}^\dagger|\psi_0\rangle - \mu\mathcal{E}^*\hat{X}|\psi_2\rangle, \tag{A.11}$$

$$i\frac{\partial}{\partial t}|\psi_2\rangle - H|\psi_2\rangle = -\mu\mathcal{E}(t)\hat{X}^\dagger|\psi_1\rangle, \tag{A.12}$$

with the initial condition that $|\psi_i(-\infty)\rangle = \delta_{i,0}|0\rangle$. The physics of the above equations is clearly displayed: $|\psi_0\rangle$ is coupled to $|\psi_1\rangle$ by the destruction of one $e$-$h$ pair, $|\psi_1\rangle$ is coupled to $|\psi_2\rangle$ by the destruction of one $e$–$h$ pair and to $|\psi_0\rangle$ by the creation of one $e$–$h$ pair, and $|\psi_2\rangle$ is coupled to $|\psi_1\rangle$ by the creation of one $e$–$h$ pair.

During their time evolution, the $X$ states interact with the 2DEG and create

2DEG excitations. For our experimental conditions, the dominant 2DEG excitations are the collective modes due to the coherent promotion of an electron from LL0 to a higher LL, or inter–LL magnetoplasmons (MP) [45, 65, 66]. Such MP eigenstates have the form [66]

$$|M_{\mathbf{q}}\rangle = \sum_{\mathbf{k}nn'} \rho_{nn'}(\mathbf{q})\hat{e}^{\dagger}_{\mathbf{k}+\mathbf{q},n}\hat{e}_{\mathbf{k},n'}|0\rangle, \tag{A.13}$$

where $|0\rangle$ is the ground state and the amplitudes $\rho_{nn'}(\mathbf{q})$ are related to the LL$n' \rightarrow$ LL$n$ contribution to the density operator [66]. For the magnetic fields of interest here, and for photo–excitation of only LL0 and LL1, the main contribution to the optical spectra comes from the LL0 $\rightarrow$ LL1 MPs (referred to from now on as the MP states), whose energy is close to the LL0 $\rightarrow$ LL1 energy and $\Omega_c^c$ [45, 65, 66]. The other MP excitations, and the incoherent particle–hole 2DEG excitations analogous to those in an ordinary Fermi liquid, have energies well above $\Omega_c^c$ and their contribution is therefore suppressed.

## A.3 Time dependent interaction effects

In this section we consider the time evolution of the photo–excited system, where we are particularly interested in the contributions to $|\psi\rangle$ due to Coulomb interactions. For that we can separate out the non–interacting contributions to the photo–excited state Eq. (A.9), and identify the contributions to the 0–$h$, 1–$h$, and 2–$h$ states due to Coulomb correlation. Therefore we decompose $|\psi_0\rangle$, $|\psi_1\rangle$ and $|\psi_2\rangle$ according to:

$$|\psi_0\rangle = \langle 0|\psi\rangle|0\rangle + |\psi_0^{int}\rangle\ ,\ |\psi_0^{int}\rangle = -\sum_n P_n^{L*}\hat{X}_n|\bar{\psi}_1\rangle + |\bar{\psi}_0\rangle, \tag{A.14}$$

where $\langle 0|\psi_0^{int}\rangle = \langle 0|\bar{\psi}_0\rangle = 0$,

$$|\psi_1\rangle = \sum_n P_n^L|X_n\rangle + |\bar{\psi}_1\rangle, \tag{A.15}$$

where $\langle X_n|\bar{\psi}_1\rangle = 0$, and

$$|\psi_2\rangle = \frac{1}{2}\sum_{nn'} P_n^L P_{n'}^L |X_n X_{n'}\rangle + |\psi_2^{int}\rangle \ , \ |\psi_2^{int}\rangle = \sum_n P_n^L \hat{X}_n^\dagger ||\bar{\psi}_1\rangle + |\bar{\psi}_2\rangle, \tag{A.16}$$

where the state $|X_n X_{n'}\rangle = \hat{X}_n^\dagger \hat{X}_{n'}^\dagger |0\rangle$ describes two non–interacting magnetoexcitons. We have introduced the LL$n$ exciton amplitude

$$P_n^L(t) = \langle X_n|\psi_1\rangle = \langle 0|\hat{X}_n|\psi\rangle, \tag{A.17}$$

which, to first order in the optical field reduces to the LL$n$ linear polarization. In the above equations, the first parts reduce to the usual independent–level system contributions, whereas $|\psi_0^{int}\rangle$, $|\bar{\psi}_0\rangle$, $|\bar{\psi}_1\rangle$, $\psi_2^{int}\rangle$ and $|\bar{\psi}_2\rangle$ account for the Coulomb interaction among the $X$ and with the 2DEG, which we will analyze in detail below. The states $|\psi_0^{int}\rangle$, $|\psi_2^{int}\rangle$, and $|\psi_1\rangle$ also allow us to separate, in the equations of motion Eqs. (A.10), (A.11), and (A.12), the source terms proportional to the optical field from the source terms proportional the polarizations $P_n^L(t)$, which lead to different time dependencies.

Clearly, the correlation effects in the third–order nonlinear polarization are contained in the states $|\bar{\psi}_0\rangle$, $|\bar{\psi}_1\rangle$, and $|\bar{\psi}_2\rangle$. Here we will analyze the dynamics of these states and determine their equations of motion. In order to obtain the third–order polarization, we only need to study the time evolution of $|\psi\rangle$ up to second order in the optical field.

It is easiest to start with the 1–$h$ time evolved state. In Eq. (A.15), the first term is the LL$n$ linear polarization contribution which is proportional to the LL$n$ magnetoexciton state $|X_n\rangle$, with the amplitude $P_n^L(t)$. The second term in Eq. (A.15) is the {1–$h$/2DEG*} contribution originating from the $X$–2DEG scattering during the time evolution of the photo–excited magnetoexcitons. Such interactions can be described by considering the

action of the Hamiltonian $H$ on the magnetoexciton states $|X_n\rangle$. By subtracting all of the exciton contributions, the state $H|X_n\rangle$ can be expressed in the general form

$$H|X_n\rangle = \Omega_n|X_n\rangle - \sum_{n'\neq n} V_{n'n}|X_{n'}\rangle + |Y_n\rangle, \tag{A.18}$$

where

$$\Omega_n = \langle X_n|H|X_n\rangle \tag{A.19}$$

is the LL$n$ exciton energy,

$$V_{n'n} = -\langle X_{n'}|H|X_n\rangle = V^*_{nn'} \tag{A.20}$$

describes the Coulomb–induced coupling of the different LL excitons [112] (see Eq. (2.11)), and $|Y_n\rangle = \hat{Y}^\dagger_n|0\rangle$, where the operator

$$\hat{Y}_n = [\hat{X}_n, H] - \Omega_n\hat{X}_n + \sum_{n'\neq n} V_{nn'}\hat{X}_{n'}, \tag{A.21}$$

describes the interactions between the LL$n$ exciton and the rest of the carriers present in the system. One can see by using the above three equations that $|Y_n\rangle$ is orthogonal to all the magnetoexciton states $|X_m\rangle$, $\langle Y_n|X_m\rangle = 0$, $n, m = 0, 1, \cdots$, and thus corresponds to a 2DEG* state, a state with an excited electron gas configuration. The states $|Y_n\rangle$ describe the $\{1e\text{–}h\text{+}1\text{MP}\}$ four–particle $Y$ excitations with which the $X$ states can scatter, as discussed in Ch. 7.3.

We can now describe the time evolution of the 1–$h$ photo–excited state $|\psi_1\rangle$, which we have split into the excitonic and correlated parts, $P^L_n(t)$ and $|\bar{\psi}_1\rangle$ respectively. The equation of motion for $P^L_n(t)$ can be derived by truncating Eq. (A.11) at first order in the electric field, projecting onto the state $\langle X_n|$, and applying Eq. (A.18):

$$i\frac{\partial}{\partial t}P^L_n(t) = \Omega_n P^L_n(t) - \sum_{n'\neq n} V_{nn'}P^L_{n'}(t) + \bar{P}^L_n(t) - \mu\mathcal{E}(t)N_n^{1/2}. \tag{A.22}$$

The correlation function

$$\bar{P}_n^L(t) = \langle Y_n|\psi_1\rangle = \langle Y_n|\bar{\psi}_1\rangle \tag{A.23}$$

describes the dephasing of $P_n^L(t)$ due to the $X$–2DEG scattering, and is discussed further in Section A.5.

Substituting the decomposition Eq. (A.15) into the Schrödinger equation Eq. (A.11) and using Eqs. (A.22) and (A.18) we obtain the equation of motion of the {1–$h$/2DEG*} contribution $|\bar{\psi}_1\rangle$,

$$i\frac{\partial}{\partial t}|\bar{\psi}_1\rangle - H|\bar{\psi}_1\rangle = \sum_n \left[P_n^L(t)\hat{Y}_n^\dagger - \bar{P}_n^L(t)\hat{X}_n^\dagger\right]|0\rangle = \sum_n \left[P_n^L(t)|Y_n\rangle - \bar{P}_n^L(t)|X_i\rangle\right]. \tag{A.24}$$

The operator $P_n^L(t)\hat{Y}_n^\dagger - \bar{P}_n^L(t)\hat{X}_n^\dagger$ will also appear below, and describes the interaction–assisted photo–excitation of the system.

We can perform a similar analysis on the time evolved 2–$h$ state with the decomposition Eq. (A.16), where the first term on the right hand side is proportional to the non–interacting two magnetoexciton states $|X_n X_{n'}\rangle = \hat{X}_n^\dagger \hat{X}_{n'}^\dagger|0\rangle$, similar to the undoped system [107, 80, 79]. This contribution describes the time evolution of the two magnetoexcitons photo–excited by the optical field in the absence of any interactions. However, the two excitons interact with each other as well as with the 2DEG, as described by the equation

$$\begin{aligned} H|X_n X_m\rangle = (\Omega_n + \Omega_m)|X_n X_m\rangle - \sum_{m'\neq m} V_{m'm}|X_n X_{m'}\rangle - \sum_{n'\neq n} V_{n'n}|X_{n'} X_m\rangle \\ +|X_n Y_m\rangle + |X_m Y_n\rangle + |B_{nm}\rangle, \end{aligned} \tag{A.25}$$

obtained by using Eq. (A.21) to calculate the state $[H, \hat{X}_n^\dagger \hat{X}_m^\dagger]|0\rangle$. The first term in Eq. (A.25) is the energy of the two non–interacting $X$, while the following two terms come from the Coulomb–induced LL coupling. The second line is easy to interpret. Similar to

$|X_n X_m\rangle$, the states $|X_n Y_m\rangle = \hat{X}_n^\dagger \hat{Y}_m^\dagger |0\rangle$ describe an $X_n$ and a $Y_m$ excitation that do not interact with each other. Finally, the last term in Eq. (A.25),

$$|B_{nm}\rangle = [\hat{Y}_n^\dagger, \hat{X}_m^\dagger]|0\rangle = [[H, \hat{X}_n^\dagger], \hat{X}_m^\dagger]|0\rangle, \tag{A.26}$$

comes from $X$–$X$ interactions [48, 49, 47, 80, 30, 17, 6, 107]. This interacting two–exciton state is a linear combination of two $e$-$h$ pairs with different center of mass momenta, with the 2DEG in its ground state. It is therefore orthogonal to all the 2DEG* states, such as $|X_n Y_m\rangle$, and describes the biexciton bound, $X_2$, and scattering, $XX$, states.

In Eq. (A.16), the $X$–$X$ and $X$–2DEG interactions contribute to the time evolution of the photo–excited 2–$h$ state through $|\psi_2^{int}\rangle$, which we further decompose into: (a) the contribution of a non–interacting LL$n$ magnetoexciton with the state $|\bar{\psi}_1\rangle$, and (b) the contribution $|\bar{\psi}_2\rangle$ due to the interactions between all the different pairs of 1–$h$ states. This last term comes from both $X$–$X$ interactions (as found in the undoped system), and $X$ interactions with the {1–$h$/2DEG*} states only present in the doped system (such as the four–particle $Y$ excitations), and therefore describes the correlated contribution to the 2–$h$ state.

To obtain the equations of motion, we note that the time evolved 2–$h$ state $|\psi_2\rangle$ contributes to the optical dynamics at second order in the applied field. By taking the time derivative of Eq. (A.16) and using Eqs. (A.12), (A.25), (A.21), (A.22), and (A.24), we find that the correlated contribution to the 2–$h$ state is determined by

$$i\frac{\partial}{\partial t}|\bar{\psi}_2\rangle - H|\bar{\psi}_2\rangle = \frac{1}{2}\sum_{nm} P_n^L(t) P_m^L(t)|B_{nm}\rangle + \sum_n \left[P_n^L(t)\hat{Y}_n^\dagger - \bar{P}_n^L(t)\hat{X}_n^\dagger\right]|\bar{\psi}_1\rangle. \tag{A.27}$$

Recalling that $|B_{nm}\rangle$, Eq. (A.26), is the interacting two–exciton state, we see that the first term on the right hand side of the above equation describes the $X$–$X$ interaction effects

similar to the undoped case [48, 49, 47, 80, 30, 17, 6, 107]. The second term describes the scattering of the photo–excited LL$n$ magnetoexciton with the carriers in the {1–$h$/2DEG*} state $|\bar{\psi}_1\rangle$.

Finally, we turn to the 0–$h$ state. In Eq. (A.14), we have split this into the contribution of the ground state $|0\rangle$, with amplitude $\langle 0|\psi\rangle = \langle 0|\psi_0\rangle$, and the {0–$h$/2DEG*} contribution $|\psi_0^{int}\rangle$. This 2DEG* contribution is second order in the electric field as well, generated by the two–photon process of excitation and de–excitation of the system by the optical field, accompanied by the scattering of the photo–excited $e$–$h$ pair with the 2DEG. The above state is further decomposed into two parts. The first part, $-\sum_n P_n^{L*}(t)\hat{X}_n|\bar{\psi}_1\rangle$, describes the de–excitation after time $t$ of an LL$n$ magnetoexciton without scattering with the rest of the carriers in the {1–$h$/2DEG*} photo–excited state $|\bar{\psi}_1\rangle$. The latter interactions, as well as the time evolution of the MP state excited via a second–order process analogous to the one that leads to the inelastic Raman scattering signal [92], are described by the second part, $|\bar{\psi}_0\rangle$.

We can introduce the state

$$|M_{nm}\rangle = \hat{X}_n|Y_m\rangle. \tag{A.28}$$

Recalling that $|Y_m\rangle$ is an $X$–MP excitation and $\hat{X}_n$ annihilates an $X$, we see that the state $|M_{nm}\rangle$ is a MP state. The creation of such a MP state is described schematically in Ch. 7.3 (see Fig. 7.3).

As stated above, the correlated part of $|\psi_0\rangle$ contributes to second order in the electric field. By substituting Eq. (A.14) into Eq. (A.10) and using Eqs. (A.21), (A.22), and (A.24), we obtain the equation of motion for the correlated 0–$h$ contribution ($H|0\rangle = 0$

defines the ground state energy as the reference point):

$$i\frac{\partial}{\partial t}|\bar{\psi}_0\rangle - H|\bar{\psi}_0\rangle = \sum_{nm} P_n^{L*}(t)P_m^L(t)|M_{nm}\rangle$$
$$+\sum_n \left[P_n^{L*}(t)\hat{Y}_n - \bar{P}_n^{L*}(t)\hat{X}_n\right]|\bar{\psi}_1\rangle - \sum_n P_n^{L*}(t)\bar{P}_n^L(t)|0\rangle, \tag{A.29}$$

where the last term in Eq. (A.29) simply ensures the orthogonality $\langle 0|\bar{\psi}_0\rangle = 0$, and we neglect any fluctuations in the number of LL$n$ electrons in the ground state ($\Delta\hat{N}_n|0\rangle = 0$ for the magnetic fields of interest).

The second term on the right hand side describes the scattering of the LL$n$ magnetoexciton with the carriers in the $\{1\text{–}h/2\text{DEG}^*\}$ state $|\bar{\psi}_1\rangle$ during the de–excitation at time $t$. The first term in Eq. (A.29) describes the photo–excitation of a MP state via the second–order process where an LL$m$ exciton is photo–excited and scatters with the 2DEG into the four–particle excitation $|Y_m\rangle$, and then the optical field de–excites a LL$n$ exciton with amplitude $P_n^L(t)$, as depicted in Fig. 7.3.

## A.4 Nonlinear Polarization equation of motion

We are now ready to derive the equation of motion of the nonlinear polarization $P_n(t)$. Although the equations can be used to describe any nonlinear optics experiment, we will focus on the FWM case which is of primary interest here when we discuss the physical meaning of the different terms.

By taking the time derivative of Eq. (A.8) and using the definition of the operator $\hat{Y}_n$ in Eq. (A.21) and the commutator Eq. (A.5), we obtain that

$$i\frac{\partial}{\partial t}P_n(t) - \Omega_n P_n(t) + \sum_{n'\neq n} V_{nn'}P_{n'}(t) = -\frac{\mu\mathcal{E}(t)}{\sqrt{N_n}}\left[N_n - \langle\psi|\Delta\hat{N}_n|\psi\rangle\right] + \langle\psi|\hat{Y}_n|\psi\rangle. \tag{A.30}$$

Let us analyze the first term on the right hand side, which describes the Pauli blocking effects. Using the decomposition Eq. (A.15) of $|\psi_1\rangle$ and the properties

$$\Delta\hat{N}_n|0\rangle = 0, \quad \Delta\hat{N}_n|X_m\rangle = 2\delta_{nm}|X_n\rangle, \tag{A.31}$$

deduced from Eqs. (A.6) and (A.4), we obtain to second order in the optical field

$$\langle\psi|\Delta\hat{N}_n|\psi\rangle = \langle\psi_1|\Delta\hat{N}_n|\psi_1\rangle = 2P_n^{L*}(t)P_n^L(t) + \bar{n}_n(t). \tag{A.32}$$

The first term, $2P_n^{L*}(t)P_n^L(t)$, is the familiar coherent exciton density (see Eq. (2.35)), while

$$\bar{n}_n(t) = \langle\bar{\psi}_1|\Delta\hat{N}_n|\bar{\psi}_1\rangle \tag{A.33}$$

is the incoherent density. Recalling the definition of $\Delta\hat{N}_n$, Eq. (A.6), we see that $\bar{n}_n$ describes the average number of photo-excited LL$n$ carriers in the {1-$h$/2DEG*} state $|\bar{\psi}_1\rangle$.

The second term in Eq. (A.30) describes the optical signal generated by the interactions between $X_n$ and the photo–excited or 2DEG carriers. Using the expansion Eq. (A.9) we obtain

$$\langle\psi|\hat{Y}_n|\psi\rangle = \langle\psi_0|\hat{Y}_n|\psi_1\rangle + \langle\psi_1|\hat{Y}_n|\psi_2\rangle + O(\mathcal{E}^5). \tag{A.34}$$

We can separate out the correlated contributions to the interaction–induced signal described by the above expectation value. We start by substituting the decompositions Eqs. (A.14)-(A.16) into Eq. (A.34) and rearranging the terms:

$$\begin{aligned}\langle\psi|\hat{Y}_n|\psi\rangle = \langle\psi|0\rangle\langle 0|\hat{Y}_n|\psi_1\rangle + \sum_m P_m^{L*}(t)\langle X_m|\hat{Y}_n|\psi_2\rangle + \langle\bar{\psi}_0|\hat{Y}_n|\bar{\psi}_1\rangle + \langle\bar{\psi}_1|\hat{Y}_n|\bar{\psi}_2\rangle \\ + \sum_m P_m^L(t)\langle\bar{\psi}_1|[\hat{Y}_n, \hat{X}_m^\dagger]|\bar{\psi}_1\rangle + \sum_m P_m^L(t)\langle\bar{\psi}_0|\hat{Y}_n|X_m\rangle \\ + \sum_{n'm'} P_{n'}^L(t)P_{m'}^L(t)\left[\frac{1}{2}\langle\bar{\psi}_1|\hat{Y}_n\hat{X}_{n'}^\dagger\hat{X}_{m'}^\dagger|0\rangle - \langle\bar{\psi}_1|\hat{X}_{n'}^\dagger\hat{Y}_n\hat{X}_{m'}^\dagger|0\rangle\right].\end{aligned} \tag{A.35}$$

We can simplify the second term on the right hand side of the above equation by using the definition of $|B_{nm}\rangle$, Eq. (A.26),

$$\begin{aligned}\sum_m P_m^{L*}(t)\langle X_m|\hat{Y}_n|\psi_2\rangle &= \sum_m P_m^{L*}(t)\langle Y_n|\hat{X}_m|\psi_2\rangle + \sum_m P_m^{L*}(t)\langle B_{nm}|\psi_2\rangle \\ &= \sum_m P_m^{L*}(t)\langle Y_n|\hat{X}_m|\psi_2\rangle + \sum_{mn'm'} \langle B_{nm}|X_{n'}X_{m'}\rangle P_m^{L*}(t)P_{n'}^{L}(t)P_{m'}^{L}(t) \\ &\quad + \sum_m P_m^{L*}(t)\langle B_{nm}|\bar{\psi}_2\rangle.\end{aligned} \tag{A.36}$$

The second and third terms in Eq. (A.36) describe the mean–field (second term) and higher order (third term) $X$-$X$ correlations. We have also used the fact that $\langle B_{nm}|\hat{X}_{m'}^{\dagger}|\bar{\psi}_1\rangle = 0$ due to the orthogonality between $X$ and any excited 2DEG states. The first term on the right hand side of Eq. (A.36) and the rest of the first line of Eq. (A.35) together make up the correlation function $\bar{P}_n(t)$, the correlated contribution to the dephasing of the nonlinear polarization,

$$\bar{P}_n(t) = \langle\psi_0|0\rangle\langle Y_n|\psi_1\rangle + \sum_m P_m^{L*}(t)\langle Y_n X_m|\psi_2\rangle + \langle\bar{\psi}_0|\hat{Y}_n|\bar{\psi}_1\rangle + \langle\bar{\psi}_1|\hat{Y}_n|\bar{\psi}_2\rangle. \tag{A.37}$$

Note that, by linearizing the above equation, we recover the correlation function $\bar{P}_n^L(t)$, Eq. (A.23), which describes the dephasing of the $X$ amplitude $P_n^L(t)$. Similarly, Eq. (A.37) describe the dephasing of the polarization $P_n(t)$, due to the $X_n \to Y_n$ scattering of the recombining $e$–$h$ pair with the 2DEG during the coherent emission process.

Next we simplify the expression $\langle\bar{\psi}_0|\hat{Y}_n|X_m\rangle$, by substituting the definition of $\hat{Y}_n$ from Eq. (A.21):

$$\langle\bar{\psi}_0|\hat{Y}_n|X_m\rangle = \langle\bar{\psi}_0|\hat{X}_n H|X_m\rangle - \langle\bar{\psi}_0|(H+\Omega_n)\hat{X}_n|X_m\rangle + \sum_{n'} V_{nn'}\langle\bar{\psi}_0|\hat{X}_{n'}|X_m\rangle. \tag{A.38}$$

Recalling the commutator Eq. (A.5), we know that $\hat{X}_n|X_m\rangle = \hat{X}_n\hat{X}_m^{\dagger}|0\rangle \propto |0\rangle$, and since $\langle\bar{\psi}_0|0\rangle = 0$, the last two terms in the above equation vanish, and we are left with only the

first term. After substituting Eq. (A.18), we obtain

$$\langle\bar{\psi}_0|\hat{X}_n H|X_m\rangle = \langle\bar{\psi}_0|\hat{X}_n\Omega_m|X_m\rangle - \sum_{m'\neq m} V_{mm'}\langle\bar{\psi}_0|\hat{X}_n|X_{m'}\rangle + \langle\bar{\psi}_0|\hat{X}_n|Y_m\rangle. \tag{A.39}$$

Again, the first two terms vanish from our orthogonality condition $\langle\bar{\psi}_0|0\rangle = 0$, and recalling the definition of the MP state $|M_{nm}\rangle$, Eq. (A.28), we find

$$\langle\bar{\psi}_0|\hat{Y}_n|X_m\rangle = \langle\bar{\psi}_0|M_{nm}\rangle. \tag{A.40}$$

We can also rewrite the last line of Eq. (A.35). We start by substituting Eq. (A.21) for $\hat{Y}_n$ and using the orthogonality $\langle\bar{\psi}_1|\hat{X}_m\hat{X}^\dagger_{n'}\hat{X}^\dagger_{m'}|0\rangle = 0$, to obtain

$$\langle\bar{\psi}_1|\hat{Y}_n\hat{X}^\dagger_{n'}\hat{X}^\dagger_{m'}|0\rangle = \langle\bar{\psi}_1|\hat{X}_n H|X_{n'}X_{m'}\rangle - \langle\bar{\psi}_1|H\hat{X}_n\hat{X}^\dagger_{n'}\hat{X}^\dagger_{m'}|0\rangle. \tag{A.41}$$

Using Eq. (A.25) to describe the action of the Hamiltonian on the two–exciton state, the definition of the MP state, Eq. (A.28), the above orthogonality relation, and some simple algebra, we find

$$\begin{aligned}\langle\bar{\psi}_1|\hat{Y}_n\hat{X}^\dagger_{n'}\hat{X}^\dagger_{m'}|0\rangle = {} & \langle\bar{\psi}_1|[\hat{X}_n,\hat{X}^\dagger_{n'}]|Y_{m'}\rangle + \langle\bar{\psi}_1|\hat{X}^\dagger_{n'}|M_{nm'}\rangle \\ & +\langle\bar{\psi}_1|[\hat{X}_n,\hat{X}^\dagger_{m'}]|Y_{n'}\rangle + \langle\bar{\psi}_1|\hat{X}^\dagger_{m'}|M_{nn'}\rangle \\ & -\langle\bar{\psi}_1|H[\hat{X}_n,\hat{X}^\dagger_{n'}]|X_{m'}\rangle - \langle\bar{\psi}_1|H\hat{X}^\dagger_{n'}[\hat{X}_n,\hat{X}^\dagger_{m'}]|0\rangle.\end{aligned} \tag{A.42}$$

Replacing the commutators by Eq. (A.5), and using Eqs. (A.18), (A.31), and the orthogonality $\langle\bar{\psi}_1|X_m\rangle = 0$, we obtain

$$\begin{aligned}\langle\bar{\psi}_1|\hat{Y}_n\hat{X}^\dagger_{n'}\hat{X}^\dagger_{m'}|0\rangle = {} & \frac{2\delta_{nn'}\delta_{nm'}}{N_n}\langle\bar{\psi}_1|Y_n\rangle - \frac{\delta_{nn'}}{N_n}\langle\bar{\psi}_1|\Delta\hat{N}_n|Y_{m'}\rangle - \frac{\delta_{nm'}}{N_n}\langle\bar{\psi}_1|\Delta\hat{N}_n|Y_{n'}\rangle \\ & +\langle\bar{\psi}_1|\hat{X}^\dagger_{n'}|M_{nm'}\rangle + \langle\bar{\psi}_1|\hat{X}^\dagger_{m'}|M_{nn'}\rangle.\end{aligned} \tag{A.43}$$

Similar to Eq. (A.40), we also find the relation

$$\langle\bar{\psi}_1|\hat{X}^\dagger_{n'}\hat{Y}_n\hat{X}^\dagger_{m'}|0\rangle = \langle\bar{\psi}_1|\hat{X}^\dagger_{n'}|M_{nm'}\rangle. \tag{A.44}$$

Putting together Eqs. (A.43) and (A.44), we can rewrite the last line of Eq. (A.35) as

$$\sum_{n'm'} P^L_{n'}(t)P^L_{m'}(t)\left[\frac{1}{2}\langle\bar{\psi}_1|\hat{Y}_n\hat{X}^\dagger_{n'}\hat{X}^\dagger_{m'}|0\rangle - \langle\bar{\psi}_1|\hat{X}^\dagger_{n'}\hat{Y}_n\hat{X}^\dagger_{m'}|0\rangle\right] \tag{A.45}$$
$$= \frac{1}{N_n}P^L_n(t)\sum_{n'}P^L_{n'}(t)\langle\bar{\psi}_1|\left[\delta_{nn'} - \Delta\hat{N}_n\right]|Y_{n'}\rangle.$$

Finally, by using Eqs. (A.40), (A.45), and (A.37) in Eq. (A.35), we find:

$$\begin{aligned}\langle\psi|\hat{Y}_n|\psi\rangle = \frac{1}{2}\sum_{mn'm'}\langle B_{nn'}|X_mX_{m'}\rangle P^{L*}_{n'}(t)P^L_m(t)P^L_{m'}(t) + \sum_m P^L_m(t)\langle\bar{\psi}_1|[\hat{Y}_n,\hat{X}^\dagger_m]|\bar{\psi}_1\rangle \\ + \frac{1}{N_n}P^L_n(t)\sum_m P^L_m(t)\langle\bar{\psi}_1|\left[\delta_{nm} - \Delta\hat{N}_n\right]|Y_m\rangle \\ + \sum_m P^{L*}_m(t)\langle B_{nm}|\bar{\psi}_2\rangle + \sum_m P^L_m(t)\langle\bar{\psi}_0|M_{nm}\rangle + \bar{P}_n(t).\end{aligned} \tag{A.46}$$

The first term in Eq. (A.46) describes the familiar mean–field, Hartree–Fock (HF) $X$–$X$ interactions of Ch. 2.5.1, which can also be thought of as interactions between the polarization $P^L_n(t)$ and the coherent density $\sim |P^L_n(t)|^2$ [112]. Recalling the decomposition Eq. (A.15) of the photo–excited 1–$h$ state and the definition of the incoherent density Eq. (A.33), the second term can be thought of as a polarization–incoherent photo–excited density interaction, which is described by the correlation function

$$\mathcal{N}_{nm} = \langle\bar{\psi}_1|[\hat{Y}_n,\hat{X}^\dagger_m]|\bar{\psi}_1\rangle. \tag{A.47}$$

The second line of Eq. (A.46) describes the shake–up of the 2DEG during the exciton recombination that leads to the coherent emission. In particular, the photo–excitation of two non–interacting $X$ is followed by the recombination of one them assisted by the shake–up of a MP excitation. The above process leaves the system in the {1–$h$/2DEG*} state $|Y_m\rangle$, which is then annihilated by the optical field.

The last line of Eq. (A.46) describes the correlation effects of the system. The last term, $\bar{P}(t)$ describes the dephasing of the system as discussed above. The first two

terms describe the correlated second–order processes where the excitation of one $e$–$h$ pair is followed by either the excitation or the de–excitation of a second $e$–$h$ pair. Similar to the undoped case [80, 107], we define the amplitude of the correlated 2–$h$ photo–excited state

$$\mathcal{B}_{nm}(t) = \langle B_{nm}|\bar{\psi}_2\rangle, \tag{A.48}$$

which describes the biexciton and X–X scattering correlations. Similarly, the amplitude of the correlated 0–$h$ photo–excited state,

$$\mathcal{M}_{nm}(t) = \langle M_{nm}|\bar{\psi}_0\rangle, \tag{A.49}$$

describes the MP effects and the $X$–{1–$h$/2DEG*} scattering during the two photon process that excites the 2DEG. The contribution to Eq. (A.46) due to the MP photo–excitation comes from a process similar to coherent antiStokes Raman scattering with phonons, shown schematically in Fig. 7.4, in which: (i) A photo–excited $X$ decays into a $Y$, or {$X$–MP} excitation. (ii) The $e$–$h$ pair in this state recombines leading to the coherent emission, which leaves the system in the MP state $|M_{nm}\rangle$. (iii) This MP propagates in time and then interacts with the second photo–excited $X$ into a new $X$ state, which is subsequently annihilated by the optical field.

We can now write the equation of motion for the third–order polarization:

$$\begin{aligned} i\frac{\partial}{\partial t}P_n(t) = \Omega_n P_n(t) - \sum_{n'\neq n} V_{nn'}P_{n'}(t) + \bar{P}_n(t) + \frac{\mu\mathcal{E}(t)}{\sqrt{N_i}}\left[2P_n^{L*}(t)P_n^L(t) + \bar{n}_n(t)\right] \\ +\frac{1}{2}\sum_{mn'm'}\langle B_{nn'}|X_m X_{m'}\rangle P_m^L(t)P_{m'}^L(t)P_{n'}^{L*}(t) + \sum_m P_m^{L*}(t)\mathcal{B}_{nm}(t) \\ +\frac{1}{N_n}P_n^L(t)\sum_m P_m^L(t)\langle Y_m|\left[\delta_{nm} - \Delta\hat{N}_n\right]|\bar{\psi}_1\rangle^* + \sum_m P_m^L(t)\mathcal{M}_{nm}^*(t) + \sum_m P_m^L(t)\mathcal{N}_{nm}. \end{aligned} \tag{A.50}$$

The last term on the first line describes the Pauli blocking (PB), where in the doped case the density also has the incoherent contribution $\bar{n}_n(t)$, Eq. (A.33). The next line shows

the interaction terms similar to the undoped case [48, 49, 47, 80, 30, 17, 6, 107], describing the X–X interactions at the HF level (first term), and correlations beyond the HF (second term). The terms on the third line, along with the dephasing term $\bar{P}_n(t)$ on the first line, describe the contributions of the 2DEG* correlations and dephasing processes as discussed above.

We now turn to the problem of solving for the 0–$h$ and 2–$h$ correlation functions which enter into the above expression, $\mathcal{M}_{nm}$ and $\mathcal{B}_{nm}$, and understanding the $\bar{P}_n(t)$ contribution to the dephasing of the system.

## A.5 Dephasing and correlation processes

So far we have derived expressions for the 3rd order response of a general 2–band correlated system without any approximations about its nature. To connect with our experiments we need to introduce a basis which describes the correlation effects and dephasing of our system. This will require some simplifying assumptions and approximations about the states of our 2DEG system. The set of basis states will allow us to write the equations of motion for the correlation functions $\mathcal{B}_{nm}(t)$, $\mathcal{M}_{nm}(t)$, and $\bar{P}_n(t)$ that determine the correlation–induced FWM signal.

We will start with $\bar{P}_n^L(t)$, Eq. (A.23), which describes the dephasing of the linear polarization $P_n^L(t)$. The interaction effects in the equation of motion of $\bar{P}_n^L(t)$ are described by the state $H|Y_n\rangle$. This state is a linear combination of the 1–$h$ states into which $Y_n$ can scatter, and we need a basis set that describes the most important contributions to the optical spectra. We must choose a basis from the $\{1\text{–}h/2\text{DEG}^*\}$ states that is made out of

electrons, rather than separate the electronic from the MP states as in the phonon case. A brute force calculation of the nonlinear response of the 2DEG using such an approach must deal with a large number of basis states. To circumvent such difficulties we will use here an orthonormal basis set constructed by using the recursive, or Lanczos method [42, 76]. Such Lanczos bases have been successfully used to calculate Green functions for tight binding and Hubbard Hamiltonians [42], or for describing continuum resonances in the absorption spectrum of semiconductor superlattices [37]. Their advantage is their efficiency, both in speed and in storage space, in problems where brute force matrix diagonalization is impractical. This basis construction will also allow us to derive the generalized average polarization model presented in the text, that captures the dominant correlation and collective time dependent effects.

Similar to Eq. (A.18) that introduced the states $|Y_n\rangle$, we use the recursive method to obtain a new basis state, by acting with the Hamiltonian $H$ on the previous state, and then orthogonalizing the result with respect to the existing basis states [42]. Such an orthogonalization procedure led us to the choice of the parameters $\Omega_n$ and $V_{nn'}$, defined in Eqs. (A.19) and (A.20). A new orthogonal state $|Z_n\rangle = \hat{Z}_n^\dagger|0\rangle$ is now constructed from the relation

$$H|Y_n\rangle = \bar{\Omega}_n|Y_n\rangle + \sum_{n'} W_{n'n}|X_{n'}\rangle + |Z_n\rangle, \tag{A.51}$$

where

$$\bar{\Omega}_n = \frac{\langle Y_n|H|Y_n\rangle}{\langle Y_n|Y_n\rangle} \tag{A.52}$$

is the average energy of the four–particle excitation $|Y_n\rangle$, and

$$W_{n'n} = \langle X_{n'}|H|Y_n\rangle \tag{A.53}$$

gives the probability amplitude that $Y_n$ scatters into $X_{n'}$. We have also introduced the operator

$$\hat{Z}_n = [\hat{Y}_n, H] - \bar{\Omega}_n \hat{Z}_n - \sum_{n'} W_{nn'} \hat{X}_{n'}. \tag{A.54}$$

Using Eqs. (A.51), (A.52), and (A.53), as well as the orthogonality $\langle X_{n'}|Y_n\rangle = 0$, one can see that the state $|Z_n\rangle$ is orthogonal to all the states $|X_n\rangle$, $m = 0, 1, \cdots$, and to $|Y_n\rangle$. Therefore, it is a linear combination of all the 2DEG* states into which $|Y_n\rangle$ can scatter.

By using Eq. (A.18) and the orthogonality $\langle X_{n'}|Y_n\rangle = 0$ we obtain the useful relation

$$W_{n'n} = \langle Y_{n'}|Y_n\rangle = W^*_{nn'}. \tag{A.55}$$

Note that $\langle Y_{n'}|Y_n\rangle \neq 0$, and we may also have that $\langle Y_{n'}|Z_n\rangle \neq 0$ for $n' \neq n$. If this is the case we also need to orthogonalize the independent states $|Y_{n'}\rangle$, and then subtract a linear combination of the latter from $|Z_n\rangle$ in Eq. (A.51), so that all the $Z$ and $Y$ states are orthogonal. However, as we shall see in Appendix B, for the 2DEG system in the limit of electron–hole symmetry $|Y_n\rangle$ is the same state for all $n$ when only LL0 and LL1 contribute, and thus the above procedure is not needed.

By multiplying Eq. (A.24) by $\langle Y_n|$ and using Eqs. (A.51), (A.52), and (A.53), we obtain the equation of motion for $\bar{P}^L_n(t)$:

$$i\frac{\partial}{\partial t}\bar{P}^L_n(t) = \bar{\Omega}_n \bar{P}^L_n(t) + \sum_{n'} W_{nn'} P^L_{n'}(t) + \mathcal{Z}^L_n(t). \tag{A.56}$$

We introduced the correlation function $\mathcal{Z}^L_n(t) = \langle Z_n|\bar{\psi}_1\rangle$ that describes the dephasing of $\bar{P}^L_n(t)$ and screening effects. To calculate $\mathcal{Z}^L_n$, we should continue the above recursive procedure by writing the state $H|Z_n\rangle$. The hierarchy of these basis states can be truncated when convergence is reached, after generating a number of states equal to the dimension of

a finite system, or by using the time dependent variational principle in the spirit of large N mean–field theories [16].

Using the recursive method we can also construct a basis for the 2–$h$ and 0–$h$ states, which we use to calculate the correlation functions $\mathcal{B}_{nm}$ and $\mathcal{M}_{nm}$. The equation of motion for $\mathcal{B}_{nm}$ depends on the state $H|B_{nm}\rangle$,

$$H|B_{nm}\rangle = \Omega^B_{nm}|B_{nm}\rangle + |\bar{B}_{nm}\rangle, \quad \Omega^B_{nm} = \frac{\langle B_{nm}|H|B_{nm}\rangle}{\langle B_{nm}|B_{nm}\rangle}, \tag{A.57}$$

where $\Omega^B_{nm}$ is the average energy of the interacting 2–$X$ state, and the state $|\bar{B}_{nm}\rangle$, where $\langle\bar{B}_{nm}|B_{nm}\rangle = 0$, is a linear combination of all the 2–$X$ states into which $|B_{nm}\rangle$ can scatter. Using Eqs. (A.57) and (A.27), and noting that, since the state $\langle B_{nm}|$ has the 2DEG is in its ground state, $\langle B_{nm}|\hat{X}^\dagger_{n'}|\bar{\psi}_1\rangle = 0$, we take the time derivative of Eq. (A.26) and find the equation of motion

$$i\frac{\partial}{\partial t}\mathcal{B}_{nm} - \Omega^B_{nm}\mathcal{B}_{nm} = \frac{1}{2}\sum_{n'm'}\langle B_{nm}|B_{n'm'}\rangle P^L_{n'}(t)P^L_{m'}(t) + \sum_{n'} P^L_{n'}(t)\langle B_{nm}|\hat{Y}^\dagger_{n'}|\bar{\psi}_1\rangle + \bar{\mathcal{B}}_{nm}, \tag{A.58}$$

where we introduced the correlation function $\bar{\mathcal{B}}_{nm} = \langle\bar{\mathcal{B}}_{nm}|\bar{\psi}_2\rangle$. One should note here the similarity between Eq. (A.58) and Eq. (2.39), from the average polarization model discussed in Ch. 2.5.2 that has been successful in describing the $X$–$X$ correlations and biexciton effects in undoped semiconductors [21, 107]. In fact, the Lanczos method provides the derivation of that model as well. Eq. (A.58) describes the time evolution of the "intermediate" interacting 2–$X$ state $|B_{nm}\rangle$, which is created by the $X$–$X$ interactions (first term on the right hand side of Eq. (A.58), same as in the undoped case) and the $X$–{1–$h$/2DEG*} interactions (second term on the right hand side of Eq. (A.58)). The last term in Eq. (A.58) describes the dephasing of $\mathcal{B}_{nm}$.

Just as $\mathcal{B}_{nm}$ describes the 2–$h$ correlated state, the correlation function $\mathcal{M}_{nm}$ describes the time evolution of the "intermediate" photo–excited MP state $|M_{nm}\rangle$. Using the Lanczos method we obtain that

$$H|M_{nm}\rangle = \Omega^M_{nm}|M_{nm}\rangle + |\bar{M}_{nm}\rangle, \quad \Omega^M_{nm} = \frac{\langle M_{nm}|H|M_{nm}\rangle}{\langle M_{nm}|M_{nm}\rangle}, \tag{A.59}$$

where $\Omega^M_{nm}$ is the average MP energy, and the state $|\bar{M}_{nm}\rangle$, with $\langle \bar{M}_{nm}|M_{nm}\rangle = 0$, describes the dephasing of $\mathcal{M}_{nm}$, mainly due to the MP decay into incoherent particle–hole excitations or electron–phonon scattering. Noting that the MP collective excitations are long lived for small momenta, we describe such dephasing here by introducing the energy width $\gamma_M$. Projecting the state $\langle M_{nm}|$ on Eq. (A.29) and using Eq. (A.59), we find

$$\begin{aligned} i\frac{\partial}{\partial t}\mathcal{M}_{nm} = (\Omega^M_{nm} - i\gamma_M)\mathcal{M}_{nm} + \sum_{n'm'} \langle M_{nm}|M_{n'm'}\rangle P^{L*}_{n'}(t)P^L_{m'}(t) \\ + \sum_{n'} \langle M_{nm}| \left[P^{L*}_{n'}(t)\hat{Y}_{n'} - \bar{P}^{L*}_{n'}(t)\hat{X}_{n'}\right] |\bar{\psi}_1\rangle. \end{aligned} \tag{A.60}$$

The remaining step is the calculation of the correlation function $\bar{P}_i$, Eq. (A.37), which describes the dephasing of $P_n$ as well as correlation effects that cannot be factorized. The equation of motion is tedious but straightforward to derive, similar to the above equations of motion:

$$\begin{aligned} i\frac{\partial}{\partial t}\bar{P}_n(t) - \bar{\Omega}_n\bar{P}_n(t) - \mathcal{Z}_n = \mu\mathcal{E}(t)\sum_m \left[\frac{1}{\sqrt{N_m}}P^{L*}_m(t)\langle Y_n|\Delta\hat{N}_m|\bar{\psi}_1\rangle - \sqrt{N_m}\,\mathcal{M}_{mn}(t)\right] \\ + \sum_m W_{nm}P_m(t) + \sum_{mn'} \frac{1}{N_{n'}}P^L_m(t)\langle Y_n| \left[\delta_{mn'} - \Delta\hat{N}_{n'}\right] |Y_m\rangle P^{L*}_{n'}(t)P^L_{n'}(t) \\ + \sum_{mn'm'} \langle M_{mn}|M_{n'm'}\rangle P^{L*}_{n'}(t)P^L_m(t)P^L_{m'}(t) \\ + \sum_m P^L_m(t)\langle\bar{\psi}_1| \left[[\hat{Y}_n, \hat{Y}^\dagger_m] - \sum_{n'} W_{nn'}[\hat{X}_{n'}, \hat{X}^\dagger_m]\right] |\bar{\psi}_1\rangle \\ - \sum_m \bar{P}^L_m(t)\langle\bar{\psi}_1|[\hat{Y}_n, \hat{X}^\dagger_m]|\bar{\psi}_1\rangle + \frac{1}{2}\sum_{mm'} P^L_m(t)P^L_{m'}(t)\langle\bar{\psi}_1|\hat{Y}_n|B_{mm'}\rangle \end{aligned} \tag{A.61}$$

$$+\sum_m \frac{1}{N_m}\bar{P}_m^{L*}(t)P_m^L(t)\langle Y_n|\Delta\hat{N}_m|\bar{\psi}_1\rangle - \sum_{mn'}\bar{P}_{n'}^{L*}(t)P_m^L(t)\langle M_{mn}|\hat{X}_{n'}^\dagger|\bar{\psi}_1\rangle$$
$$-\sum_{mm'}P_m^{L*}(t)P_{m'}^L(t)\langle M_{m'm}|\hat{Y}_n|\bar{\psi}_1\rangle + \sum_{mm'}P_m^{L*}(t)P_{m'}^L(t)\langle Y_n|\hat{Y}_m\hat{X}_{m'}^\dagger|\bar{\psi}_1\rangle$$
$$+\sum_m \bar{P}_m^{L*}(t)\mathcal{B}_{nm} - \sum_m \bar{P}_m^L(t)\mathcal{M}_{mn}^* + \sum_m\left[P_m^L(t)\langle\bar{\psi}_0|\hat{Y}_n|Y_m\rangle - P_m^{L*}(t)\langle 0|[\hat{Y}_m,\hat{Y}_n]|\bar{\psi}_2\rangle\right]$$

where we have introduced the correlation function

$$\mathcal{Z}_n = \langle\psi|0\rangle\langle Z_n|\psi_1\rangle + \sum_m P_m^{L*}(t)\langle Z_n|\hat{X}_m|\psi_2\rangle + \langle\bar{\psi}_0|\hat{Z}_n|\bar{\psi}_1\rangle + \langle\bar{\psi}_1|\hat{Z}_n|\bar{\psi}_2\rangle. \tag{A.62}$$

The first line on the right hand side of Eq. (A.61) describes Pauli blocking effects, while the first term on the second line describes the scattering of the $Y$ four–particle excitation into $X$ states. This term is the only one that contributes to the linearized Eq. (A.56). The next two terms may be thought of as describing, to lowest order in the optical field, the excitation–induced corrections to the above scattering amplitude $W_{nn'}$ that are proportional to the coherent density. The fourth line describes analogous corrections proportional to the incoherent density. The last line of Eq. (A.61) describes the effects of the time evolution of the intermediate MP and $X$–$X$ interacting states. $\mathcal{Z}_n(t)$ describes the dephasing of $\bar{P}_n(t)$ and, to first order in the optical field, coincides with $\mathcal{Z}_n^L(t)$ in Eq. (A.56). Its equation of motion has a form analogous to that of $\bar{P}_n(t)$, and may be obtained after expressing the states $H|Z_n\rangle$ with the recursive method. Finally, the remaining terms on the right hand side of Eq. (A.61) describe, to the lowest order in the optical field, the excitation–induced dephasing of $\bar{P}_n(t)$.

# Appendix B

# Symmetry arguments

In this appendix we derive some useful expressions for the operators $\hat{Y}_n$, most notably the symmetry relation Eq. (7.16) for the two LL model in the symmetric limit. These properties are determined by the commutator $[X_n, H_{int}]$, where the Hamiltonian $H_{int} = V_{ee} + V_{hh} + V_{eh}$ describes the Coulomb interactions. In the particle–hole symmetric limit we have that

$$H_{int} = \frac{1}{2}\int d\mathbf{r}d\mathbf{r}'\ v(\mathbf{r}-\mathbf{r}')\ \left[\psi^\dagger(\mathbf{r})\psi(\mathbf{r}) - \bar{\psi}^\dagger(\mathbf{r})\bar{\psi}(\mathbf{r})\right]\left[\psi^\dagger(\mathbf{r}')\psi(\mathbf{r}') - \bar{\psi}^\dagger(\mathbf{r}')\bar{\psi}(\mathbf{r}')\right], \qquad \text{(B.1)}$$

where $\psi^\dagger(\mathbf{r})$ is the electron creation operator, $\bar{\psi}^\dagger(\mathbf{r})$ is the hole creation operator, and $v(\mathbf{r})$ is the Coulomb potential. To describe the magnetic field effects, we choose to work in the Landau gauge $\mathbf{A} = (0, Bx, 0)$. The eigenstates of the kinetic energy operator are then characterized by the $y$–component of the momentum, $k$. The electron, $\psi_{kn}$, and hole, $\bar{\psi}_{kn}$, eigenstates of the kinetic energy operator in this gauge are [45, 107]

$$\psi_\alpha(\mathbf{r}) = \frac{e^{iky}}{\sqrt{L}}\psi_n(x - x_k), \quad \bar{\psi}_{kn}(\mathbf{r}) = \psi^*_{-kn}(\mathbf{r}), \qquad \text{(B.2)}$$

where $\alpha = (k, n)$, $x_k = -kl_c^2$ is the x coordinate of the cyclotron orbit center, $l_c = \sqrt{\hbar c/eB}$ is the magnetic length, $\psi_n(x - x_k)$ are the eigenstates of the one–dimensional harmonic oscillator with frequency equal to the cyclotron frequency, and $L$ is the system size. By expanding the electron and hole creation operators in the Landau basis we transform the Hamiltonian Eq. (B.1) in the familiar form

$$H_{int} = \frac{1}{2} \sum_{\alpha_1\alpha_2\alpha_3\alpha_4} \Big[ v^{ee}_{\alpha_1\alpha_2,\alpha_3\alpha_4} \hat{e}^\dagger_{\alpha_3} \hat{e}^\dagger_{\alpha_1} \hat{e}_{\alpha_2} \hat{e}_{\alpha_4} + v^{hh}_{\alpha_1\alpha_2,\alpha_3\alpha_4} \hat{h}^\dagger_{\alpha_3} \hat{h}^\dagger_{\alpha_1} \hat{h}_{\alpha_2} \hat{h}_{\alpha_4}$$
$$- v^{eh}_{\alpha_1\alpha_2,\alpha_3\alpha_4} \hat{h}^\dagger_{\alpha_3} \hat{e}^\dagger_{\alpha_1} \hat{e}_{\alpha_2} \hat{h}_{\alpha_4} - v^{he}_{\alpha_1\alpha_2,\alpha_3\alpha_4} \hat{e}^\dagger_{\alpha_3} \hat{h}^\dagger_{\alpha_1} \hat{h}_{\alpha_2} \hat{e}_{\alpha_4}, \tag{B.3}$$

where the Coulomb interaction matrix elements $v^{ij}_{\alpha_1\alpha_2,\alpha_3\alpha_4}$ (with $i, j = e, h$) are given by

$$v^{ij}_{\alpha_1\alpha_2,\alpha_3\alpha_4} = \int \frac{d\mathbf{q}}{(2\pi)^2} v_q F^i_{\alpha_1\alpha_2}(\mathbf{q}) F^j_{\alpha_3\alpha_4}(-\mathbf{q}), \tag{B.4}$$

where $v_q = 2\pi e^2/q$ and

$$F^e_{\alpha_1\alpha_2}(\mathbf{q}) = \int d\mathbf{r} \psi^*_{\alpha_1}(\mathbf{r}) e^{i\mathbf{q}\cdot\mathbf{r}} \psi_{\alpha_2}(\mathbf{r}) \ , \ F^h_{\alpha_1\alpha_2}(\mathbf{q}) = \int d\mathbf{r} \bar{\psi}^*_{\alpha_1}(\mathbf{r}) e^{i\mathbf{q}\cdot\mathbf{r}} \bar{\psi}_{\alpha_2}(\mathbf{r}). \tag{B.5}$$

Following Ref. [65] we obtain that

$$F^e_{\alpha_1\alpha_2}(\mathbf{q}) = \varphi_{n_1 n_2}(\mathbf{q}) f_{k_1 k_2}(\mathbf{q}), \tag{B.6}$$

where

$$f_{k_1 k_2}(\mathbf{q}) = e^{-iq_x(k_1+k_2)l^2/2} \delta_{k_1, k_2+q_y} = f^*_{k_2 k_1}(-\mathbf{q}) = f_{-k_1,-k_2}(-\mathbf{q}) \tag{B.7}$$

and, for $m \geq n$, we have that

$$\varphi_{mn}(\mathbf{q}) = \frac{n!}{m!} \left[ \frac{(q_y + iq_x)l}{\sqrt{2}} \right]^{m-n} L_n^{m-n} \left( \frac{q^2 l^2}{2} \right) e^{-q^2 l^2/4}, \tag{B.8}$$

where $L_n^{m-n}$ is the generalized Laguerre polynomial. $\varphi_{mn}(\mathbf{q})$ for $m < n$ can be obtained by using the property

$$\varphi_{mn}(\mathbf{q}) = \varphi^*_{nm}(-\mathbf{q}). \tag{B.9}$$

Using Eq. (B.2) we obtain from Eq. (B.5)

$$F^h_{\alpha_1\alpha_2}(\mathbf{q}) = F^e_{-\alpha_2,-\alpha_1}(\mathbf{q}) = \varphi_{n_2n_1}(\mathbf{q}) f_{-k_2-k_1}(\mathbf{q}) = \varphi_{n_2n_1}(\mathbf{q}) f^*_{k_1k_2}(\mathbf{q}), \tag{B.10}$$

where we denote $-\alpha = (-k, n)$. Using the symmetry property

$$v^{ij}_{\alpha_1\alpha_2,\alpha_3\alpha_4} = v^{ji}_{\alpha_3\alpha_4,\alpha_1\alpha_2} \tag{B.11}$$

we obtain that

$$\begin{aligned}[\hat{h}_{-\alpha}\hat{e}_\alpha, H_{int}] = \sum_{\alpha_1\alpha_2\alpha_3} \Big[ & v^{ee}_{\alpha_1\alpha_2,\alpha\alpha_3} \hat{e}^\dagger_{\alpha_1}\hat{e}_{\alpha_2}\hat{h}_{-\alpha}\hat{e}_{\alpha_3} - v^{eh}_{\alpha_1\alpha_2,-\alpha-\alpha_3}\hat{e}^\dagger_{\alpha_1}\hat{e}_{\alpha_2}\hat{h}_{-\alpha_3}\hat{e}_\alpha \\ + v^{hh}_{-\alpha-\alpha_3,\alpha_1\alpha_2}\hat{h}^\dagger_{\alpha_1}\hat{h}_{\alpha_2}\hat{h}_{-\alpha_3}\hat{e}_\alpha - & v^{eh}_{\alpha\alpha_3,\alpha_1\alpha_2}\hat{h}^\dagger_{\alpha_1}\hat{h}_{\alpha_2}\hat{h}_{-\alpha}\hat{e}_{\alpha_3}\Big] - \sum_{\alpha_1\alpha_2} v^{eh}_{\alpha\alpha_2,-\alpha-\alpha_1}\hat{h}_{-\alpha_1}\hat{e}_{\alpha_2}. \end{aligned} \tag{B.12}$$

Using the symmetry properties Eq. (B.11) and

$$v^{eh}_{\alpha_1\alpha_2,-\alpha-\alpha_3} = v^{ee}_{\alpha_1\alpha_2,\alpha_3\alpha}, \quad v^{hh}_{-\alpha-\alpha_3,\alpha_1\alpha_2} = v^{ee}_{\alpha_3\alpha,-\alpha_2-\alpha_1}, \tag{B.13}$$

obtained from Eqs. (B.4) and (B.10), we obtain after some algebra that

$$\begin{aligned}[\hat{h}_{-\alpha}\hat{e}_\alpha, H_{int}] = & -\sum_{\alpha_1\alpha_2} v^{ee}_{\alpha\alpha_2,\alpha_1\alpha}\hat{h}_{-\alpha_1}\hat{e}_{\alpha_2} \\ + \sum_{\alpha_1\alpha_2\alpha'} \Big[ & v^{ee}_{\alpha_1\alpha_2,\alpha\alpha'}\Big(\hat{e}^\dagger_{\alpha_1}\hat{e}_{\alpha_2} - \hat{h}^\dagger_{-\alpha_2}\hat{h}_{-\alpha_1}\Big)\hat{h}_{-\alpha}\hat{e}_{\alpha'} - (\alpha \leftrightarrow \alpha')\Big]. \end{aligned} \tag{B.14}$$

After summing over $k$, the left hand side of Eq. (B.14) becomes the commutator $[\hat{X}_n, H_{int}]$ that determines the operator $\hat{Y}_n$. Using the property

$$\sum_k f_{kk_2}(\mathbf{q}) f_{k_1k}(-\mathbf{q}) = \delta_{k_1k_2} \tag{B.15}$$

and noting that, due to the parity properties of $\varphi_{nm}(\mathbf{q})$ under the transformation $\mathbf{q} \to -\mathbf{q}$, we have that

$$\int d\mathbf{q}\, v(q)\varphi_{nn_2}(\mathbf{q})\varphi^*_{nn_1}(\mathbf{q}) = \delta_{n_1,n_2}\int d\mathbf{q}\, v(q)\,|\varphi_{nn_1}(\mathbf{q})|^2, \tag{B.16}$$

we transform the first term on the right hand side of Eq. (B.14) into the form $\sum_{n'} V^0_{nn'} X_{n'}$, where

$$V^0_{nn'} = \int \frac{d\mathbf{q}}{(2\pi)^2}\, v_q\, |\varphi_{nn'}(q)|^2. \tag{B.17}$$

The above expression gives the Coulomb–induced LL coupling in the undoped case [112]. Using the above relations we obtain that

$$[\hat{X}_n, H_{int}] = -\sum_{n'} V^0_{nn'} \hat{X}_{n'}$$
$$+ \sum_{\alpha_1\alpha_2} \left(\hat{e}^\dagger_{\alpha_1}\hat{e}_{\alpha_2} - \hat{h}^\dagger_{-\alpha_2}\hat{h}_{-\alpha_1}\right) \sum_{kk'n'} \left[v^{ee}_{\alpha_1\alpha_2,knk'n'}\hat{h}_{-kn}\hat{e}_{k'n'} - v^{ee}_{\alpha_1\alpha_2,kn'k'n}\hat{h}_{-kn'}\hat{e}_{k'n}\right]. \tag{B.18}$$

Note that the last term in the above equation vanishes for $n' = n$.

Let us now restrict to the first two LL's, which dominate the optical spectra for the magnetic fields and excitation conditions of interest. Recalling Eq. (7.10) we see that the operator $\hat{Y}_n$ is determined by the last term on the right hand side of the above equation. The only contribution to this term comes from $n' \neq n$, and therefore $n'$=1 if $n$=0, or $n'$=0 if $n$=1. Noting that, except for a minus sign, the right hand side of Eq. (B.18) is then the same for $n = 0$ and $n = 1$, we obtain the property $\hat{Y}_1 = -\hat{Y}_0 = \hat{Y}$, Eq. (7.16). The explicit expressions for the four–particle excitation $\langle Y|$ can be obtained from Eq. (B.18) by acting on the ground state $\langle 0|$. Noting that there are no holes or LL1 electrons in the ground state, we obtain from Eq. (B.18) that

$$\langle 0|[\hat{X}_1, H_{int}] = -\sum_{n'} V^0_{1n'} \langle X_{n'}|$$
$$+ \sum_{pp'kk'n'} \langle 0| \left[v^{ee}_{p0p'n',k1k'0}\hat{e}^\dagger_{p0}\hat{e}_{p'n'}\hat{h}_{-k1}\hat{e}_{k'0} - v^{ee}_{p0p'n',k0k'1}\,\hat{e}^\dagger_{p0}\hat{e}_{p'n'}\hat{h}_{-k0}\hat{e}_{k'1}\right]. \tag{B.19}$$

$\hat{Y}_1$ is then obtained by subtracting the $X$ contributions (see Eq. (7.10)). As can be seen from this equation, the four–particle excitation $Y$ consists of an $e$–$h$ pair plus a 2DEG excitation.

# Appendix C

# Derivation of the generalized average polarization model

In this appendix we will discuss the simplifications of the equations of motion derived above which allow us to write the average polarization model presented in the text and used to simulate our experiments. In Section C.1 we we will derive several useful relations, based on the symmetry relation $\hat{Y}_1 = -\hat{Y}_0 = \hat{Y}$, Eq. (7.16), and our truncation of the Lanczos basis described in Appendix A. In Section C.2 we will discuss the simplification of the $X$–$X$ interaction source terms described by $\langle B_{nm}|\psi_2\rangle$. Finally, in Section C.3, we discuss some additional approximations, and put everything together to arrive at the model equations presented in Ch. 7.4.

## C.1 Some useful relations

Starting from our symmetry argument, we immediately find that

$$\bar{\Omega} = \bar{\Omega}_1 = \bar{\Omega}_0 = \frac{\langle Y|H|Y\rangle}{\langle Y|Y\rangle}, \tag{C.1}$$

is the energy of the state $|Y\rangle$, and

$$W_{nn'} = \langle X_n|H|Y_{n'}\rangle = \langle Y_n|Y_{n'}\rangle, \quad W_{00} = W_{11} = -W_{01} = -W_{10} = W > 0 \tag{C.2}$$

simplifies to a single parameter which describes the scattering between $X$ and $Y$ states. Another immediate consequence of Eq. (7.16) is that $\bar{P}_1^L(t) = \langle Y_1|\bar{\psi}_1\rangle = -\langle Y_0|\bar{\psi}_1\rangle = -\bar{P}_0^L(t) = \bar{P}^L(t)$ for the dephasing of the linear polarization, and similarly for $\bar{P}_1(t)$,

$$\begin{aligned}
\bar{P}_1(t) &= \langle\psi_0|0\rangle\langle Y_1|\psi_1\rangle + \sum_m P_m^{L*}(t)\langle Y_1 X_m|\psi_2\rangle + \langle\bar{\psi}_0|\hat{Y}_1|\bar{\psi}_1\rangle + \langle\bar{\psi}_1|\hat{Y}_1|\bar{\psi}_2\rangle \\
&= -\langle\psi_0|0\rangle\langle Y|\psi_1\rangle - \sum_m P_m^{L*}(t)\langle Y X_m|\psi_2\rangle - \langle\bar{\psi}_0|\hat{Y}|\bar{\psi}_1\rangle - \langle\bar{\psi}_1|\hat{Y}|\bar{\psi}_2\rangle \\
&= -\bar{P}_0(t) = \bar{P}(t).
\end{aligned} \tag{C.3}$$

In addition, we notice from the discussion at the end of Appendix B that the $Y$ excitation is an $e$–$h$ pair in different LLs plus a 2DEG excitation. Since we are including only the lowest two levels in the model, we have either {1–LL0–$e$ + 1–LL1–$h$ + 1MP}, or {1–LL1–$e$ + 1–LL0–$h$ + 1MP}. The first case has an energy $\sim \Omega_1$, nearly resonant with LL1, while the second has an energy $\sim \Omega_1 + \Omega_M$, not resonant at all. We therefore neglect the second state and approximate $Y$ as the first state only, which leads to some additional simplifications, such as

$$\Delta\hat{N}_n|Y\rangle = 2\delta_{n,1}|Y\rangle \tag{C.4}$$

for the action of the number operator, and

$$|M_{n,1}\rangle = \delta_{n,0}|M\rangle = -|M_{n,0}\rangle, \quad |M\rangle = \hat{X}_0|Y\rangle \tag{C.5}$$

for the MP states $|M_{nm}\rangle$. The energy $\bar{\Omega} \sim \Omega_0 + \Omega_M \sim \Omega_1$ as well, as a consequence of this approximation.

In order to obtain a closed set of equations for our model, in addition to limiting the number of LLs in the calculations, we must also limit the number of basis states involved. In Appendix A.5, we introduced the Lanczos orthogonalization method, in which we can generate a series of basis states to describe the state $|\psi_1\rangle$, $\hat{X} \to \hat{Y} \to \hat{Z} \to \cdots$. Let us examine the correlation function $\bar{P}^L(t)$, whose dephasing is described by $\mathcal{Z}^L(t)$ in Eq. (A.56). Using the orthogonality relations $\langle X_n|H|Z\rangle = 0$ and $\langle X_n|Y\rangle = \langle Y|Z\rangle = 0$, we see that the equation of motion of $\mathcal{Z}^L(t)$ (and all higher correlation functions) does not couple directly to $P_n^L(t)$. The coupling between $\mathcal{Z}^L(t)$ and $\bar{P}^L(t)$ due to the $Y \to Z$ scattering gives the Coulomb–induced dephasing of $\bar{P}^L(t)$, as well as screening effects. For simplicity here we characterize the dephasing by a phenomenological rate $\gamma$, in analogy with the average polarization treatment of the X–X scattering processes in the undoped case, Ref. [21], or the treatment of electron–phonon scattering Refs. [7, 9] (in the latter work the CM momentum was included). This approximation corresponds to neglecting the basis states $|Z\rangle$ or higher. Then, using Eq. (A.55) we find

$$|\bar{\psi}_1\rangle = \frac{\bar{P}^L(t)}{W}|Y\rangle + \frac{\mathcal{Z}^L(t)}{\langle Z|Z\rangle}|Z\rangle + \cdots \approx \frac{\bar{P}^L(t)}{W}|Y\rangle. \tag{C.6}$$

This is a rather big approximation, which becomes more accurate as $\gamma$ increases. We are truncating the Lanczos basis at the state $|Y\rangle$, and treating the error this causes with a

phenomenological dephasing rate $\gamma$. However, this simplification will allow us to estimate the incoherent contributions to the nonlinear polarization. For example, substituting Eq. (C.6) into Eqs. (A.33) and (A.47) we obtain

$$\bar{n}_n(t) = \frac{\langle Y|\Delta\hat{N}_n|Y\rangle}{\langle Y|Y\rangle}\,\frac{\bar{P}^L(t)\bar{P}^{L*}(t)}{W} = 2\delta_{n,1}\,\frac{\bar{P}^L(t)\bar{P}^{L*}(t)}{W} \tag{C.7}$$

and

$$\mathcal{N}_{1n'}(t) = \frac{\langle Y|[\hat{Y},\hat{X}^\dagger_{n'}]|Y\rangle}{\langle Y|Y\rangle}\,\frac{\bar{P}^L(t)\bar{P}^{L*}(t)}{W} = V^{XY}_{n'}\,\frac{\bar{P}^L(t)\bar{P}^{L*}(t)}{W} = -\mathcal{N}_{0n'}(t). \tag{C.8}$$

Using Eqs. (7.16) and (A.21) and the orthogonality $\langle YX_0|X_1Y\rangle = 0$ we obtain the mean–field interaction between the $X_{n'}$ and the Y excitations, $V^{XY}_{n'}$,

$$V^{XY}_1 = \frac{\langle Y|\hat{Y}|X_1Y\rangle}{\langle Y|Y\rangle} = \frac{\langle YX_1|(H-\bar{\Omega}-\Omega_1)|X_1Y\rangle}{\langle Y|Y\rangle}\,, \tag{C.9}$$
$$V^{XY}_0 = -\frac{\langle YX_0|(H-\bar{\Omega}-\Omega_0)|X_0Y\rangle}{\langle Y|Y\rangle} < 0.$$

Long–lived MP states were observed in the inelastic Raman scattering spectra [92], we thus expect that the time evolution of MP intermediate states, described by the single correlation function $\mathcal{M}(t)$, plays an important role. Such states contribute to the nonlinear optical spectra only due to the electron-hole asymmetry, and disorder [92, 20, 70]. Eq. (C.5) shows that there is now only a single correlation function necessary to describe the MP time dependence, $\mathcal{M}(t) = \mathcal{M}_{\prime\infty}(t) = -\mathcal{M}_{\prime\prime}(t)$, with an energy $\Omega^M_{nm} = \delta n, 0\Omega_M$. The driving terms in the equation of motion, Eq. (A.60, are determined by the matrix elements $W_M = \langle M|M\rangle$, which is a measure of the electron–hole asymmetry of the system, and $\langle M|\hat{Y}|Y\rangle = W_M(\Omega_M+\Omega_0-\bar{\Omega})$, obtained from Eqs. (A.21), (7.16), (A.28), the orthogonalities $\langle 0|\mathcal{M}\rangle = 0$ and $\langle\mathcal{M}|\hat{X}_1|Y\rangle \sim 0$, and neglecting the contribution of the $|Z\rangle$.

## C.2 Exciton-exciton interactions in the APM

In this Appendix we discuss the inclusion of the $X$–$X$ interactions in our model. Such effects have been studied for undoped QW's in a magnetic field for LL0 excitation [107, 23, 123]. For simplicity we treat here the $X$–$X$ interactions at the mean–field, Hartree–Fock (HF) level.

Recalling the definition Eq. (A.26) of the interacting state $\langle B_{n'm'}|$ we obtain from Eq. (B.18)

$$\langle B_{1m'}| = \frac{1}{\sqrt{N_{m'}}} \sum_{pp'n'} \sum_{kk'} \Big[ v^{ee}_{pm'p'n',k1k'0} \langle 0|\hat{h}_{-pm'} \hat{e}_{p'n'} \hat{h}_{-k1} \hat{e}_{k'0}$$
$$- v^{ee}_{pn'p'm',k1k'0} \langle 0|\hat{h}_{-pn'} \hat{e}_{p'm'} \hat{h}_{-k1} \hat{e}_{k'0} - v^{ee}_{pm'p'n',k0k'1} \langle 0|\hat{h}_{-pm'} \hat{e}_{p'n'} \hat{h}_{-k0} \hat{e}_{k'1}$$
$$+ v^{ee}_{pn'p'm',k0k'1} \langle 0|\hat{h}_{-pn'} \hat{e}_{p'm'} \hat{h}_{-k0} \hat{e}_{k'1} \Big], \qquad \text{(C.10)}$$

where the nonzero contribution to the above state comes from $n' \neq m'$. The HF $X$–$X$ interactions are described by the overlap of the above state $\langle B_{1m'}$ with the two–exciton state $|X_n X_m\rangle$. The latter state consists of two electrons in LLs $n$ and $m$, and two holes also in LLs $n$ and $m$. Noting that, as can be seen from the above expression, the state $\langle B_{1m'}$ has at least one electron and hole in different LL's, we see that the only nonzero contribution to the the HF $X$–$X$ interaction comes from $m \neq n$, and therefore $m = 0, n = 1$, or $m = 1, n = 0$. The HF $X$–$X$ interaction contribution to the nonlinear polarization equation of motion thus takes the form

$$\frac{1}{2} \sum_{mm'n'} \langle B_{nn'}|X_m X_{m'}\rangle P^L_m(t) P^L_{m'}(t) P^{L*}_{n'}(t) = \sum_{n'} V^{XX}_{nn'} P^{L*}_{n'}(t) P^L_0(t) P^L_1(t) \qquad \text{(C.11)}$$

where

$$V^{XX}_{nn'} = \langle B_{nn'}|X_1 X_0\rangle = \langle X'_n|\hat{Y}_n|X_1 X_0\rangle. \qquad \text{(C.12)}$$

To obtain the last relation we used the orthogonality $\langle Y_n|\hat{X}_{n'}|X_1X_0\rangle = 0$. From Eq. (7.16) we see that

$$V_{0n'}^{XX} = -V_{1n'}^{XX}. \tag{C.13}$$

We now obtain an explicit expression for $V_{nn}^{XX}$ by substituting Eq. (A.21) for $\hat{Y}_n$ into Eq. (C.12):

$$V_{nn}^{XX} = \langle X_nX_n|H\hat{X}_1^\dagger|X_0\rangle - \langle X_n|HX_n|X_1X_0\rangle - \Omega_n\langle X_nX_n|X_1X_0\rangle + V_{nn'}\langle X_nX_{n'}|X_1X_0\rangle. \tag{C.14}$$

where $n' \neq n$ and thus $n' = 1, n = 0$ or $n' = 0, n = 1$. Noting that $\langle X_nX_n|X_1X_0\rangle = 0$, $\langle X_nX_{n'}| = \langle X_1X_0|$ since the $X$ operators commute with each other, using Eq. (A.18) to obtain the states $\langle X_n|H$ and $H|X_0\rangle$, and Eq. (A.21) to express the commutator $[H, \hat{X}_1^\dagger]$ and using the orthogonality between the state $|Y\rangle$ and the $X$ states we obtain after some algebra that

$$\begin{aligned} V_{nn}^{XX} = &-V_{01}\langle X_nX_n|X_0X_0\rangle + \langle X_nX_n|\hat{Y}_1^\dagger|X_0\rangle - V_{10}\langle X_nX_n||X_1X_1\rangle \\ &+V_{nn'}\langle X_0X_1|X_1X_0\rangle + V_{nn'}\langle X_0X_1|X_1X_0\rangle \end{aligned} \tag{C.15}$$

where $n' \neq n$. As discussed above, $\langle X_mX_m|B_{ii'}\rangle = 0$, and therefore $\langle X_nX_n|\hat{Y}_1^\dagger|X_0\rangle = \langle X_nX_n|B_{10}\rangle = 0$. Using the relations $\langle X_0X_1|X_1X_0\rangle = 1$, $\langle X_nX_n|X_{n'}X_{n'}\rangle = 0$ for $n \neq n'$, and

$$\langle X_nX_n|X_nX_n\rangle = \langle X_n|[\hat{X}_n, \hat{X}_n^\dagger]|X_n\rangle + \langle X_n|\hat{X}_n^\dagger\hat{X}_n|X_n\rangle = 2 - \frac{2}{N_n}, \tag{C.16}$$

we finally obtain that

$$V_{nn}^{XX} = \frac{2V_{nn'}}{N_n}\ ,\ n' \neq n. \tag{C.17}$$

The above relations relate the $X$–$X$ interaction parameters to the Coulomb–induced LL coupling strength $V_{01}$.

## C.3 Additional approximations for the APM

The simplifications outlined in the previous sections will lead to a closed set of only a few equations, which still describe the dominant physical processes responsible for our experimental results, as explained in Ch. 7.4. Here we will outline how the equations in Appendix A become the model equations of Ch. 7.4.

We will start with the linear polarization equations, Eqs. (A.22) and (A.56). By replacing $\mathcal{Z}^L(t)$ with $-i\gamma\bar{P}^L(t)$, and using the symmetry relation to replace $\bar{P}^L_n(t)$ with $\pm\bar{P}^L(t)$ and $W_{nn'}$ with $\pm W$, we find the model equations Eqs. (7.17) - (7.19).

For the second order equations, by neglecting $X$–$X$ interactions we have only one equation of motion, for $\mathcal{M}(t)$. There are three source terms in Eq. (A.60), after applying the simplification of Eq. (C.6). Two of these terms are proportional to the incoherent linear correlation function $\bar{P}^L(t)$, which is characterized by the dephasing parameter $\gamma$, which is large, and therefore these source terms provide a weak incoherent background contribution to the FWM signal. We will neglect these terms, leading to Eq. (7.23).

Similarly, the source terms in Eq. (A.50) which are proportional to the incoherent densities, $\bar{n}_n(t)$ and $\mathcal{N}_{nm}(t)$ can be neglected, since they will make only minor quantitative changes to the calculated FWM signal without adding any new understanding, and they obscure the new physics from the other contributions. By applying Eq. (C.6) to Eq. (A.50), simplifying using the symmetry relations, and neglecting the incoherent density

contributions, we arrive at Eqs. (7.24) and (7.25).

Finally, to simplify Eq. (A.61), we will again use the logic that all the incoherent source terms add only a weak incoherent background. In this case, we will consider only the source terms which correspond to an excitation–induced correction to the $X \leftrightarrow Y$ scattering amplitude $W$. The other source terms are were either proportioanl to $\bar{P}^L(t)$ and thus broadened by an additional factor of $\gamma$, or terms with a similar time dependence to those included but reflecting the electron–hole asymmetry of the system. We are then only left with the source terms found in Eq. (7.26).